

Measuring Directional Stiffnesses in Pavement Base Material

by

Ronald Granville Terrell, B. S. Civil Engineering, P. E.

Graduate School Report

Presented to the Faculty of the Graduate School of

The University of Texas at Austin

in Partial Fulfillment

of the Requirements

for the Degree of

Master of Science in Engineering

The University of Texas at Austin

August 2002

DISTRIBUTION STATEMENT A
Approved for Public Release
Distribution Unlimited

20030220 027

AD NUMBER		DATE 05 Feb 03	DTIC ACCESSION NOTICE
1. REPORT IDENTIFYING INFORMATION		REQUESTER.	
A. ORIGINATING AGENCY NAVAL POSTGRADUATE SCHOOL, MONTEREY, CA 93943		1. Put yr on rev	
B. REPORT TITLE AND/OR NUMBER Measuring Directional Stiffnesses in Pavement		2. Compl	
C. MONITOR REPORT NUMBER Base Material By: Ronald G. Terrell, Univ. of Texas @ Austin		3. Attach mailex	
D. PREPARED UNDER CONTRACT NUMBER N62271-97-G-0073		4. Use un inform	
2. DISTRIBUTION STATEMENT		5. Do not for 6 ti	
APPROVED FOR PUBLIC RELEASE; DISTRIBUTION UNLIMITED		DTIC:	
		1. Assign.	
		2. Return.	

20030220 027

DTIC Form 50
DEC 91

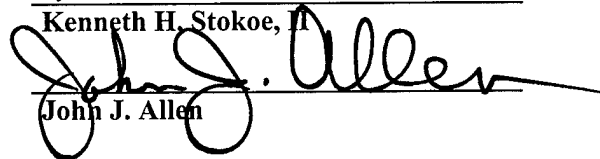
PREVIOUS EDITIONS ARE OBSOLETE

Measuring Directional Stiffnesses in Pavement Base Material

Approved by
Supervising Committee:



Kenneth H. Stokoe, II



John J. Allen

"To unpath'd waters, undreamed shores...."

- Shakespeare

Acknowledgements

Sincere appreciation is extended to Dr. Kenneth H. Stokoe, II for all of his guidance and inspiration. His unwavering dedication and support proved invaluable in the completion of this project. Equally important were the guidance of Dr. John J. Allen, who made this a truly successful joint operation, and the support of the International Center for Aggregates Research.

I would like to thank my teammates on this project: Brady Cox and Lin Yin-Cheng. Their knowledge, expertise, and good humor in the field were great assets during the more challenging moments. Thanks must also be extended to Dwane Lewis and Charles Smith of the Georgia Department of Transportation, and Carol Cook of Lafarge North America, who provided excellent logistical support.

My extension of gratitude would be incomplete without mentioning the other faculty members who enhanced my educational experience in so many ways: Dr. Alan Rauch, Dr. Stephen Wright, Dr. Ellen Rathje, Dr. Robert Gilbert, and Dr. Roy Olson. I am grateful to have been associated with such sublime group of professionals. I must also acknowledge the ladies who keep the gears turning from day-to-day and made my life much easier: Teresa Tice-Boggs, Alicia Zapata, and Chris Treviño.

Then there are my fellow classmates, Dennis, Jim, Adam, Sarah, Emily, Fadi, Jason, and numerous others who gave me so much support in and out of the classroom. To all of them I extend a hearty, "Cheers!"

I would like to thank my parents for their unwavering support through this endeavor and everything else they have endured during my vagabond years. I could not have done it without them.

I must also extend my appreciation to the United States Navy for not only giving me the opportunity to pursue this advanced degree, but for carrying me to many distant and exotic lands. I have seen and experienced more than I had ever thought possible.

Finally, I say thanks to Karl Terzaghi – engineer, soldier, scholar, pioneer, artist, lover of life. He taught me there is more to being an engineer than simply crunching numbers. Most importantly, though, he taught me that it all comes down to one thing – effective stress.

August 9, 2002

Abstract

Measuring Directional Stiffnesses in Pavement Base Material

Ronald Granville Terrell, M.S.E.

The University of Texas at Austin, 2002

Supervisor: Kenneth H. Stokoe, II

Unbound aggregate base layers in a quarry haul road in Georgia were characterized using embedded sensors and in-situ seismic testing. Two sections of the road were constructed as inverted pavements, one using a South African Roads Board method and the other using a conventional Georgia Department of Transportation method. A third was constructed using a traditional method. Horizontally propagating compression and shear waves were measured under varying loading conditions to determine the stiffnesses. It was found that the Georgia section was as good as the South African Section. Surprisingly, the traditional section was found to be somewhat stiffer than the other sections. This higher stiffness is thought to be due to a prolonged period of compaction prior to construction of the unbound aggregate base layer. Additionally, the negative

pore-water pressures in the partially saturated granular base had a significant impact on the stiffness of the UAB layer, especially under small load levels.

Table of Contents

List of Tables.....	xiii
List of Figures	xiv
CHAPTER ONE Introduction.....	1
1.1 Characterization of the Unbound Granular Base Layer in Flexible Pavements	1
1.1.1 Conventional Flexible Pavement	1
1.1.2 The Unbound Aggregate Base	2
1.1.3 The Inverted Pavement System.....	4
1.2 Seismic Testing on Georgia Test Road	4
1.3 Organization of This Report.....	7
CHAPTER TWO Construction of the Test Road	9
2.1 Introduction	9
2.2 The South African Base	9
2.3 The Georgia Base	15
2.4 The Traditional Base	17
CHAPTER THREE Cross-Anisotropic Model for Granular Material.....	18
3.1 Overview	18
3.2 Use of Seismic Waves to Characterize the Stiffness of the GAB Layer	20
3.2.1 Shear Waves	20
3.2.2 Compression Waves	23
3.3 Inherent Anisotropy.....	24
3.4 Effect of State of Stress	25
3.5 Stress-Induced Anisotropy	28
3.6 Relationship to In-Situ Seismic Testing.....	32

CHAPTER FOUR Material and Test Site.....	36
4.1 Overview	36
4.2 Graded Aggregate Base.....	38
4.2.1 Index Properties.....	38
4.2.2 In-Situ Density and Gravimetric Water Content.....	41
CHAPTER FIVE In-Situ Seismic Testing and Field Equipment	44
5.1 Overview	44
5.1.1 Traditional Crosshole Seismic Method.....	44
5.1.2 Traditional Downhole Method.....	47
5.1.3 Miniaturized Crosshole and Downhole Methods.....	48
5.2 Test Equipment	48
5.3 Test Site.....	51
5.3.1 Embedded Instrumentation	51
5.3.2 Placement of Embedded Instrumentation	53
5.4 Seismic Testing and Typical Records	58
5.4.1 PH-Wave Velocities.....	60
5.4.2 SHH-Wave Velocities.....	65
5.4.3 SHV-Wave Velocities.....	68
5.4.4 PV-Wave Velocities.....	71
CHAPTER SIX Unsaturated Soil Mechanics and the Soil-Water Characteristic Curve	74
6.1 Overview of Unsaturated Soil Mechanics.....	74
6.1.1 Stress State Variables	75
6.1.2 Total Suction	77
6.1.3 The Soil-Water Characteristic Curve	79
6.1.4 The Axis Translation Technique	80
6.2 Development of the Soil-Water Characteristic Curve.....	84
6.3 Negative Pore-Water Pressures in the UAB Layer	87

CHAPTER SEVEN Determination of Vertical and Radial Normal Stresses in the UAB Layer	89
7.1 Overview of ILLI-PAVE	89
7.2 Calculating the Vertical and Radial Total Normal Stresses.....	92
7.3 Calculating the Vertical and Radial Effective Normal Stresses.....	94
7.4 Total Stress Profiles in the UAB Layer from ILLI-PAVE.....	94
7.5 Radial Total and Effective Normal Stresses Using a Constant Value of K.....	99
CHAPTER EIGHT Results of the Seismic Crosshole Testing	102
8.1 Introduction	102
8.2 Resultant PH- and SHH-Wave Velocities for Each Site.....	102
8.3 Comparison of the PH-Wave Velocity Profiles	106
8.4 Comparison of the SHH-Wave Velocity Profiles	111
8.5 Resonant Column Results	112
8.6 Variation in PH- and SHH-Wave Velocities Versus ILLI-PAVE Radial Effective Stresses.....	114
8.7 Estimation of the Anisotropic State of the UAB Layer in Terms of E_{max}	115
CHAPTER NINE Summary and Conclusions.....	118
9.1 Summary	118
9.2 Conclusions	119
9.2.1 Field Instrumentation	119
9.2.2 Field Testing.....	122
9.2.3 Wave Velocity Measurements	123

Appendix A Measured PH- and SHH-Wave Velocities and Associated Loading Conditions	124
Appendix B Input Values for Young's Modulus and Associated Loading Conditions for ILLI-PAVE	126
Appendix C ILLI-PAVE Stresses and Loading Conditions.....	128
References	130
Vita	133

List of Tables

Table 4.1:	Gradation Requirements for GAB.....	38
Table 4.2:	Index Properties of GAB from the Lafarge Morgan County Quarry.....	39
Table 4.3:	Gradation of GAB from the Lafarge Morgan County Quarry	41
Table 4.4:	Density and Gravimetric Water Content Data from the Three Test Sections	42
Table 4.5:	Gravimetric Water Contents.....	42
Table 5.1:	Test Site Dimensions.....	52
Table 5.2:	Loading from a Fully-Loaded Dump Truck.....	60
Table 6.1:	Specimen Unit Weights and Applied Air Pressures.....	85
Table 6.2:	Volumetric Water Contents and Applied Air Pressures.....	86
Table 6.3:	Volumetric Water Contents and Corresponding Matric Suctions....	88
Table 7.1:	Input Values for Young's Modulus and Poisson's Ratio	92
Table 7.2:	Calculated Values for Young's Modulus for the UAB Layer at Site 5.....	93
Table 7.3:	Computed Total Normal Stresses in the Middle of the UAB Layer at Site 5	93
Table 7.4:	Computed Effective Normal Stresses in the Middle of the UAB Layer at Site 5	94
Table 8.1:	Range in $E_{H,max}$ from All Sites for Each Loading Condition	109
Table 9.1:	Summary of Results in Terms of E	121

List of Figures

Figure 1.1: Conventional flexible pavement system	1
Figure 1.2: Recoverable vs. non-recoverable deformation.....	3
Figure 1.3: Inverted flexible pavement system.....	4
Figure 1.4: Morgan County, Georgia.....	6
Figure 2.1: Traditional base layer under loaded conditions.....	10
Figure 2.2: South African inverted flexible pavement system	10
Figure 2.3: Saturation of a G1 base layer in South Africa.....	12
Figure 2.4: Consolidation of a G1 base layer in South Africa.....	13
Figure 2.5: Removing the expelled fines from a G1 base layer in South Africa.....	14
Figure 2.6: Construction of the GAB base in Georgia	16
Figure 2.7: Slushing of the GAB base in South African test section in Georgia	17
Figure 3.1: Cross-anisotropic model for a UAB layer in a flexible pavement ...	19
Figure 3.2: S wave within a uniform, infinite medium.....	21
Figure 3.3: S wave velocity versus degree of saturation	22
Figure 3.4: P wave within a uniform, infinite medium.....	23
Figure 3.5: Principal planes and associated polarized body waves in a cross- anisotropic model with the plane of isotropy oriented horizontally.....	28

Figure 3.6: Variations in P and S-wave velocities along the three principal stress directions under biaxial loading with only the vertical effective stress changing	30
Figure 3.7: Coincidence of particle motion and wave propagation for two shear waves	33
Figure 3.8: Axes of particle motion and wave propagation differ for SV and SH waves in crosshole testing.....	34
Figure 3.9: Schematic illustration of the variation in σ_h with σ_v for a constant coefficient of lateral earth pressure at rest	35
Figure 4.1: Locations of test sites in haul road.....	37
Figure 4.2: Maximum dry density	39
Figure 4.3: Gradation curve for the GAB from the Lafarge Morgan County Quarry.....	40
Figure 4.4: Locations of Sand Cone and NDG tests at the haul road	43
Figure 5.1: Field arrangement for a crosshole test.....	45
Figure 5.2: Example S-wave records measured in traditional crosshole testing using upward and downward impacts to help identify the initial SV-wave arrival	46
Figure 5.3: Field arrangement for a downhole test.....	47
Figure 5.4: Illustration of geophone arrangement used for measurement of body waves propagating in a horizontal direction	49
Figure 5.5: 3-D sensor used in crosshole testing	50
Figure 5.6: 1-D sensor used in downhole testing.....	51

Figure 5.7: Source hole and sensors for a typical site	52
Figure 5.8: Coring down 4 in. into the compacted UAB	54
Figure 5.9: 3-D sensor geophones in-line and orthogonal to wave ray path in UAB layer	55
Figure 5.10: 1-D sensors placed vertically in UAB layer.....	56
Figure 5.11: Installation of source casing and embedded sensors.....	56
Figure 5.12: Cable trenches with superimposed sources and P wave and S wave ray paths.....	57
Figure 5.13: Site 2 sources and embedded sensor locations marked on HMA surface	58
Figure 5.14: Testing with a van load	59
Figure 5.15: Testing with a dump truck load.....	60
Figure 5.16: Source hammer and accelerometer	61
Figure 5.17: Using a small hammer to create a PH wave.....	62
Figure 5.18: Typical trigger record for PH wave.....	63
Figure 5.19: Typical record for PH-wave arrival.....	64
Figure 5.20: Determining a calibration factor for PH and SHH waves.....	65
Figure 5.21: Typical record for SHH(R)-wave arrival	67
Figure 5.22: Typical record for SHH(L)-wave arrival.....	67
Figure 5.23: Typical "butterfly" curves for SHH-wave arrival	68
Figure 5.24: Using a wedged source to create an SHV wave.....	69
Figure 5.25: Typical record for SHV(U)-wave arrival	70
Figure 5.26: Incident and reflected waves in horizontal layering.....	71

Figure 5.27: Using a small ball-peen hammer to create a PV wave	72
Figure 5.28: Typical record for PV-wave arrival.....	73
Figure 6.1: Classification of the regions within a saturated-unsaturated soil profile	75
Figure 6.2: Separation of saturated and unsaturated soil mechanics based on the stress state description.....	76
Figure 6.3: Elements showing the stress state at a point in a saturated soil and unsaturated soil.....	77
Figure 6.4: Residual saturation	79
Figure 6.5: Typical soil-water characteristic curves for four soils from Saskatchewan, Canada	80
Figure 6.6: Disassembled Tempe pressure cell	81
Figure 6.7: Assembled Tempe pressure cell.....	81
Figure 6.8: Cross section of a Tempe pressure cell	82
Figure 6.9: Tempe pressure cell with water outlet connected to water reservoir at same height as top of soil specimen	83
Figure 6.10: Compacted GAB in a Tempe pressure cell	84
Figure 6.11: Soil-water characteristic curve for UAB layer	86
Figure 6.12: Determining the matric suctions	87
Figure 7.1: ILLI-PAVE pavement model	90
Figure 7.2: Example system configuration of the finite element mesh	91
Figure 7.3: Vertical total normal stresses in the UAB layer at Site 5 based on ILLI-PAVE and 2:1 distributions.....	95

Figure 7.4: Vertical total normal stresses in the UAB layer at Site 5 based on ILLI-PAVE and Boussinesq distributions.....	96
Figure 7.5: Radial total normal stresses in the UAB layer at Site 5 from ILLI-PAVE.....	96
Figure 7.6: Vertical effective normal stresses in the UAB layer at Site 5 based on ILLI-PAVE and 2:1 distributions.....	97
Figure 7.7: Vertical effective normal stresses in the UAB layer at Site 5 based on ILLI-PAVE and Boussinesq distributions	98
Figure 7.8: Radial effective normal stresses in the UAB layer at Site 5 from ILLI-PAVE.....	98
Figure 7.9: Calculated radial total normal stresses in UAB layer at Site 5	100
Figure 7.10: Calculated radial effective stresses in UAB layer at Site 5	100
Figure 8.1: Variations of PH- and SHH-wave velocities with stress state for Site 2.....	103
Figure 8.2: Variations of PH- and SHH-wave velocities with stress state for Site 3.....	104
Figure 8.3: Variations of PH- and SHH-wave velocities with stress state for Site 4.....	104
Figure 8.4: Variations of PH- and SHH-wave velocities with stress state for Site 5.....	105
Figure 8.5: Variation of PH-wave velocity with stress state for all four sites..	107
Figure 8.6: Variation of $E_{H,max}$ with stress state for all four sites	108
Figure 8.7: Variation of $E_{H,max}$ with stress state for Site 5.....	110

Figure 8.8: Variation of SHH-wave velocity with state of stress for all four sites.....	111
Figure 8.9: Variation of SHV-wave velocity with effective confining pressure of the UAB determined in laboratory by resonant column testing	112
Figure 8.10: Comparison of field SHH-wave velocities measured in the UAB layer with SHV-wave velocities measured in the laboratory by resonant column testing with a reconstituted UAB specimen.....	113
Figure 8.11: PH-wave velocity vs. ILLI-PAVE radial effective normal stress for all four sites	114
Figure 8.12: SHH-wave velocity vs. ILLI-PAVE radial effective normal stress for all four sites	115
Figure 8.13: $E_{V,max}$ and $E_{H,max}$ vs. the effective normal stresses in direction of loading for Site 5	116
Figure 8.14: $E_{V,max}$ and $E_{H,max}$ vs. the loading conditions for Site 5	117
Figure 9.1: $E_{H,max}$ vs. average radial effective normal stress	122

CHAPTER ONE

Introduction

1.1 Characterization of the Unbound Granular Base Layer in Flexible Pavements

1.1.1 Conventional Flexible Pavement

According to the American Association of State Highway Transportation Officials (AASHTO) 1993, a conventional flexible pavement is composed of three components: (1) a prepared subgrade, (2) layers of subbase and base materials, and (3) a surface layer, as shown in Figure 1.1.

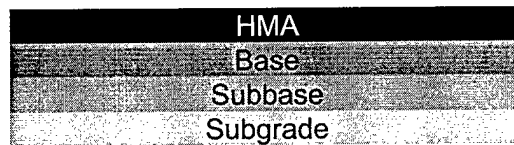


Fig. 1.1 Conventional flexible pavement system

The surface layer is normally a hot mix asphalt (HMA), and the base and subbase layers are unbound granular materials. These unbound granular layers serve as the major structural components of the pavement system. As such, it is particularly important to be able to characterize unbound aggregate base (UAB) materials as these materials strongly influence the performance of the overlying

HMA surface. The focus of the work presented in this study deals with in-situ characterization of UAB materials.

1.1.2 The Unbound Aggregate Base

The UAB is a multi-phase material composed of aggregate particles, air voids, and water. Such factors as density, stiffness, pore water pressure, stress history, and temperature affect the mechanical behavior of the unbound granular materials in the UAB. Due to the non-elastic nature of granular material above some threshold strain, the UAB experiences some non-recoverable deformation after each load application that creates strains above some threshold strain. With transient loads, however, the amount of non-recoverable deformation is generally much smaller than the amount of recoverable deformation, as illustrated in Figure 1.2 (note: the figure is not the stress-strain curve for a soil but simply an illustration of a generalized response). As a result, elastic theory can be used to analyze the UAB's response to loading (Brown, 1996).

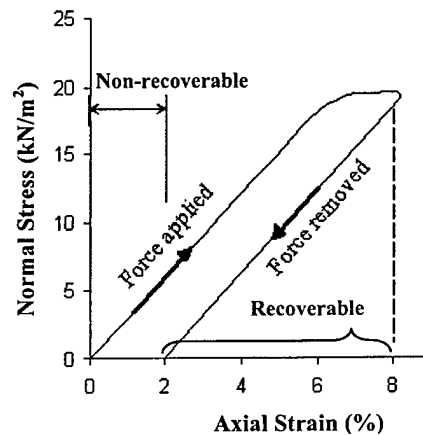


Fig. 1.2 Recoverable vs. non-recoverable deformation (from www.gamedev.net/reference/programming/features/deformsolid2, 2002)

The Georgia Department of Transportation (GDOT) currently uses the AASHTO pavement design procedure for designing flexible pavements. This procedure takes a conservative view of the structural contribution of the UAB, which is constructed from a material known as Graded Aggregate Base (GAB). The feasibility of relying more on the UAB for structural support has been raised, especially when used in conjunction with a cemented subbase. Such a pavement system is shown in Figure 1.3 and is called an “inverted” pavement system. This inverted pavement system has been used successfully by the South Africans since the 1950’s (South African National Roads Agency, 1998).

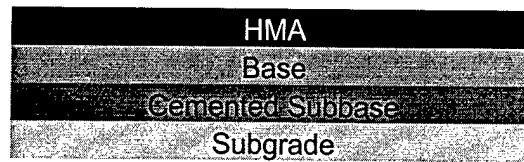


Fig. 1.3 Inverted flexible pavement system

1.1.3 The Inverted Pavement System

In an inverted pavement system, the stiffness of one of the lower supporting layers is greater than the stiffness of the upper structural layers. A stabilized, or cemented, subbase layer acts as a platform for a UAB. The stiffness of the supporting layers beneath this cemented subbase is decreased gradually and systematically with depth, creating a relatively deep supportive pavement structure. In addition to acting as a “backbone” of the pavement, the cemented subbase acts as a firm base on which to build the UAB layer and keeps this base layer in a state of compression when loaded (South African National Roads Agency, 1998). The SARB maintains that the inverted pavement system provides such an excellent structural performance that it requires only a thin HMA riding course.

1.2 Seismic Testing on Georgia Test Road

In this study, UAB layers in a haul road in Georgia were characterized in situ. The GDOT constructed two test sections of inverted pavement in the haul

road which acts as the entrance road to a new crushed aggregate quarry in Morgan County, Georgia. In-situ seismic testing was performed to compare the stiffnesses of the UAB layer in these sections with a similar layer in a traditional pavement section, also constructed in the haul road. One inverted section was constructed using the South African Roads Board (SARB) method; the other inverted section was constructed using the conventional GDOT method. A third control section in the haul road was constructed in the traditional method so that it could be compared with the other two sections. Seismic crosshole and downhole testing of the UAB was done in order to allow a direct comparison of the stiffness characteristics of the three different sections by determining the directional stiffnesses of each section. Geophones were installed in the UAB layers to measure the travel times of compression and shear waves under different loading conditions.

The haul road was constructed at a quarry owned by Lafarge North America in Morgan County, Georgia, 60 miles east of Atlanta (see Figure 1.4).



Fig. 1.4 Morgan County, Georgia
(from www.ph.dhr.state.ga.us/regional/morgan/index.shtml, 2002)

The haul road contains the following sections:

1. Section #1: 1000-ft (300-m) length of traditional haul road (prepared subgrade with minimum CBR of 15, 2 in. (5.1 cm) of GAB, 6 in. (15.2 cm) of surge stone, 8 in. (20.3 cm) GAB, and topped with 3 in. [7.6 cm] of HMA);
2. Section #2: 400-ft (120-m) length of inverted pavement with a South African base; and
3. Section #3: 400-ft length of inverted pavement with a Georgia base.

Pavement sections #2 and #3 include a prepared subgrade, 2 in. (5.1 cm) of unbound GAB, 8 in. (20.3 cm) of GAB with 4% to 5% cement by volume (the "backbone" layer), 6 in. (15.2 cm) of unbound GAB (UAB), and 3 in. (7.6 cm) of

Marshall design HMA. The only difference between the South African Section #2 and Georgia Section #3 is that a process known as "slushing" was used as part of the South African compaction process. Slushing involves compacting the UAB under saturated conditions and sweeping off the fines that squeeze to the surface, resulting in a "super" dense matrix that is 88% of the solid particle density. The GDOT believes that with the cemented layer acting as a compaction platform, the same density can be achieved in the Georgia base using typical compaction methods without slushing.

With assistance from the International Center for Aggregates Research (ICAR), in-situ seismic crosshole and downhole testing was conducted in order to evaluate the stiffness of each UAB to test indirectly the theory that one is denser than the other.

1.3 Organization of This Report

This study begins with a description of the construction methods and specifications of the South African and Georgia bases in Chapter 2. An explanation of the theoretical framework, specifically, how the cross-anisotropic model applies, is presented in Chapter 3. The material, test site, and in-situ seismic testing and field equipment are described in detail in Chapters 4 and 5, respectively. Unsaturated soil mechanics and the development of a soil-water

characteristic curve in order to determine the negative pore water pressures present in the unsaturated UAB are discussed in Chapter 6. A description of the utilization of ILLI-PAVE to determine the vertical and axial stresses can be found in Chapter 7. The results of the seismic crosshole testing are presented in Chapter 8. The relative stiffnesses under varied loading conditions are compared and discussed in this chapter, along with the comparative stiffnesses of the Georgia and South African bases. The summary, conclusions, and recommendations are presented in Chapter 9.

CHAPTER TWO

Construction of the Test Road

2.1 Introduction

As mentioned in Chapter One, three test sections were constructed along the quarry haul road in order to study the characteristics of each UAB layer. The characteristics that were determined were (1) density, (2) water content, and (3) stiffness. Two inverted pavement systems were constructed resulting in two different base layers: the South African base section and the Georgia base section. Additionally, a conventional base layer was constructed with which to compare the inverted base layers.

2.2 The South African Base

The SARB pavement design philosophy revolves around the use of a high performance crushed stone base, commonly known as G1, to produce a pavement with outstanding load bearing capacity (South African National Roads Agency, 1998). The G1 base is highly interlocked, non-cohesive, crushed stone particles that is compacted in such a way as to create a "super densified" material with a density on the order of 88% of the "solid" particle density. Unfortunately, this high degree of densification makes the G1 base sensitive to undue flexural

movement, poor support, and tension stress (as illustrated in Figure 2.1) which could result in sufficient dilation of the layer that undoes the state of “super” density.

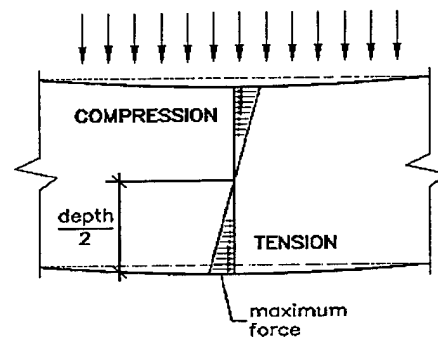


Fig. 2.1 Traditional base layer under loaded conditions (from www.mevicker.com/vwall/Hand03b.GIF, 2002)

This potential problem with the G1 base led to the development of the inverted pavement design philosophy (South African National Roads Agency, 1998). The main idea behind the inverted pavement philosophy is that the stiffer cemented layer directly beneath the G1 base layer (see Figure 2.2) keeps the base layer in compression during “bending” (loading).

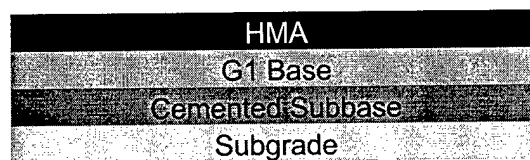


Fig. 2.2 South African inverted flexible pavement system

Attainment of the super density within the G1 matrix is a two-phase process: (1) the "normal" compaction phase followed by (2) the aggregate interlocking or slushing phase. The normal compaction phase comprises compacting the material in accordance with standard South African practice for gravel road building material (at optimum moisture content for the material and equipment) up to the minimum density level required for successful initiation of the slushing phase, normally between 144 and 146 pcf (2300 and 2330 Kg/m³). The slushing phase involves recompacting the same material under nominally saturated conditions in order to extract the fines from the G1 matrix. Through this slushing process, the larger particles are interlocked to form the super dense matrix. The attainment of this very dense matrix requires a very sound and moisture resistant support – the cemented subbase.

The cemented subbase is typically between 6 and 12 in. (15 and 30 cm) thick and stabilized to an unconfined compressive strength of at least 145 to 435 psi (1.0 to 3.0 MPa) after 7 days. The stabilizer is lime or Portland cement at an amount that typically does not exceed 4% by volume. SARB requires the material to be "compacted to a percentage of modified AASHTO density, 90% or 93% (as required)."

After the cemented subbase is placed and cured, the 5- to 6-in. (12.5- to 15-cm) thick G1 base layer is constructed in one layer and compacted following

normal procedures. After the G1 material is deemed stable, the slushing phase is initiated. The slushing process is executed by saturating the G1 layer and consolidating it with heavy vibratory rollers, steel-wheeled rollers, and pneumatic-tired rollers to expel the excess fines, as shown in Figures 2.3 and 2.4. Saturation of the G1 material serves a two-fold purpose: (1) providing a medium through which to remove the excess fines from the G1, and (2) transforming the fines into a lubricant which aid in the re-orientation and interlocking of the larger aggregate particles.

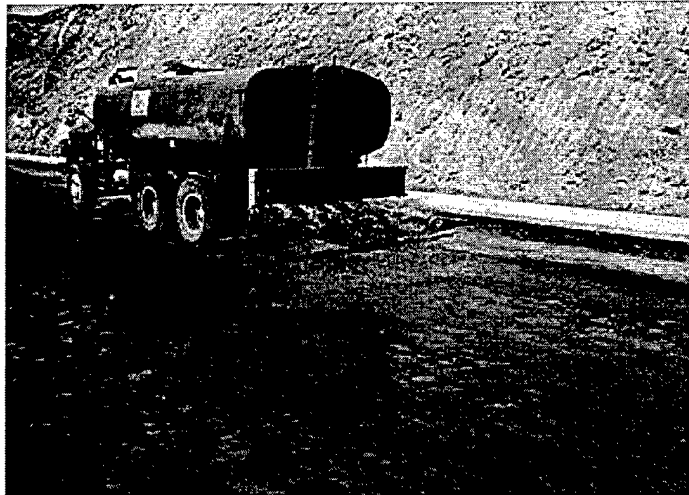


Fig. 2.3 Saturation of a G1 base layer in South Africa (photo courtesy of Kobus van der Walt, South African National Roads Agency)

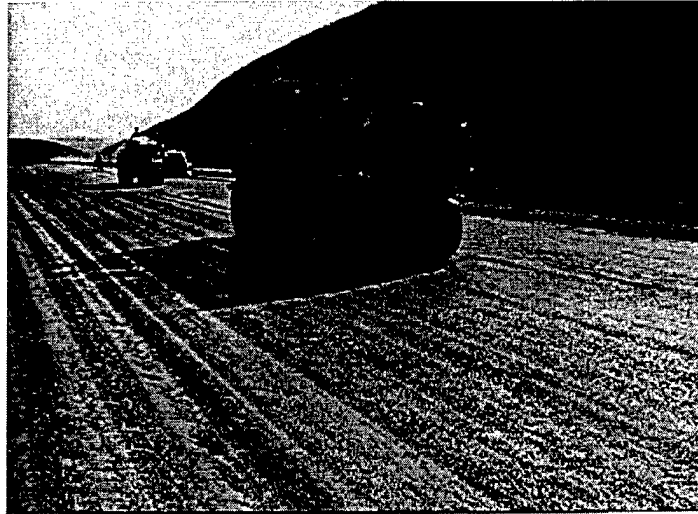


Fig 2.4 Consolidation of a G1 base layer in South Africa (photo courtesy of Kobus van der Walt, South African National Roads Agency)

At the beginning of the slushing process, the expelled fines will be very fine, silty material, growing coarser as the process continues. These fines are removed from the surface with hand brooms or light mechanical rotary brooms, as shown in Figure 2.5.

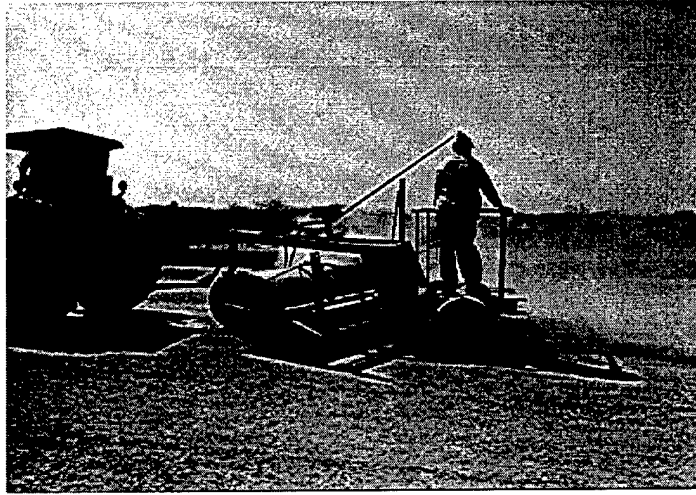


Fig. 2.5 Removing the expelled fines from a G1 base layer in South Africa (photo courtesy of Kobus van der Walt, South African National Roads Agency)

Air bubbles also form on the surface directly behind the roller wheels, serving as an indicator that there are voids in the layer. The layer is considered sufficiently slushed when these bubbles no longer appear. Additionally, the expelled water loses its coloration, indicating the removal of all excess fines (South African National Roads Agency, 1998). At the end of this phase, the G1 material is in its super densified state, with a density of around 147 pcf (2360 Kg/m^3).

2.3 The Georgia Base

The GDOT's goal was to produce a GAB base layer whose strength and density equaled that of the South African G1 base, without the slushing process. Sections 300 and 310 of the GDOT 1993 Specifications covered the construction of the GAB and subbase layers. Although there are no sections that specifically govern the construction of a cemented-stabilized GAB subbase, the GDOT Specifications cover this general manner of construction, requiring the central plant mix method. This construction process was waived, however, due to the small size of this section of roadway.

The cement-stabilized subbase comprises one, 8-in. (20.3-cm) thick lift of GAB mixed in place with 5% by volume Portland cement. Since the Specifications do not cover this type of subbase, a verbal agreement was made with the contractor to construct this base using the South African method as much as practicable. Cores were taken of the subbase and found to have an average unconfined compressive strength of 450 psi (3.1 MPa), greater than required by the South African method (435 psi [3.0 MPa]).

The Specifications require that the GAB base be no more than 8 in. thick after compaction, placed in one course, and compacted to 100% (for Group II) of the maximum dry density (136.7 pcf for this material). The GDOT construction procedures were followed with the exception that compaction requirements were

88% of the apparent density as determined by SARB. The actual densities obtained in the two inverted test sections are discussed in Chapter 4.

Construction of the GAB base layer is shown in Figure 2.6. Figure 2.7 shows the slushing process on the South African test section in Georgia.



Fig. 2.6 Construction of the GAB base in Georgia (photo courtesy of Dwane Lewis, Georgia Department of Transportation)



Fig. 2.7 Slushing of the GAB base in South African test section in Georgia (photo courtesy of Dwane Lewis, Georgia Department of Transportation)

2.4 The Traditional Base

A typical haul road with a conventional base is constructed by placing 6 in. (15.2 cm) of surge stone on top of 2 in. (5.1 cm) of GAB and a prepared subgrade. The surge stone is 4 to 8 in. (10.2 to 20.3 cm) in diameter and is compacted by normal construction traffic (haul trucks, water trucks, etc.). After the surge stone has been in place and compacted over several months, 8 in. (20.3 cm) of GAB is placed on top of the surge stone subbase and compacted according to the GDOT Specifications. Three inches (7.6 cm) of HMA is then placed on top of the compacted GAB base.

CHAPTER THREE

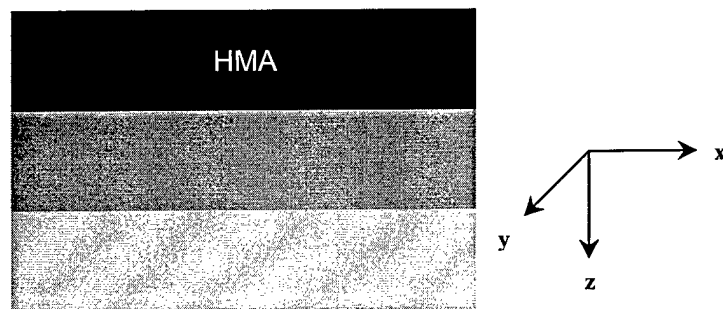
Cross-Anisotropic Model for Granular Material

3.1 Overview

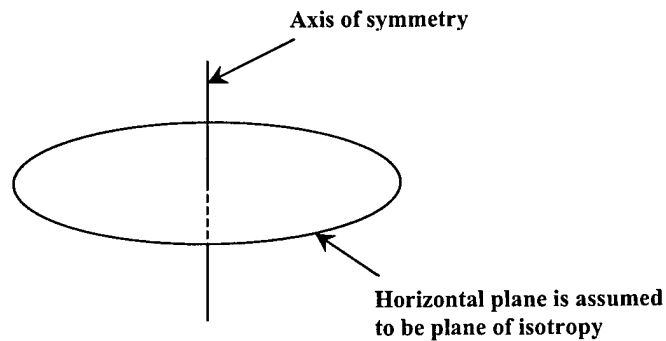
Much research has been conducted in understanding the anisotropic behavior, i.e., the directional dependency of material properties, of UAB's under varied loading conditions. According to Tutumluer (1998), the behavior of a granular medium depends on the arrangement of particles at that point. Aggregate characteristics and construction methods usually determine the particle arrangement. With the UAB in a flexible pavement, a structural anisotropy is created during construction by aggregate placement and compaction. This layer, therefore, becomes stiffer in the vertical direction than the horizontal direction even before a wheel load creates the situation of a stress-induced anisotropy (Tutumluer, 1998).

The difference in stiffness with direction is a key element in modeling the UAB material with a cross-anisotropic model. Unlike an isotropic model, the cross-anisotropic model has different material stiffnesses assigned in the horizontal and vertical directions. Within the cross-anisotropic model representing the UAB, the base is considered to exhibit two kinds of anisotropy: inherent (structural) and stress-induced. Also, the orientations associated with

each of these anisotropies are assumed to coincide and be oriented in the horizontal and vertical directions. Furthermore, for the UAB in a pavement, the axis of symmetry is assumed to be vertical and the horizontal plane is assumed to be the plane of isotropy (discussed further in Section 3.4). This model is illustrated in Figure 3.1.



a. Orientation of axes in the UAB



b. Axis of symmetry and isotropic plane

Fig. 3.1 Cross-anisotropic model for a UAB layer in a flexible pavement

3.2 Use of Seismic Waves to Characterize the Stiffness of the GAB Layer

Measurements of the propagation velocities of seismic body waves are a long-practiced method of characterizing the small-strain stiffness of all types of soils in the laboratory and in the field. Specifically, shear wave and compression wave velocities, V_s and V_p , respectively, are used to determine the shear modulus, G , and constrained modulus, M , respectively. These parameters are measured at strains less than or equal to 0.0001% where the moduli are independent of strain amplitude and exhibit the largest values; hence, they are typically denoted as G_{\max} and M_{\max} , respectively. Measurements of V_s and V_p along various directions permit one to characterize the anisotropic nature of the soil or GAB (Stokoe et al, 1994). Many factors affect the velocities of compression and shear waves, including the degree of saturation, the state of effective stress, inherent anisotropy, and stress-induced anisotropy (Stokoe and Santamarina, 2000). These seismic waves and associated factors are discussed below.

3.2.1 Shear Waves

Shear waves (also called S waves) are stress waves that exhibit particle motion perpendicular to the direction of wave propagation, as shown in Figure 3.2.

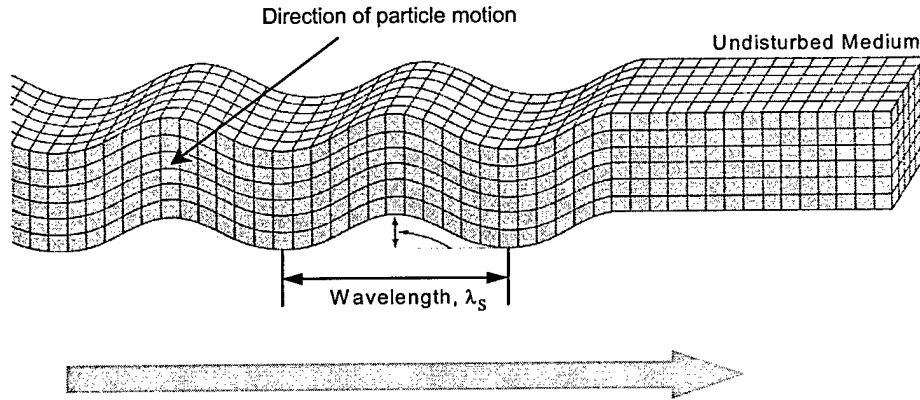


Fig. 3.2 S wave within a uniform, infinite medium (after Bolt, 1976)

In granular (and other) materials, V_s is controlled by G_{\max} and the mass density, ρ , as follows:

$$V_s = \sqrt{\frac{G_{\max}}{\rho}} \quad (3.1)$$

Also, V_s is related to the mean effective stress, σ_o' , under isotropic loading as:

$$V_s = V_{s1} \left(\frac{\sigma_o'}{P_a} \right)^m \quad (3.2)$$

where V_{s1} equals the shear wave velocity at σ_o' equal to one atmosphere,
 P_a equals atmospheric pressure, and
 m equals an exponent.

V_s can also be related to anisotropic conditions as discussed in Sections 3.4 and 3.5.

In an unsaturated soil, capillary forces can affect the value of V_s and G_{\max} of the soil, with the relevance of capillary forces on shear stiffness increasing with

the fines content. The pore water pressures in unsaturated material are negative, resulting in a higher level of effective stress. As a result, G_{\max} and V_s increase as the degree of saturation, S_r , decreases in most soils (Cho and Santamarina, 2001). This effect is illustrated in Figure 3.3, which shows how V_s of a granite powder specimen ($d_{50}=89\mu\text{m}$) increases during drying. This effect increases as d_{50} decreases.

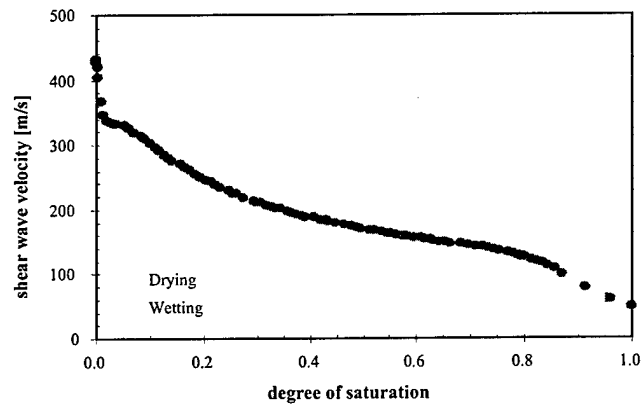


Figure 3.3 S wave velocity versus degree of saturation (granite powder, $d_{50}=89\mu\text{m}$, applied $\sigma_v=1.5\text{ kPa}$) (Cho and Santamarina, 2000)

As previously stated, a greater effective stress results in an increase in G_{\max} and V_s . The effects of isotropic pressure and anisotropic pressure are discussed in Section 3.5.

3.2.2 Compression Waves

Compression waves (also called P waves) are stress waves that have particle motion parallel to the direction of propagation, as illustrated in Figure 3.4. In-situ seismic measurements with P waves are performed at small strains just as with shear waves.

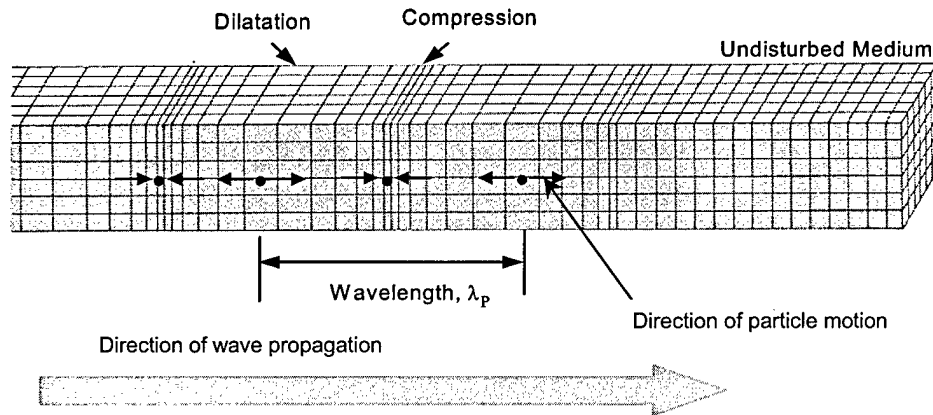


Figure 3.4 P wave within a uniform, infinite medium (after Bolt, 1976)

Also similar to V_s , V_p is controlled by the stiffness of the soil skeleton when S_r is less than 99%. Under these conditions, the P-wave velocity at small strains is related to M_{max} , ρ , Young's modulus, E_{max} , and Poisson's ratio, ν , as follows:

$$V_p = \sqrt{\frac{M_{max}}{\rho}} = \sqrt{\frac{E_{max}(1-\nu)}{\rho(1+\nu)(1-2\nu)}} \quad (3.3)$$

For a homogeneous, isotropic material, V_p is related to V_s through ν as:

$$V_p = V_s \sqrt{\frac{1-\nu}{0.5-\nu}} \quad (3.4)$$

As previously stated, a decrease in S_r results in an increase in effective stress. Accordingly, M_{\max} and V_p increase as S_r decreases. With a completely saturated material ($S_r = 100\%$), however, the relative incompressibility of the water dominates M_{\max} , resulting in a value of V_p of approximately 5000 fps (Stokoe and Santamarina, 2000).

3.3 Inherent Anisotropy

Inherent anisotropy (also called structural anisotropy) is associated with the depositional process and grain characteristics and is independent of the applied stress (Arthur and Menzies, 1972; and Oda, 1972). For an isotropic material skeleton, stiffness is independent of direction under isotropic loading conditions ($\sigma_1' = \sigma_2' = \sigma_3'$, where σ_1' , σ_2' , and σ_3' represent the major, intermediate, and minor principal effective stresses, respectively). If the stiffness is dependent on direction under isotropic loading conditions, however, then the material is anisotropic and is said to possess inherent or structural anisotropy.

Inherent (structural) anisotropy is manifested in the variation with direction of the material constants which represent the material skeleton. These

material constants are associated with the type of grains, the nature of the contacts, and the stability of the soil skeleton. The material constants in constrained compression and shear are denoted by C_p and C_s , respectively (see Eqs. 3.5 and 3.6 below). The looser and finer the soil, the lower the values for C_p and C_s (Stokoe and Santamarina, 2000).

3.4 Effect of State of Stress

As previously stated, body wave velocities increase with an increase in effective stress. P and S waves are considered polarized when their directions of particle motion and wave propagation are both oriented along principal stress directions. The propagation velocities of polarized body waves can be expressed by the following equations (Stokoe and Santamarina, 2000):

$$V_p = C_p \sqrt{F(e)} \left(\frac{\sigma'_a}{P_a} \right)^{ma} \quad (3.5)$$

$$V_s = C_s \sqrt{F(e)} \left(\frac{\sigma'_a}{P_a} \right)^{na} \left(\frac{\sigma'_b}{P_a} \right)^{nb} \quad (3.6)$$

where C_p = material constant in constrained compression,
 C_s = material constant in shear,
 $F(e)$ = void ratio homogenization function,
 P_a = atmospheric pressure in the same units as σ'_a and σ'_b ,
 σ'_a = effective principal stress in the direction of wave propagation (in same units as P_a),
 σ'_b = effective principal stress in the direction of particle motion (in same units as P_a),
 $ma \cong 0.25$ for relatively uniform granular materials, and
 $na = nb \cong 0.125$ for relatively uniform granular materials.

These equations show that for polarized body waves, V_p depends only on the state of stress in the direction of wave propagation, while V_s depends on both the states of stress in the directions of wave propagation and particle motion.

Inherent (structural) anisotropy in compacted granular soils under isotropic loading conditions has been shown to be well represented by a cross-anisotropic model through the use of calibration chamber tests. In this case, the axes for structural and stress-induced anisotropy can be assumed to coincide. One example of this condition is a granular sample constructed through dry pluviation.

A cross-anisotropic model represents this sample in which the stiffnesses are the same along the x and y axes (horizontal plane), serving as the plane of isotropy, but the stiffnesses in the vertical plane are slightly less. The following general relationships demonstrate this condition in terms of polarized P-wave and S-wave velocities (Lee and Stokoe, 1986; Belloti et al, 1996):

$$V_{Px} = V_{Py} > V_{Pz1} = V_{Pz2} \quad (3.7)$$

$$V_{Sxy} = V_{Syx} > V_{Sxz} = V_{Szx} = V_{Syz} = V_{Szy} \quad (3.8)$$

where V_{Px} , V_{Py} , and V_{Pz} = the P-wave velocities in the x, y, and z directions, respectively,

V_{Sxy} and V_{Syx} = the S-wave velocities in the x-y plane,

V_{Sxz} and V_{Szx} = the S-wave velocities in the x-z plane, and

V_{Syz} and V_{Szy} = the S-wave velocities in the y-z plane.

The principal planes and associated polarized body waves are shown in Figure 3.5.

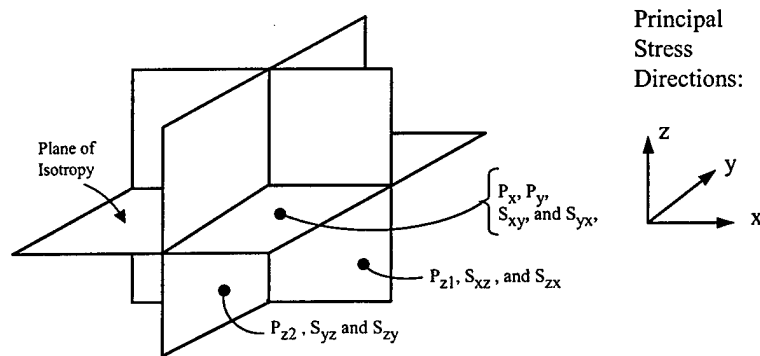


Fig. 3.5 Principal planes and associated polarized body waves in a cross-anisotropic model with the plane of isotropy oriented horizontally (Stokoe and Santamarina, 2000)

Under isotropic loading conditions, the P- and S-wave velocities in the xy plane are approximately 10% higher than the respective velocities in the xz and yz planes (Stokoe and Santamarina, 2000).

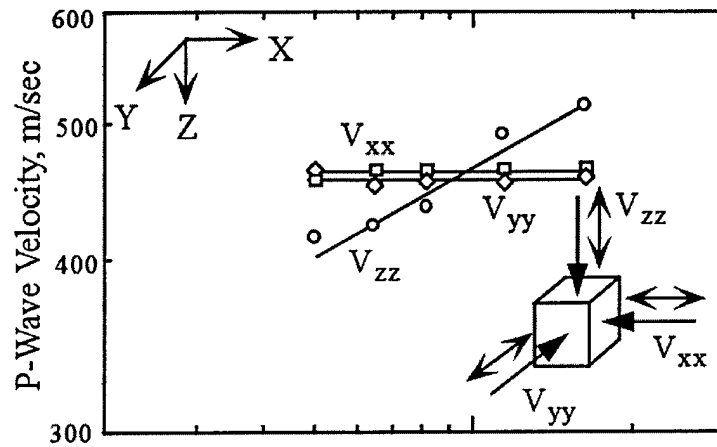
Although the horizontal plane would logically be the plane of isotropy in a compacted UAB, the stiffness (and corresponding body wave velocities) are predicted to be higher in the vertical plane than in the horizontal due to the compaction according to Tutumluer (1998). This relationship remains to be one of the points investigated in this study.

3.5 Stress-Induced Anisotropy

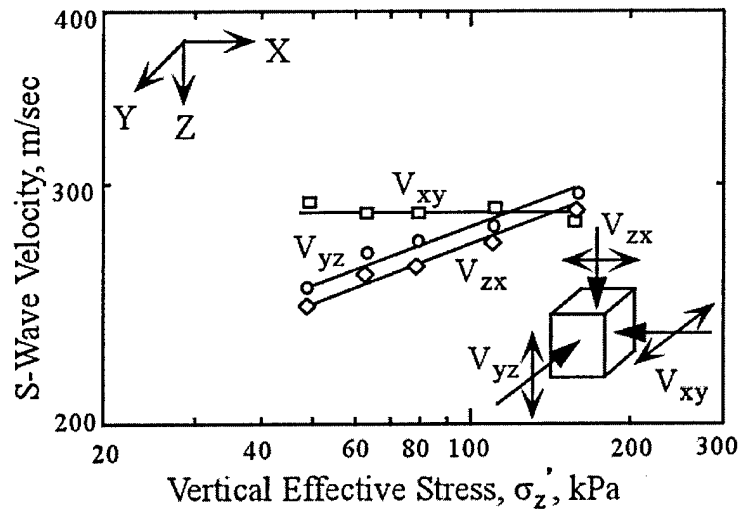
Stress-induced anisotropy is anisotropy created by the stress state applied to a material. The two stress conditions normally associated with stress-induced

anisotropy are biaxial ($\sigma_1' = \sigma_2' > \sigma_3'$, or $\sigma_1' > \sigma_2' = \sigma_3'$) and true triaxial ($\sigma_1' > \sigma_2' > \sigma_3'$) principal stresses. The biaxial stress condition is presented here as it is assumed to most closely represent the state of stress of a UAB layer directly under a wheel load.

Lee (1993) conducted numerous tests on sand under biaxial loading conditions using the large-scale triaxial chamber (LSTC). One set of results is shown in Fig. 3.6. For this test, the principal stresses in the x and y directions were held constant at 83 kPa, while the principal stress in the z direction was varied from 41 kPa to 145 kPa.



a. Variations in P-wave velocity with changes in vertical effective stress.



b. Variations in P-wave velocity with changes in vertical effective stress.

Figure 3.6 Variations in P and S-wave velocities along the three principal stress directions under biaxial loading with only the vertical effective stress changing (Stokoe et al, 1994)

As can be seen in Figure 3.6a, only the P-wave velocity in the vertical direction, V_{zz} , varied with stress, increasing with increases in the applied vertical stress. The wave velocities in the horizontal plane, V_{xx} and V_{yy} , remained unchanged, because the confining pressures in the direction of wave propagation and particle motion (x and y axes) were held constant. These results indicate that the P-wave velocity is related only to the effective principal stress in the direction of wave propagation, as indicated in Equation 3.5.

Although the polarized shear wave velocities are more complex, they also fall in line with the cross-anisotropic model. As can be seen in Figure 3.6b, the S-wave velocities in the yz and zx plane, V_{yz} V_{zx} , varied with stress, increasing with increases in the applied vertical stress. As with the P-wave, the S-wave velocities of the shear wave contained in the horizontal plane (V_{xy}) remained unchanged. The constant S-wave velocity is due to confining pressures in the directions of wave propagation and particle motion (x and y axes) were held constant. These results indicate that the S-wave velocity is related to both the effective principal stresses in the directions of wave propagation and particle motion, as indicated in Equation 3.6.

3.6 Relationship to In-Situ Seismic Testing

The cross-anisotropic model is a good approximation to what might be expected for a level soil site, especially as it relates to traditional downhole and crosshole seismic testing (assuming that the waves are propagating horizontally in the crosshole test and vertically in the downhole test). This concept is discussed by Stokoe and Santamarina (2000).

First, due to effects of inherent anisotropy coupled with stress-induced anisotropy, the P-wave velocity measured in the downhole test, V_{Pz} , will not equal the P-wave velocity measured in the crosshole test (V_{Px} or V_{Py} and $V_{Px} = V_{Py}$) in unsaturated soil. For a normally consolidated soil, V_{Pz} would generally be larger than V_{Px} or V_{Py} .

Second, shear wave velocities along the xz (or yz) plane will be equal: the SH-wave velocity (V_{Szx}) measured in the downhole test is equal to the SV-wave velocity (V_{Sxz}) measured in the crosshole test. The axes of particle motion and wave propagation coincide for these two shear waves, as illustrated in Figure 3.7.

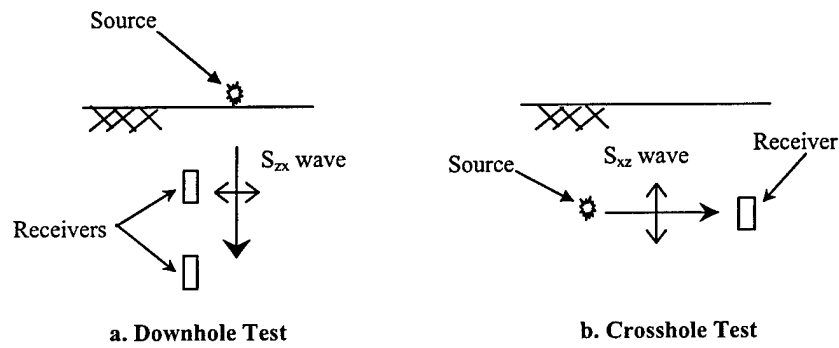


Fig. 3.7 Coincidence of particle motion and wave propagation for two shear waves

Conversely, the SH-wave velocity ($V_{S_{xy}}$) is different from the SV-wave velocity ($V_{S_{xz}}$) for waves measured in the crosshole test, as noted by Fuhrman (1993) and Roblee et al. (1994). This difference is due to the axes of particle motion and wave propagation being different for these two waves, as illustrated in Figure 3.8. The benefit of these differing velocities, however, is that they could be used to evaluate stress state (Lee and Stokoe, 1986 and Lee, 1993).

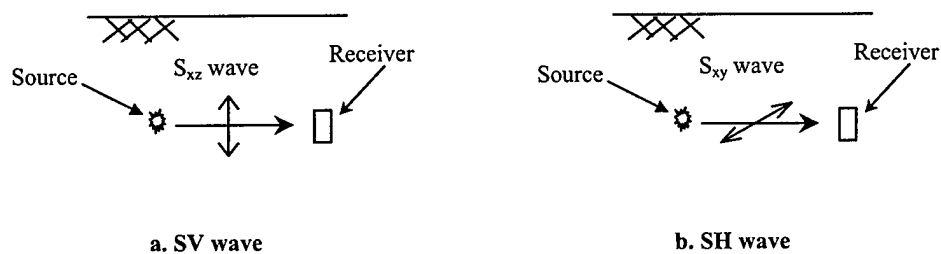


Fig. 3.8 Axes of particle motion and wave propagation differ for SV and SH waves in crosshole testing

Third, unlike the cross-anisotropic model observed during testing in the LSTC, horizontally propagating P and S waves will increase with increases in vertical pressure in a UAB pavement layer due to the coefficient of lateral earth pressure, K . Horizontal pressures could be held constant in the LSTC, but this is an impossibility in the field. Increases in total vertical pressure, σ_v , will result in corresponding increases in total horizontal pressure, σ_h , as illustrated in Figure 3.9. As a result, an increase in vertical pressure will result in an increase in all body wave velocities.

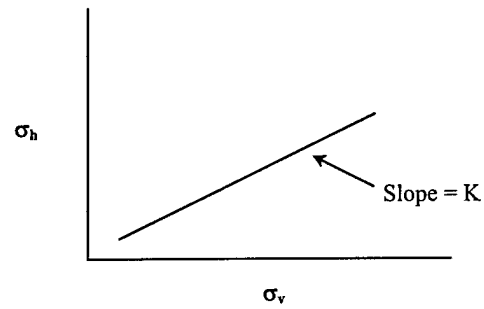


Fig. 3.9 Schematic illustration of the variation in σ_h with σ_v for a constant coefficient of lateral earth pressure at rest

CHAPTER FOUR

Material and Test Site

4.1 Overview

An attempt was made to evaluate the directional stiffnesses in each of the two test sections of the inverted pavement that were constructed in the quarry haul road. This attempt was also made in the traditional pavement section of the haul road. Five test sites were chosen along the haul road in which to conduct crosshole and downhole seismic testing in the UAB layer. Two sites were located in the conventional haul road section (denoted as Sites 1 and 2), two sites were located in the South African base section (denoted as Sites 3 and 4), and one site was located in the Georgia base section (denoted as Site 5). A second site was not placed in the Georgia base section due to the inability to find a second section of base that was thick enough for the installation of the sensors. The first site was disregarded in the end due to unforeseen grading that deposited an unknown quantity of GAB over the sensors. The relative locations of the test sites are shown in Figure 4.1.

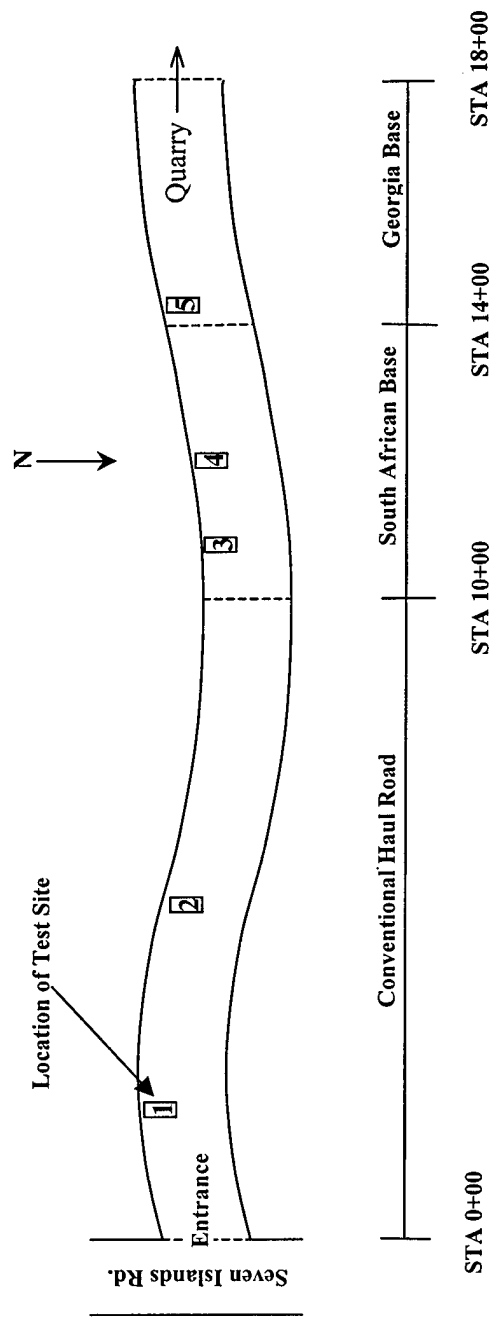


Fig. 4.1 Locations of test sites in haul road

4.2 Graded Aggregate Base

The GAB material used in the UAB layer for all three sections is classified by the GDOT 1993 Specifications as Group II – slag, gravel, granitic and gneissic rocks, quartzite, synthetic aggregate, or any combination thereof. It was produced by the Lafarge Morgan County Quarry, located adjacent to the test road. The GDOT 1993 Specifications requires that the GAB meet the gradation requirements outlined in Table 4.1.

Table 4.1 Gradation Requirements for GAB (GDOT Specifications, 1993 Edition)

Sieve Size	Percent Passing by Weight
2.0 in. (50 mm)	100
1.5 in. (37.5 mm)	97 - 100
0.75 in. (19 mm)	60 - 90
No. 10 (2 mm)	25 - 45
No. 60 (250 μ m)	5 - 30
No. 200 (75 μ m)	4 - 11

4.2.1 Index Properties

The GDOT determined the theoretical maximum dry density to be 136.7 pcf with an optimum gravimetric water content, w , of 6.7%, as shown in Figure 4.2. A summary of the index properties is presented in Table 4.2

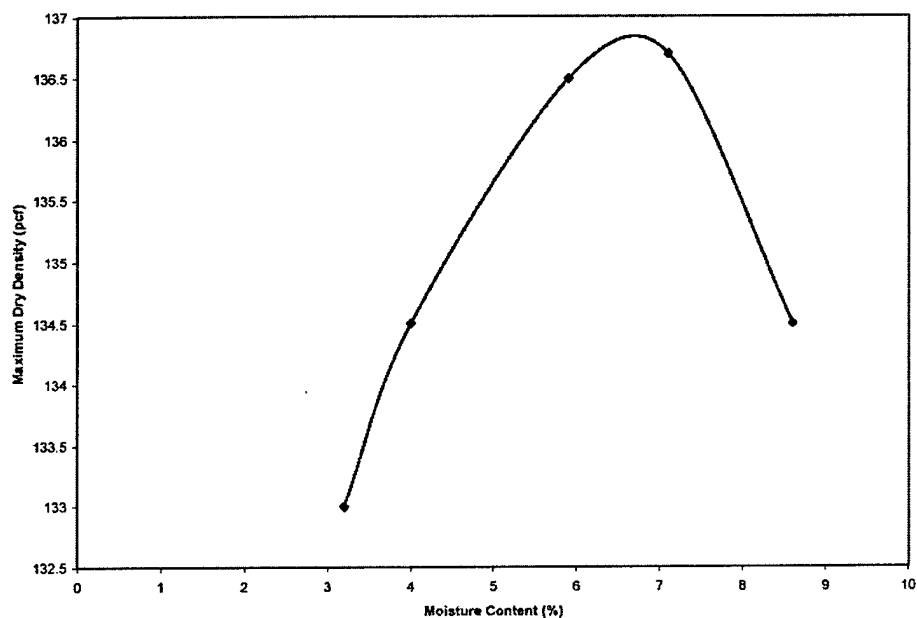


Fig. 4.2 Maximum dry density (Charles Smith, Georgia Department of Transportation)

Table 4.2 Index Properties of GAB from the Lafarge Morgan County Quarry

Liquid Limit	Non-Plastic
Plastic Limit	Non-Plastic
Optimum w	6.7%
ASTM D 1557 (Modified Proctor) Max. Dry Density	136.7 pcf
Mean Grain Size, D_{50}	6.5 mm
D_{10}	0.1 mm
Uniformity Coefficient, $C_u = D_{60}/D_{10}$	100
Unified Soil Classification System Designation	GP - GW

The Lafarge quarry performed a sieve analysis on a sample of the stockpile material in accordance with ASTM C 136-01. It showed 45% passing the #4 (4.75 mm) sieve and 8% passing the #200 (.075 mm) sieve. The fines were non-plastic. The gradation curve, along with upper and lower GDOT limits, is shown in Figure 4.3. The gradation data are also presented in Table 4.3.

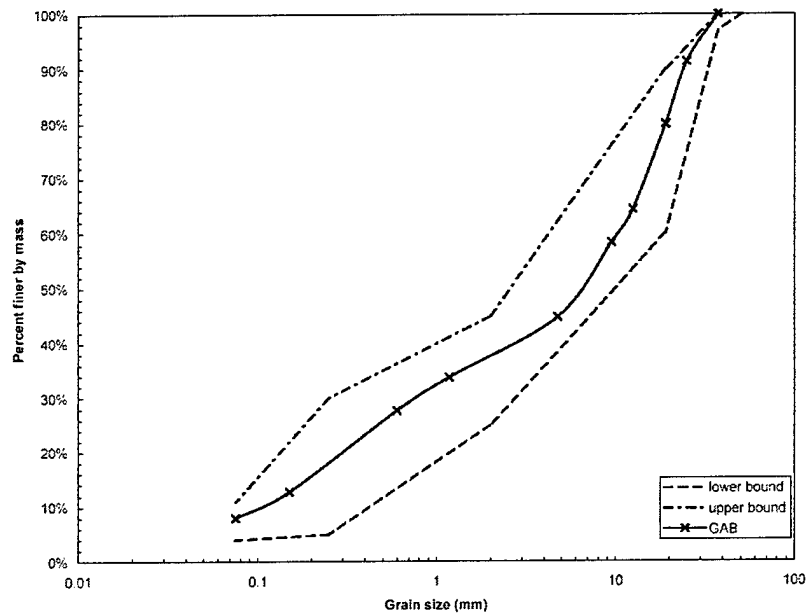


Figure 4.3 Gradation curve for the GAB from the Lafarge Morgan County Quarry (Carol Cook, Lafarge North America)

Table 4.3 Gradation of GAB from the Lafarge Morgan County Quarry

Sieve Size		% Passing
	mm	
1.5 in.	37.5	100%
1 in.	25.4	91%
0.75 in.	19	80%
0.5 in.	12.5	64%
3/8 in.	9.5	58%
#4	4.75	45%
#16	1.18	34%
#30	0.6	28%
#100	0.15	13%
#200	0.075	8%

4.2.2 In-Situ Density and Gravimetric Water Content

The GDOT determined the in-situ wet and dry unit weights and the water contents for the two inverted test sections immediately after construction using the Sand Cone Method (ASTM D1556) and a Troxler 3430 Nuclear Density Gauge (NDG) (AASHTO T310-00). The unit weight and water content data are presented in Table 4.4, and the test locations are shown in Figure 4.4. The dry unit weight and water content for the traditional section were assumed to be the aforementioned maximum values of 136.7 pcf and 6.7%. The calibration values used in calibrating the NDG for dry unit weight and water content were calculated using the average of the three sand cone dry unit weights. The GDOT also determined the water contents for all three sections using an NDG. These values are presented in Table 4.5. It is interesting to note that the Georgia procedure produced a GAB layer with a dry unit weight that is slightly above that produced

with the South African procedure. The differences in the unit weights determined from the sand cone and NDG methods for the South African section are due to the large variances in dry unit weights used in calculating the calibration factor.

Table 4.4 Density and Gravimetric Water Content Data from the Three Test Sections

a. In-situ Measurements - sand cone (ASTM D 1556-00)

South African - after construction

Station	wet unit wt. (pcf)	dry unit wt. (pcf)	w (%)
13+00	143.8	135.5	6.1

Georgia - after construction

Station	wet unit wt. (pcf)	dry unit wt. (pcf)	w (%)
14+50	151.0	143.6	5.1
16+00	156.6	149.6	4.7
avg.	153.8	146.6	4.9

b. In-situ Measurements - nuclear density gauge (SA AS 1289.5.8.1)

South African - after construction

Station	wet unit wt. (pcf)	dry unit wt. (pcf)	w (%)
10+30	147.2	140.1	5.9
11+50	151.3	144.2	5.9
12+00	148.6	140.5	5.9
13+50	150.9	142.6	5.9
avg.	149.5	141.9	5.9

Georgia - after construction

Station	wet unit wt. (pcf)	dry unit wt. (pcf)	w (%)
14+50	150.6	143.5	5.9
15+50	152.0	144.1	5.9
16+50	150.8	143.2	5.9
17+50	146.8	139.3	5.9
avg.	150.05	142.5	5.9

Table 4.5 Gravimetric Water Contents

Date of Test	Location	w (%)
1/24/02	Site 2	4.78
1/24/02	Site 3	4.93
1/24/02	Site 5	5.70

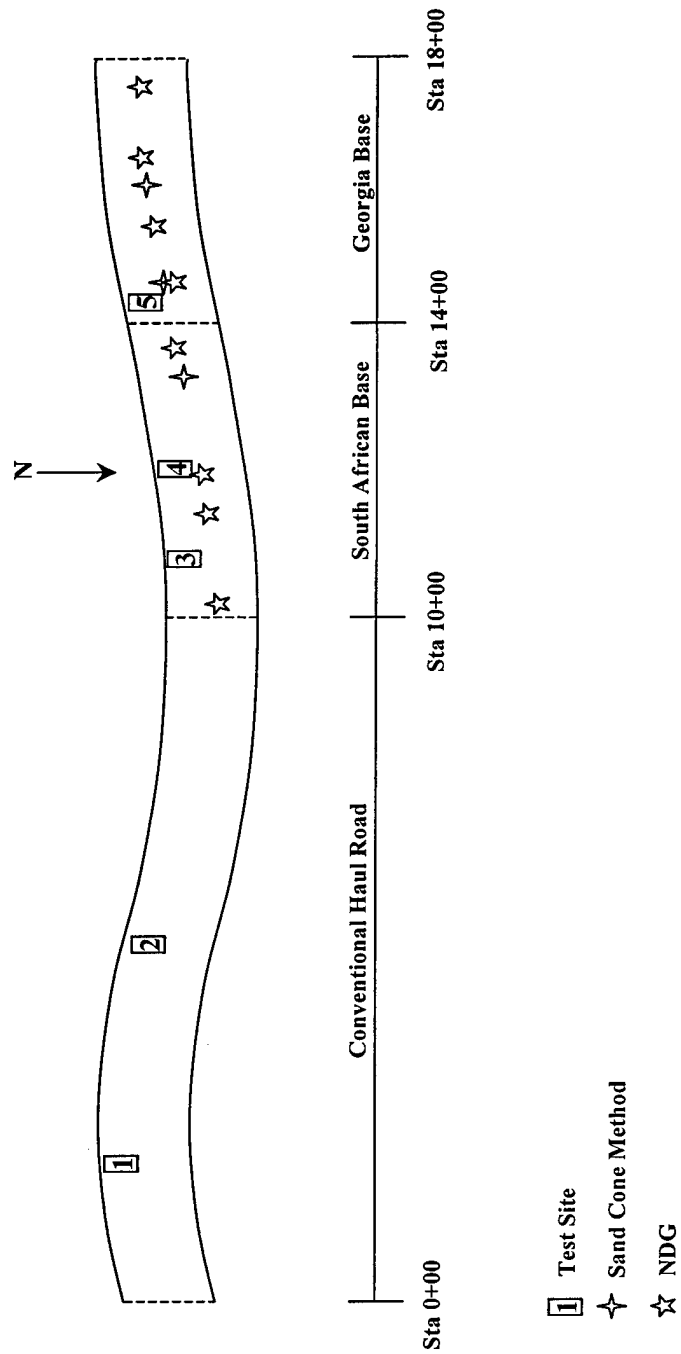


Fig. 4.4 Locations of Sand Cone and NDG tests at the haul road

CHAPTER FIVE

In-Situ Seismic Testing and Field Equipment

5.1 Overview

In-situ seismic testing was performed using embedded sensors in the UAB layer at each of the five previously noted test sites (see Figure 4.1). The embedded sensors were installed prior to the placement of the HMA course during the first site visit on 17 to 20 December 2001. Also installed at each test site was a section of PVC pipe that served as a source casing for the crosshole testing. Miniaturized versions of traditional crosshole and downhole tests were conducted in an attempt to determine the directional stiffnesses at each of the five sites and how these stiffnesses changed under different external loads. The traditional and miniaturized testing methods are discussed below.

5.1.1 Traditional Crosshole Seismic Method

The crosshole method is an intrusive, active method of seismic body wave testing based on time-of-travel measurements of generated S and P waves. The sources and receivers are placed at the same depth in adjacent boreholes, as shown in Figure 5.1.

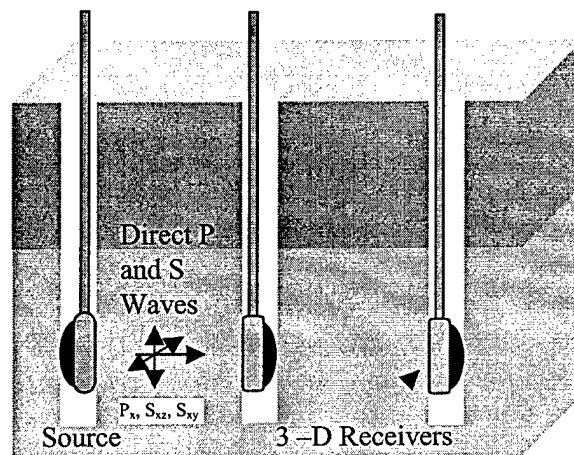
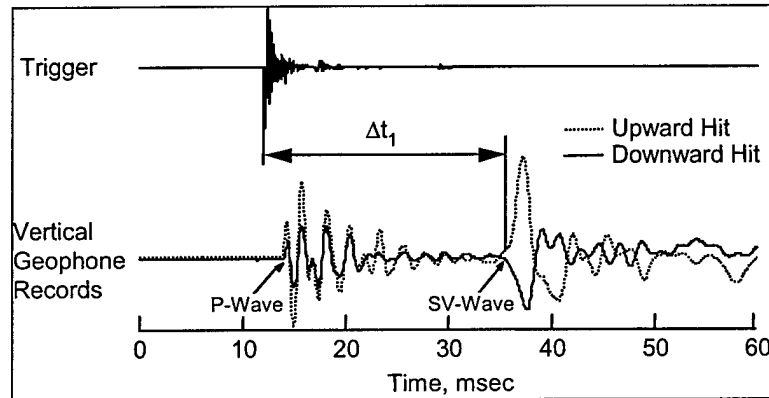
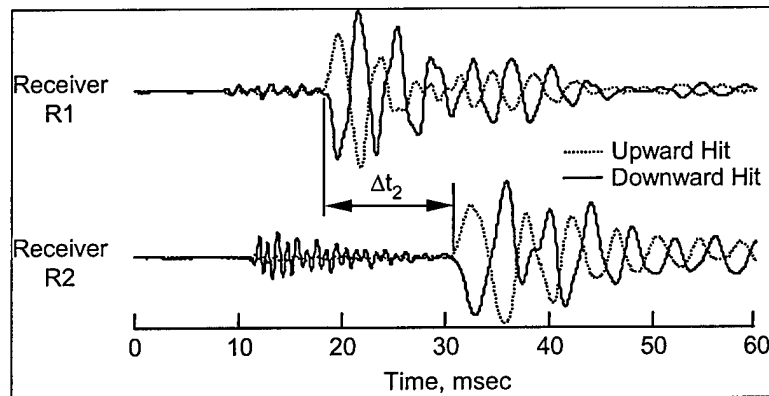


Fig. 5.1 Field arrangement for a crosshole test (Stokoe and Santamarina, 2000)

Travel times from the source to receivers (direct travel times) and travel times between receivers (interval travel times) were measured. Examples of direct and interval travel times are shown in Figures 5.2a and 5.2b, respectively, for full-scale tests performed by Fuhrman (1993) at a site on Treasure Island near San Francisco, California. Full-scale tests are defined as those tests involving distances between adjacent boreholes on the order of 10 to 15 ft (3 to 5 m).



a. Record illustrating a direct travel time measurement of an SV wave



b. Record illustrating an interval travel time measurement of an SV wave

Fig. 5.2 Example S-wave records measured in traditional crosshole testing using upward and downward impacts to help identify the initial SV-wave arrival (from Fuhrman, 1993). Note: the P-wave signal may also reverse, depending on the directivity of the source and the relative position of the receiver (Stokoe and Santamarina, 2000)

In this example, horizontally propagating SV waves were created by applying vertical impacts to the side of the borehole using a wedged source.

Wave arrivals were monitored using vertically oriented velocity transducers (geophones) as receivers. S-wave velocities are calculated by dividing the distance between the boreholes at the test depth by the respective travel times (Δt_1 or Δt_2) after any necessary calibration constants were applied.

5.1.2 Traditional Downhole Method

The downhole method is based on the same principles as the crosshole method, only the source is located on the surface of the deposit and the sensors are located directly over each other at different depths in the soil mass, as illustrated in Figure 5.3.

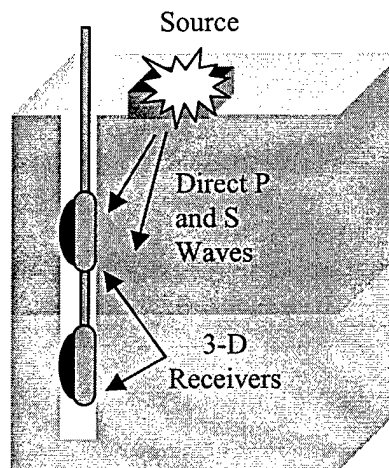


Fig. 5.3 Field arrangement for a downhole test (Stokoe and Santamarina, 2000)

Travel distances between the source and receivers are assumed to be straight ray paths, though further analysis may reveal refracted ray paths. In the traditional tests, source-receiver distances commonly range from 5 to 10 ft (1.5 to 3 m) at the

first measurement depth to several 100 ft (on the order of 30 to 150 m) at the deepest measurement depth.

5.1.3 Miniaturized Crosshole and Downhole Methods

While the traditional crosshole and downhole methods involve making measurements of travel paths in tens to hundreds of feet, the miniaturized crosshole and downhole methods utilized on the quarry road involved travel paths of a few inches. The actual measurements and methods are discussed later in this chapter and are sometimes referred to as miniaturized versions of the traditional tests.

5.2 Test Equipment

Two types of embedded sensors were placed in each UAB layer during construction. Each sensor type was constructed with Geospace 28.5-Hz geophones. The first type was a 3-dimensional (3-D) sensor consisting of three, orthogonally oriented geophones that were used in crosshole testing. The geophones (receivers) were oriented in such a way as to detect horizontally propagating P waves (termed PH waves) and horizontally propagating S waves with either horizontal or vertical particle motion, termed SHH waves and SHV waves, respectively. These waves are illustrated in Figure 5.4.

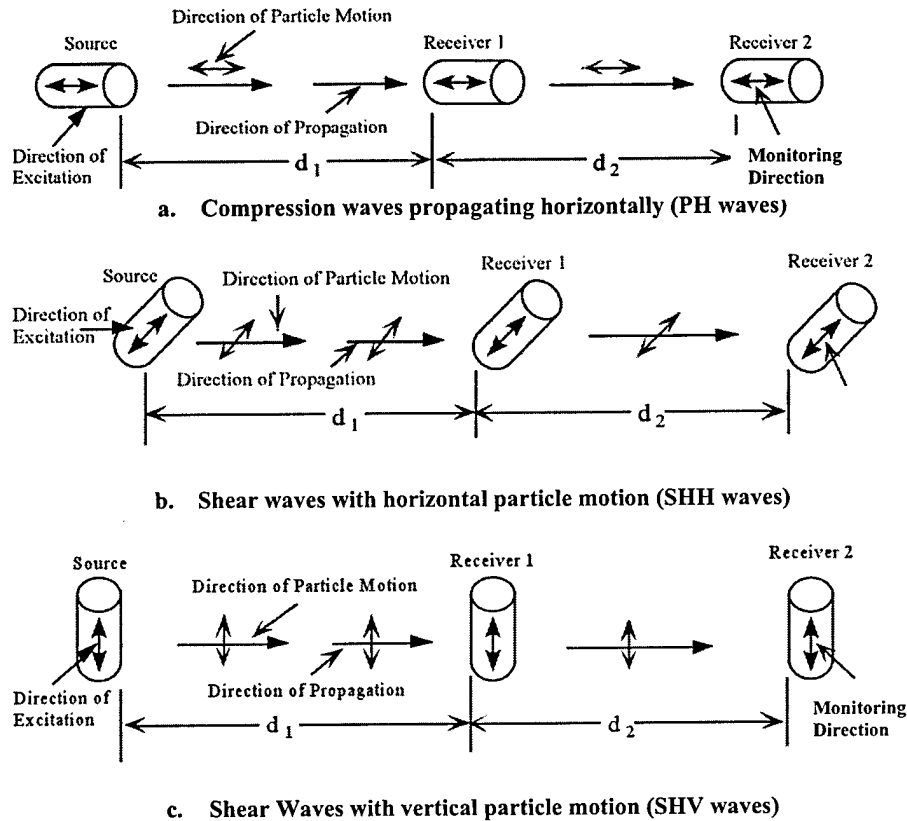


Fig. 5.4 Illustration of geophone arrangement used for measurement of body waves propagating in a horizontal direction (Stokoe and Lee, 1991)

The three geophones used to build the 3-D receivers were epoxied into a 2.5-in. (6.4-cm) diameter by 1-in. (2.5-cm) thick, pre-drilled acrylic template (Figure 5.5a). The two horizontally oriented geophones were placed at 90 degrees to each other, and the third geophone was placed orthogonal to the first two. Each geophone was soldered to a pair of shielded wires, which were in turn soldered to

a three-pair shielded cable that was connected to an Agilent 3567A Dynamic Signal Analyzer during testing. The template and geophones were then epoxied into a capped, 3.5-in. (8.9-cm) diameter (outside) by 2-in. (5.1-cm) tall section of PVC pipe, filled with a silicone caulk, and sealed (Figure 5.5b).

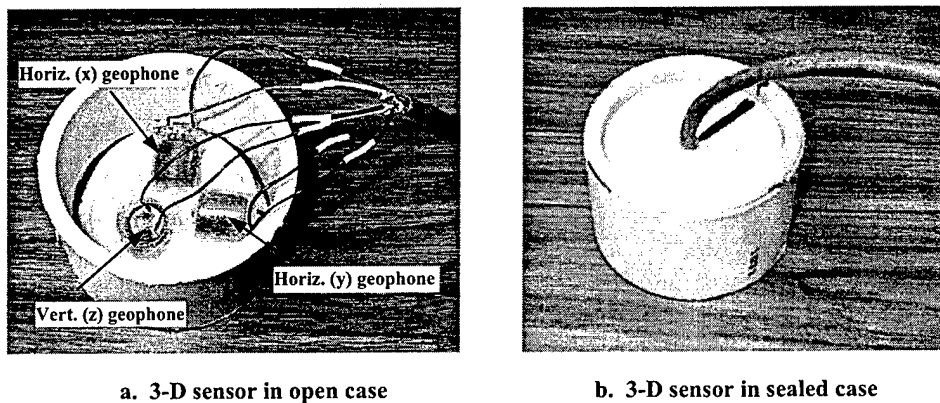
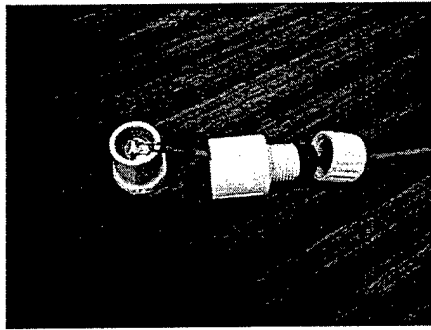
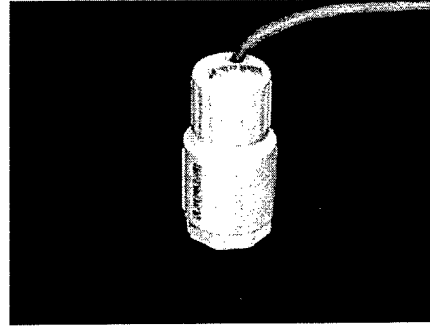


Fig. 5.5 3-D sensor used in crosshole testing

The second type of sensor was a 1-dimensional (1-D) sensor that was constructed with a single geophone epoxied into a 1.25-in. (3.2-cm) diameter (outside) by 2.75-in. (7-cm) tall PVC case (Figures 5.6a and b), and filled with silicone caulk. A two-pair shielded cable was used to connect the sensor to the analyzer during testing. This sensor was used in pairs and oriented vertically so as to detect vertical P waves (termed PV waves) in downhole testing.



a. 1-D sensor in open case



b. 1-D sensor in sealed case

Fig. 5.6 1-D sensor used in downhole testing

5.3 Test Site

5.3.1 Embedded Instrumentation

Each test site was composed of a 3.5-in. (8.9-cm) diameter (outside) by 4-in. (10.2-cm) tall section of PVC pipe (designated as S in Figure 5.7 for source) that served as a source casing for the crosshole test. Two 3-D sensors (denoted R1 and R2 in Figure 5.6) were placed at two different distances (denoted as d_1 and d_2) from the source hole (at an included angle of about 45 degrees) in order to measure PH-, SHH-, and SHV-wave velocities. Two, 1-D sensors (denoted R3, top, and R4, bottom) were placed vertically in the same location (one over the other) at the same distance (denoted d_3) from the source hole in order to measure PV-wave velocities created by a hammer impacting the ground surface at distances of 3 in. (7.6 cm), 6 in. (15.2 cm), and 9 in. (22.9 cm) from the top of these sensors.

A typical test site is illustrated in Figure 5.7. Values for d1, d2, and d3 for each test site are presented in Table 5.1.

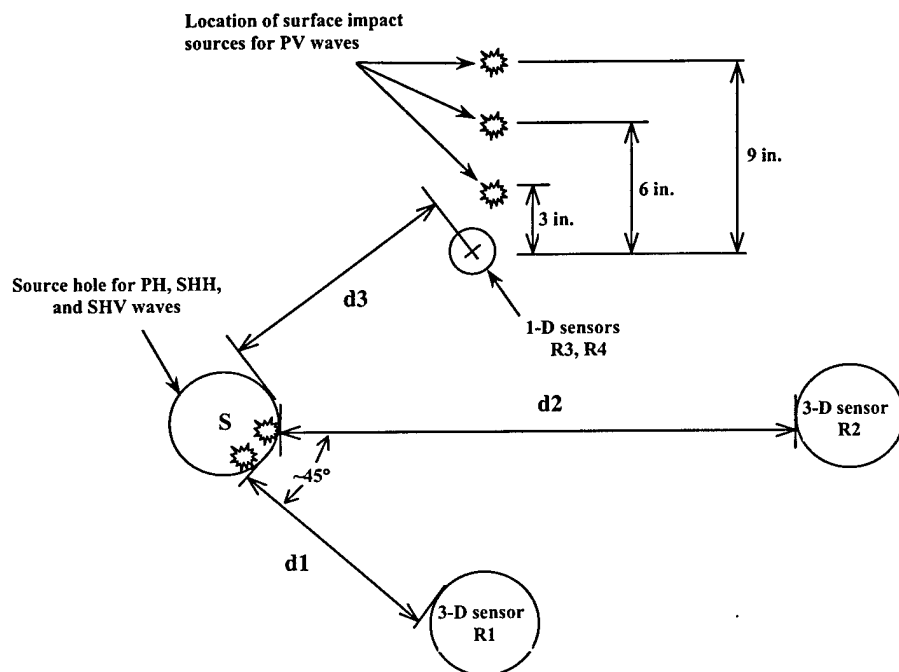


Fig. 5.7 Source hole and sensors for a typical test site

Table 5.1 Test Site Dimensions

Site	d1 (in./cm)	d2 (in./cm)	d3 (in./cm)
2	5.5/14	10.8/27.4	7.5/19.1
3	5.0/12.7	11.0/27.9	8.5/21.6
4	5.25/13.3	10.75/27.3	7.5/19.1
5	5.4/13.7	10.5/26.7	7.3/18.5

The values of d_1 and d_2 were used for both PH and SHH waves even though the point of impact was slightly further away for the SHH waves. Analysis of the data (discussed in Chapter 8) confirmed the use of the same d_1 and d_2 values for PH and SHH wave analysis.

5.3.2 Placement of Embedded Instrumentation

After the GAB layer was compacted, installation of the source casing and sensors required the use of an Acker Drill mounted on a Ford HD350 truck. The drill was used to core four, 4-in. (10.2-cm) diameter holes about 4 in. into the UAB in the pattern illustrated in Figure 5.7. This operation is shown in Figure 5.8. The 3-D sensors were oriented so that one geophone was in line with the ray path and two geophones were orthogonal to it, as illustrated in Figure 5.9. The two, 1-D sensors were placed vertically, one over the other, as illustrated in Figure 5.10. A Portland cement grout was used to secure the source casing, while the other sensors were backfilled in place with the excavated GAB (Figure 5.11).

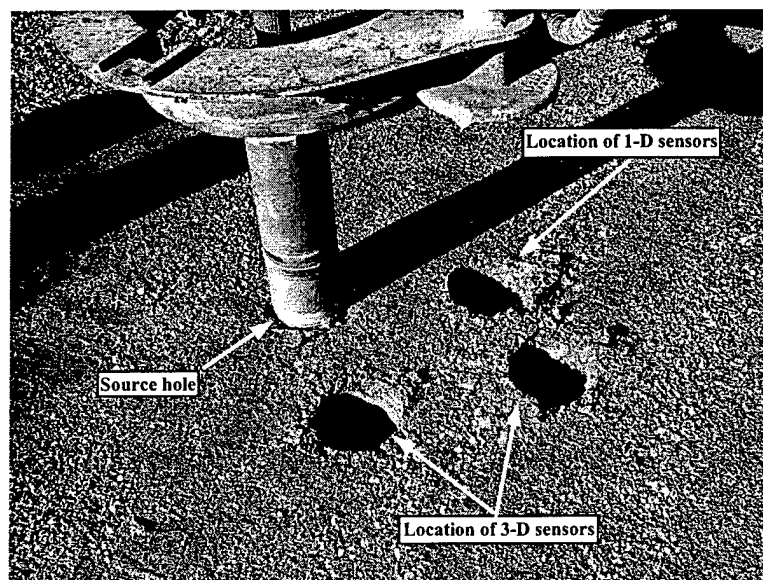
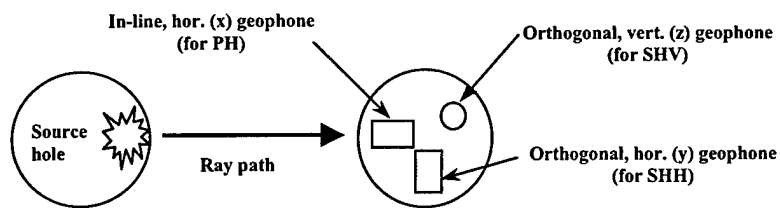
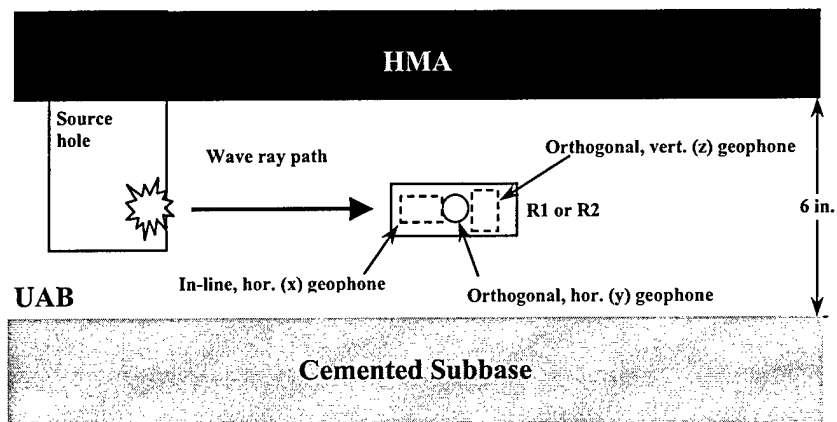


Fig. 5.8 Coring down 4 in. into the compacted UAB.



a. 3-D sensor plan view



b. 3-D sensor side view

Fig. 5.9 3-D sensor geophones in-line and orthogonal to wave ray path in UAB layer

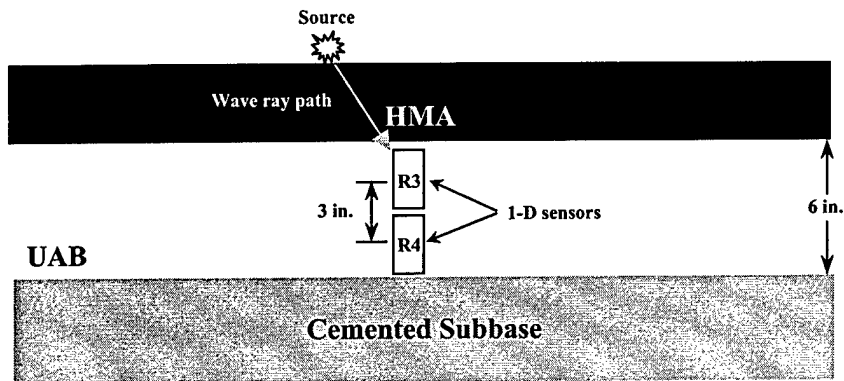


Fig. 5.10 1-D sensors placed vertically in UAB layer

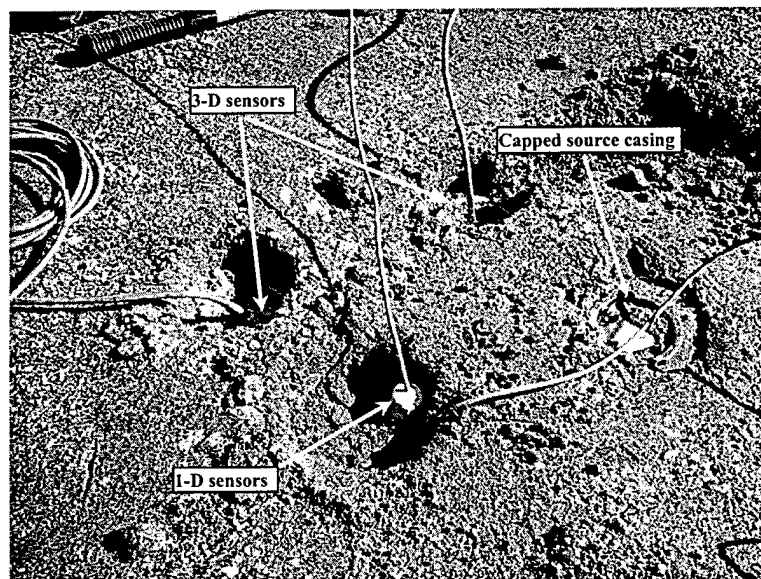


Fig. 5.11 Installation of source casing and embedded sensors

Trenches for the cables were then dug around the sensors and away from the area through which waves would propagate. The trenches were backfilled with the excavated GAB (Figure 5.12).

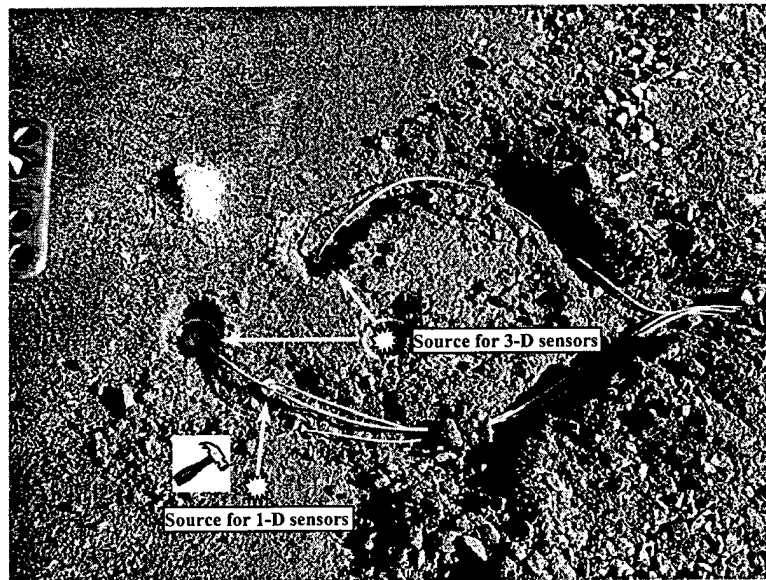


Fig. 5.12 Cable trenches with superimposed sources and P wave and S wave ray paths

A 3-in. (7.6-cm) layer of HMA was placed over the entire road after the construction of all five test sites was completed. The source crosshole casing was filled with sand and capped to protect it from infiltration by the HMA, which was placed the next day after the source casing was installed. Existing fence posts and driven stakes near the haul road were marked and used to sight-in the positions of the source holes after the HMA layer was placed.

5.4 Seismic Testing and Typical Records

A return trip was made approximately one month after the installation of the sensors and placement of the HMA, from 24 through 26 January 2001, in order to conduct the in-situ seismic testing. The source holes were easily relocated and excavated using the Acker Drill mounted on a Ford HD350 truck. The cardboard template originally used to mark the locations of the source holes and sensors for placement in the UAB layer was then used to mark the locations of the sensors with painted circles on top of the HMA surface. An excavated source hole and marked sensor locations at Site 2 are shown in Figure 5.13.

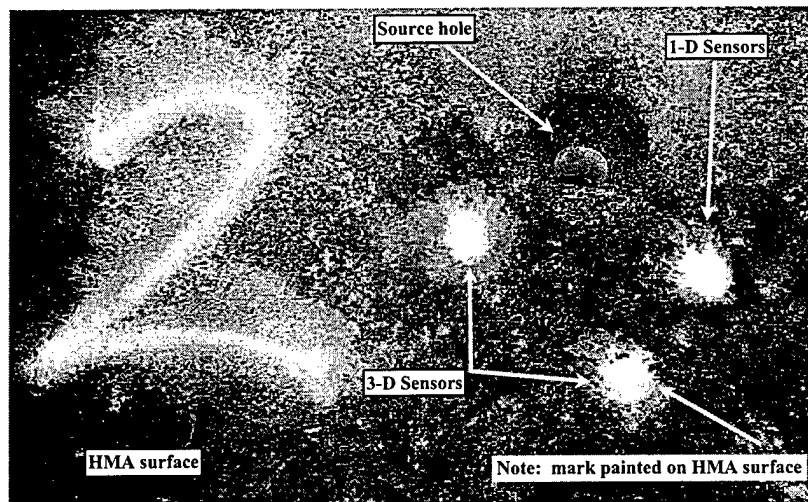


Fig. 5.13 Site 2 source hole and embedded sensor locations marked on HMA surface

Crosshole and downhole seismic tests were conducted under the following four loading conditions: (1) zero external load, (2) front right tire of a Chrysler

Town Van (1270 lbs/580 kg), (3) front right tire of an empty International Dump Truck (5670 lbs/2600 kg), (4) front right tire of the dump truck fully-loaded (variable). The van and truck loadings are shown in Figures 5.14 and 5.15, respectively. The weights of the van and truck were determined by taking half of the weight of the front wheels as measured on a truck scale at the quarry. The weights of the loaded trucks can be found in Table 5.2.



Fig. 5.14 Testing with a van load



Fig. 5.15 Testing with a dump truck load

Table 5.2 Loading from a Fully-Loaded Dump Truck

Site	2	3	4	5
Wt. under front right wheel of fully-loaded dump truck (lbs./kg)	10,280/ 4660	10,010/ 4540	8880/ 4030	8,370/ 3800

5.4.1 PH-Wave Velocities

PH waves were created by applying horizontal impacts to the side of the source casing (3 in. [7.6 cm] down from the top edge) in the direction of wave propagation using a small hammer equipped with a PCB 303A12 accelerometer

as a trigger signal. This source hammer is shown in Figure 5.16. Impacts were directed toward each 3-D sensor, R1 and R2, as shown in Figure 5.17.

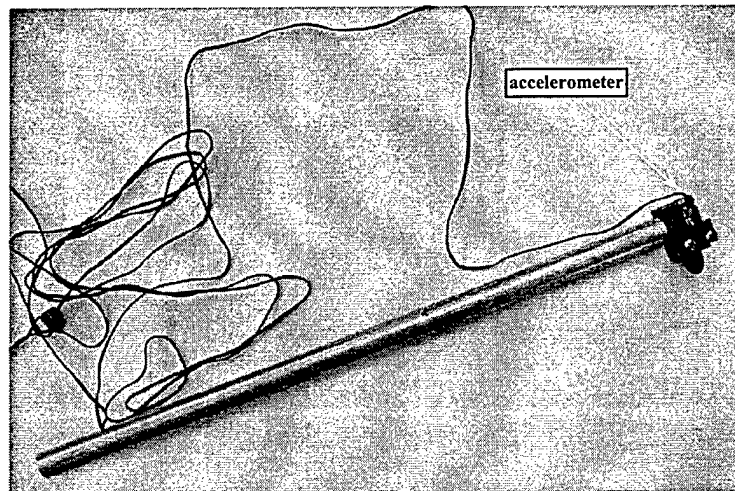


Figure 5.16 Source hammer and accelerometer

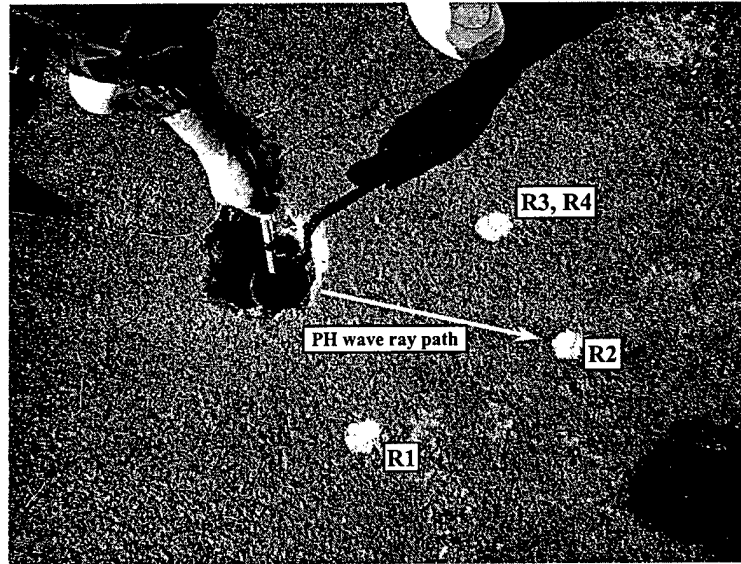


Fig. 5.17 Using a small hammer to create a PH wave

Trigger times were recorded with the accelerometer attached to the hammer and connected to the analyzer. A typical trigger record is shown in Figure 5.18.

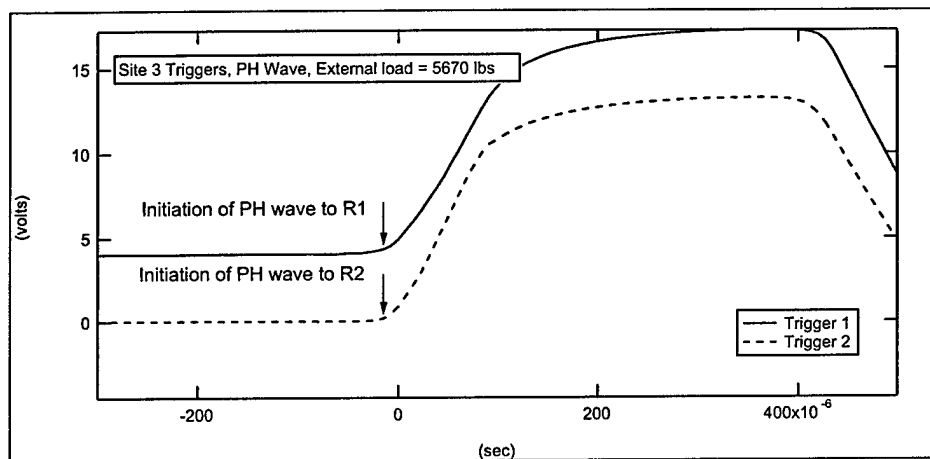


Figure 5.18 Typical trigger record for PH wave

Wave arrivals were measured using the horizontal (x) geophone oriented in-line with the wave ray path in the 3-D sensor (as illustrated in Figure 5.9). PH waves were created and measured for each 3-D sensor for each of the previously-mentioned loading conditions. A typical record for a PH-wave arrival is shown in Figure 5.19.

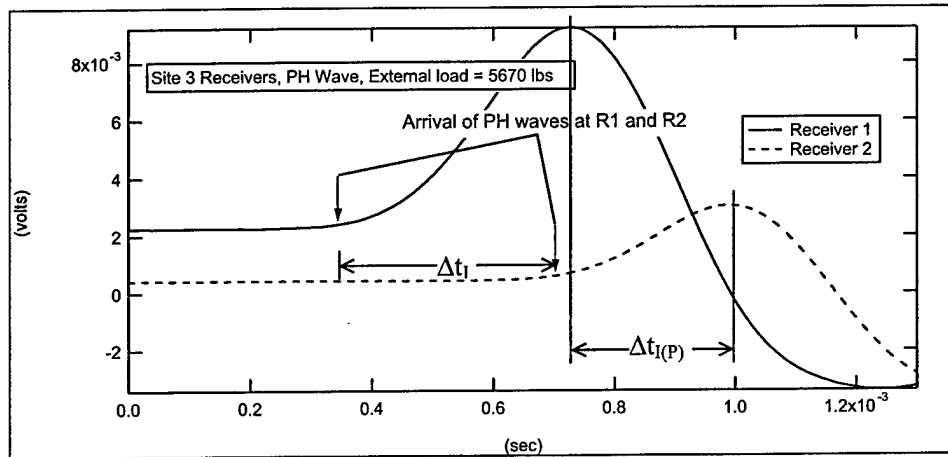


Fig. 5.19 Typical record for PH-wave arrival

Three PH-wave velocities were calculated for each site. The first velocity was for the wave travel between the source and R1, calculated by dividing the distance between the source and R1 (noted as d_1 in Figure 5.7) by the direct travel time (the difference between the trigger and the wave arrival) between the source and R1. The second velocity was for the wave travel between the source and R2, calculated by dividing the distance between the source and R2 (d_2 in Figure 5.7) by the direct travel time between the source and R2. A calibration factor for the wave travel through the PVC encasing the source hole and receiver (along with the silicone caulk filling the receiver) was determined in the lab by attaching a receiver directly to the casing and recording the travel time for a PH wave, as illustrated in Figure 5.20. This time was subtracted from each direct travel time.

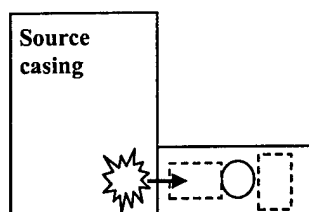


Figure 5.20 Determining a calibration factor for PH and SHH waves

The third velocity was for the wave travel between the two sensors (as if they were in line), calculated by dividing the difference between d_2 and d_1 by the interval travel time between the two receivers (Δt_i in Figure 5.19). There was general scatter for the interval velocities, being both larger and smaller than the direct velocities for each of the sites. The PH-wave velocities calculated from the peak intervals ($\Delta t_{i(p)}$ in Figure 5.19) were very similar to those calculated from Δt_i . The PH-wave velocities and associated loading conditions used in characterizing the UAB layer can be found in Appendix A.

5.4.2 SHH-Wave Velocities

SHH waves were created by applying horizontal impacts to the side of the source casing (3 in. [7.6 cm] down from the top edge) perpendicular to the direction of wave propagation using the same equipment as previously described. Wave arrivals were measured using the horizontal (y) geophone oriented

perpendicular to the wave ray path in the 3-D sensor (as illustrated in Figure 5.9). Two SHH waves, transverse right and transverse left, denoted SHH(R) and SHH(L), respectively, were created and measured for each 3-D sensor for each of the previously-mentioned loading conditions. Typical records for SHH(R) and SHH(L) wave arrivals are shown in Figures 5.21 and 5.22, respectively. Superimposing the wave arrivals over each other generates "butterfly" curves, as shown in Figure 5.23. The SHH-wave velocities are calculated in the same manner as PH-wave velocities, using a calibration factor determined in the same manner as for the PH wave, except the receiver was rotated so that the geophone used to detect the SHH wave was in line with the hammer tap. There was general scatter for the interval velocities, being both larger and small for each of the sites. The SHH-wave interval velocities calculated from the peak intervals ($\Delta t_{l(p)}$ in Figure 5.23) were very similar to those calculated from the initial intervals (Δt_l in Figure 5.23). The SHH-wave velocities and associated loading conditions used in characterizing the UAB layer can be found in Appendix A.

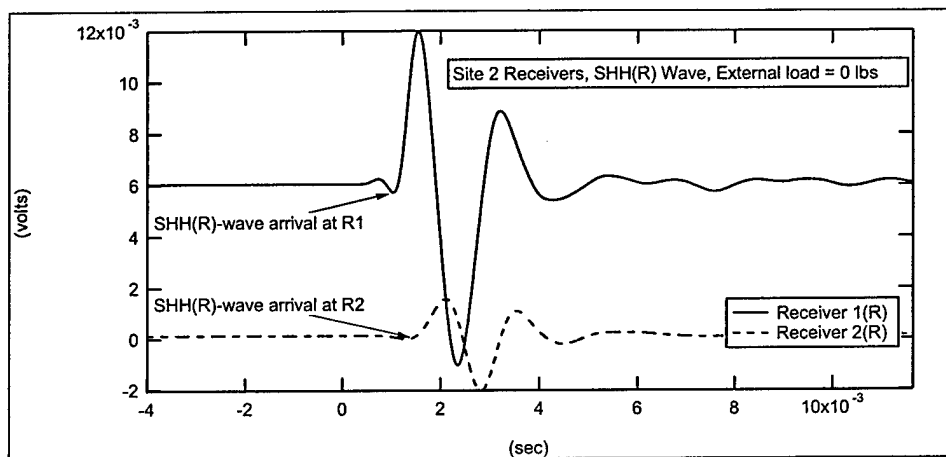


Fig. 5.21 Typical record for SHH(R)-wave arrival

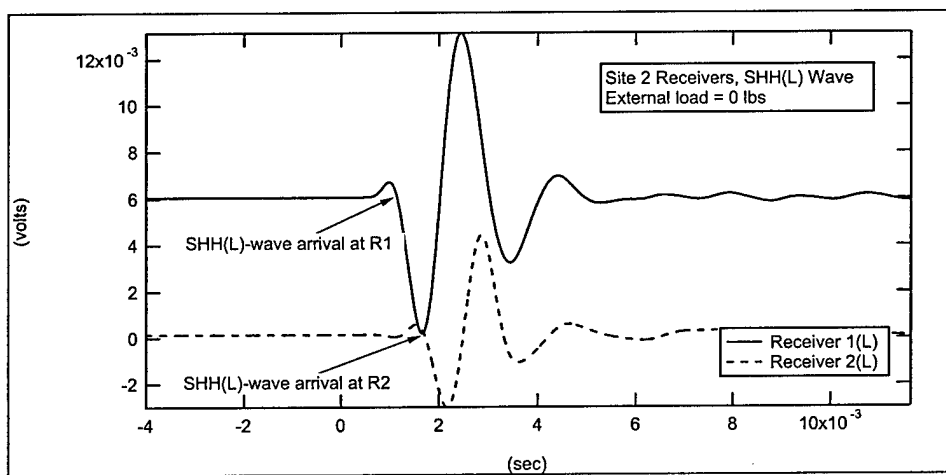


Fig. 5.22 Typical record for SHH(L)-wave arrival

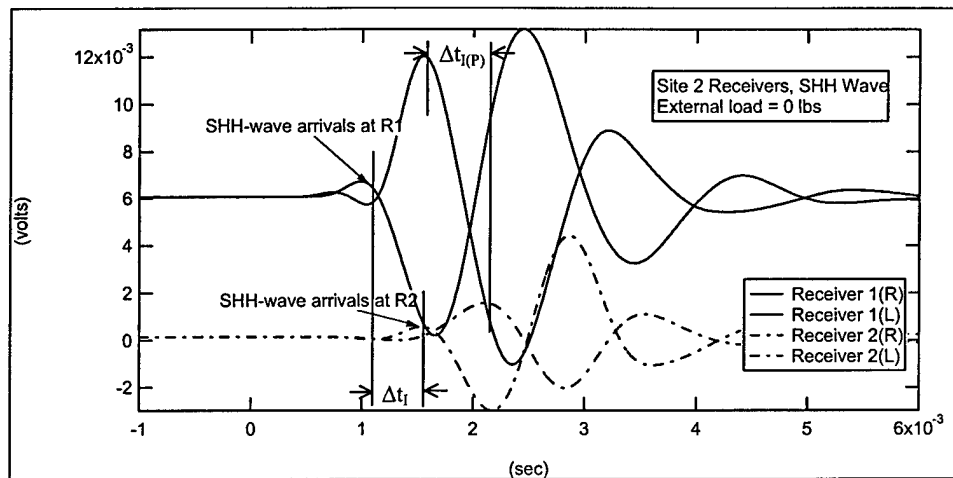


Fig. 5.23 Typical "butterfly" curves for SHH-wave arrival

5.4.3 SHV-Wave Velocities

SHV waves were created by applying vertical impacts to the side of the borehole using an aluminum wedged source, as shown in Figure 5.24. A PCB 303A02 accelerometer was attached to the wedged aluminum cylinder to record trigger times.



Fig. 5.24 Using a wedged source to create an SHV wave

Wave arrivals were measured using the vertical (z) geophone oriented perpendicular to the wave ray path in the 3-D sensor (as illustrated in Figure 5.9). Two SHV waves, transverse up and transverse down, denoted SHV(U) and SHV(D), respectively, were created and measured for each 3-D sensor for each of the previously-mentioned loading conditions.

Unfortunately, the poor quality of the wave arrival records precluded any reliable calculation of the SHV-wave velocities. A typical record and expected arrival time are shown in Figure 5.25.

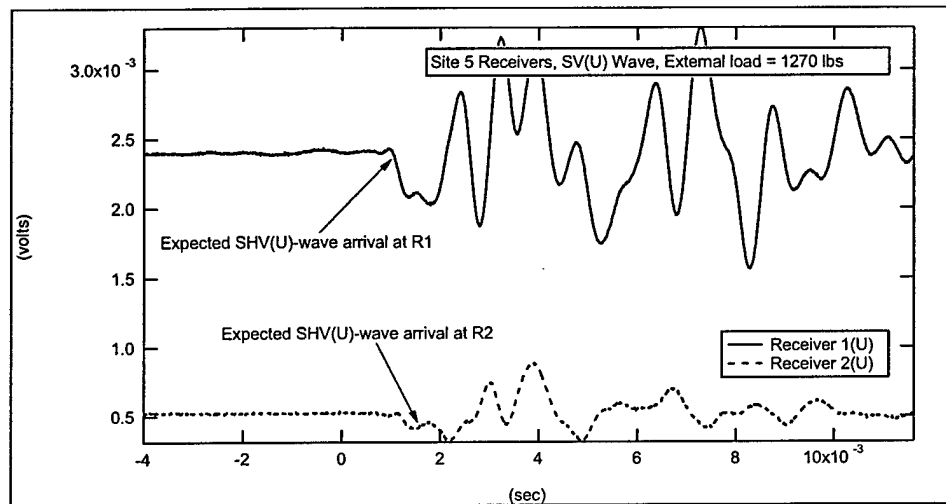


Figure 5.25 Typical record for SHV(U)-wave arrival

The poor-quality records are most likely due to the horizontal layering of the pavement system. The vertical impacts to the side of the borehole used to produce SHH and SHV waves also produce other SH and SV waves which travel in all directions. Unlike an incident SH wave that only produces reflected SH waves when it encounters an adjacent, horizontally-layered elastic medium, an incident SV wave will produce reflected SV and P waves when it encounters an elastic medium (Richart et al, 1970), as illustrated in Figure 5.26. Since these reflected P-waves travel faster than the SHV wave, they can arrive at the sensor before the generated SHV wave, disrupting the wave arrival record.

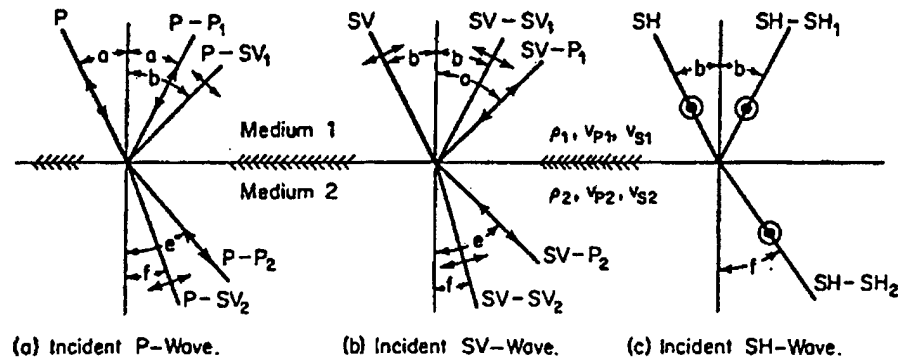


Fig. 5.26 Incident and reflected waves in horizontal layering (Richart et al, 1970)

5.4.4 PV-Wave Velocities

PV waves were created by hitting the HMA surface with a 4-oz (113-g) ball-peen hammer at distances of 3 in. (7.6 cm), 6 in. (15.2 cm), and 9 in. (22.9 cm) from the horizontal projection of the 1-D sensors on the HMA surface, as shown in Figure 5.27. A PCB 303A02 accelerometer was attached to the hammer to record trigger times.

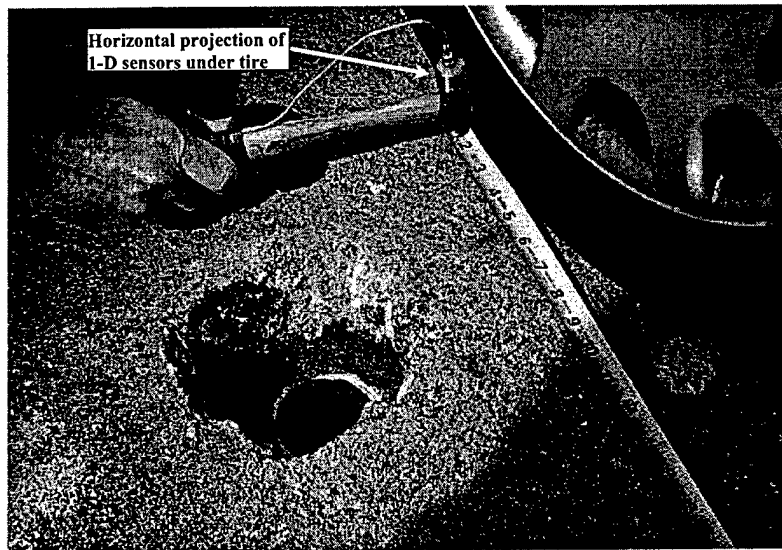


Fig. 5.27 Using a small ball-peen hammer to create a PV wave

The PV-wave velocities obtained from this testing were deemed to be unreliable due to the spacing of the 1-D sensors with respect to each other (see Figure 5.10). The distances between the bottom of the HMA layer, R3, and R4 were too small to allow good representations of the UAB layer. Additionally, the wave was found to be very complicated and its exact travel path unknown. A typical record and expected arrival times are shown in Figure 5.28.

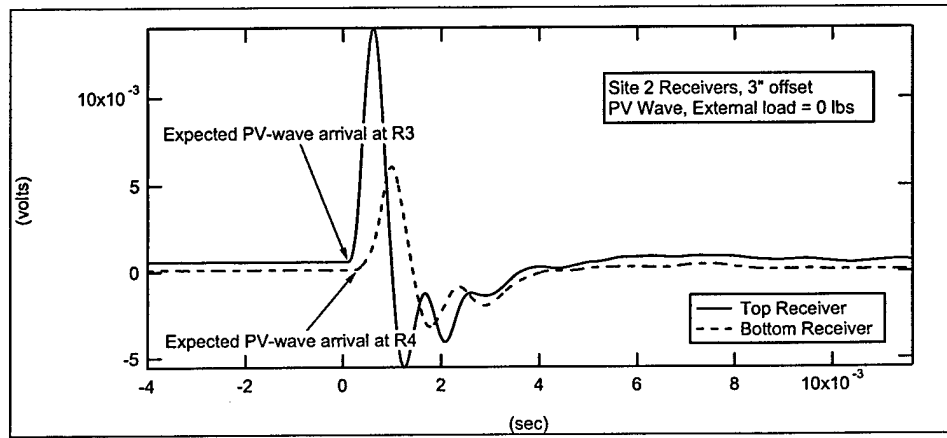


Figure 5.28 Typical record for PV-wave arrival

CHAPTER SIX

Unsaturated Soil Mechanics and the Soil-Water Characteristic Curve

6.1 Overview of Unsaturated Soil Mechanics

The UAB layer of the quarry haul road lies well above the water table, in what is commonly known as the unsaturated zone. Due to negative pore-water pressures and the wide range of degrees of saturation possible in the soil, the engineering behavior of an unsaturated soil can be more difficult to describe than that of a saturated soil. An unsaturated soil can vary in degree of saturation, S , from 100% in the capillary zone and below to completely dry near the surface, as illustrated in Figure 6.1. Unsaturated soil mechanics focuses primarily on the zone where the air and water phases are continuous, often called the two-phase zone in the pore space (Fredlund, 2000).

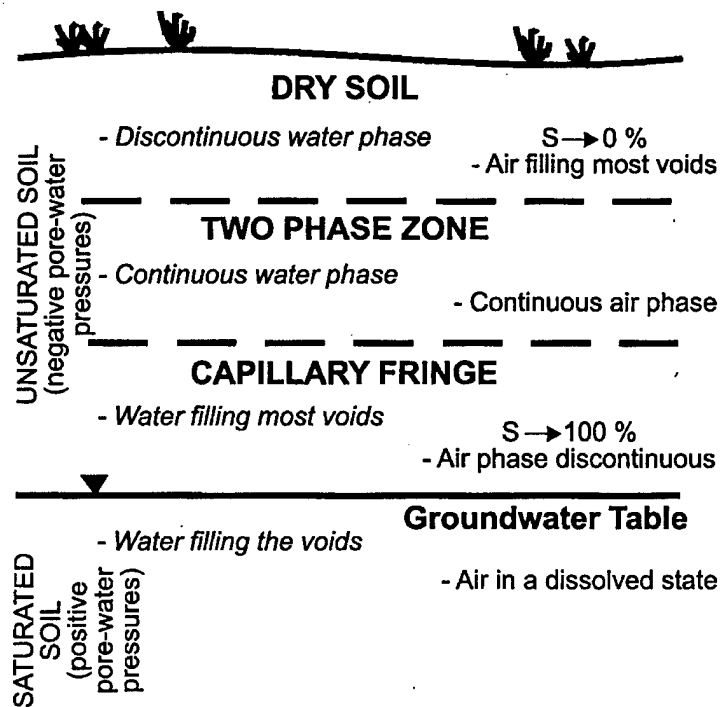


Fig. 6.1 Classification of the regions within a saturated-unsaturated soil profile (Fredlund, 2000)

6.1.1 Stress State Variables

The widely accepted stress state variables for an unsaturated soil are the net normal stress, $(\sigma - u_a)$, where σ is the total stress and u_a is the pore-air pressure, and the matric suction, $(u_a - u_w)$ where u_w is the pore-water pressure (Fredlund, 2000). These two stress states, and associated smooth transition between the saturated and unsaturated zones, are illustrated in Figure 6.2. The

complete stress state acting in three dimensions at a point is illustrated in Figure 6.3.

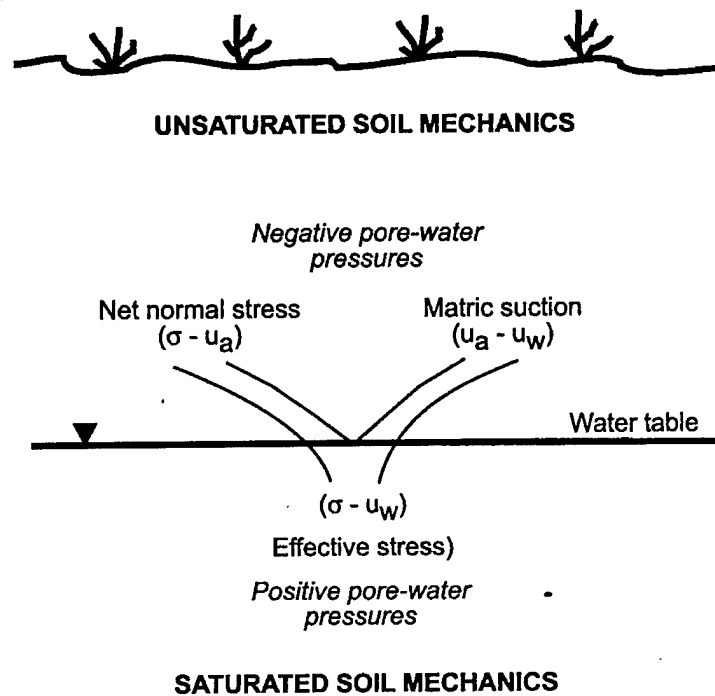


Fig. 6.2 Separation of saturated and unsaturated soil mechanics based on the stress state description (Fredlund, 2000)

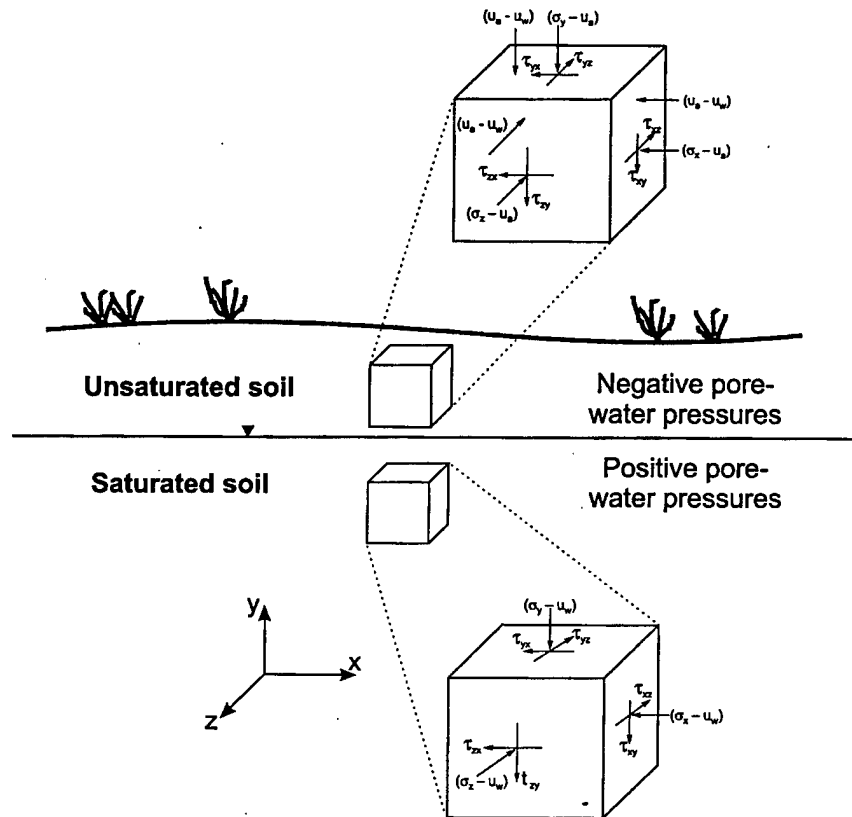


Fig. 6.3 Elements showing the stress state at a point in a saturated soil and unsaturated soil (Fredlund, 2000)

6.1.2 Total Suction

The total suction (or soil suction), ψ , comprises two components, the matric suction, $(u_a - u_w)$, and the osmotic suction, π :

$$\psi = (u_a - u_w) + \pi \quad (6.1)$$

Matric suction is affected by environmental changes and is more relevant for low suctions (less than residual saturation, S_r , conditions). Osmotic suction is related to the salt content in the pore-water and has an effect on the mechanical behavior of the soil – a change in salt content results in changes in the soil's overall volume and shear strength. Most engineering problems involving unsaturated soils are usually the result of environmental factors (e.g., excessive rainfall), primarily affecting the matric suction component. Changes in the osmotic suction are usually less significant. Additionally, the total suction is more relevant at high suctions (greater than S_r conditions). The residual saturation is defined as the degree of saturation at which an increase in matric suction does not produce a significant change in the degree of saturation, as illustrated in Figure 6.4 (Fredlund, 2000; Fredlund and Rahardjo, 1993).

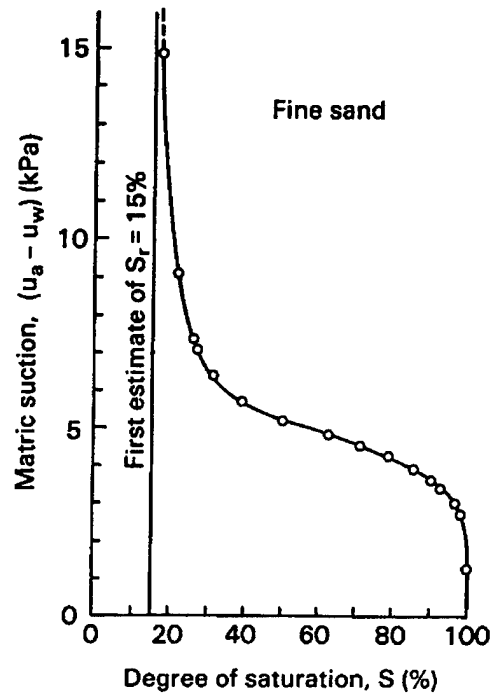


Fig. 6.4 Residual saturation (Fredlund and Rahardjo, 1993)

6.1.3 The Soil-Water Characteristic Curve

The amount of water in the soil is generally quantified in terms of S , the gravimetric water content, w , or the volumetric water content, θ . Whereas the w is the ratio of the mass of water in the soil to the mass of dry soil (M_w/M_s), θ is the ratio of the volume of water to the total volume (V_w/V). The soil-water characteristic curve is a relationship between θ and the soil suction, with θ as the ordinate and matric suction as the abscissa (using matric suction in the lower

suction range – 1500 kPa [218 psi] – and total suction [which includes the osmotic suction, π] in the higher suction range). Typical soil-water curves are shown in Figure 6.5 (Fredlund, 2000).

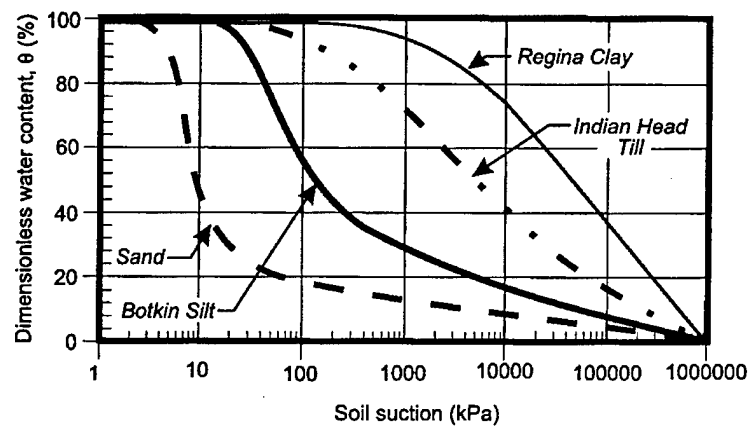


Fig. 6.5 Typical soil-water characteristic curves for four soils from Saskatchewan, Canada (Fredlund, 2000)

6.1.4 The Axis Translation Technique

An acrylic pressure plate device with a 1 bar (100 kPa) high air-entry disk known as a Tempe pressure cell is normally used to determine the water contents corresponding to low suction values. The disassembled components of a Tempe pressure cell, assembled Tempe pressure cell, and cross section of a Tempe cell are shown in Figures 6.6, 6.7, and 6.8, respectively.

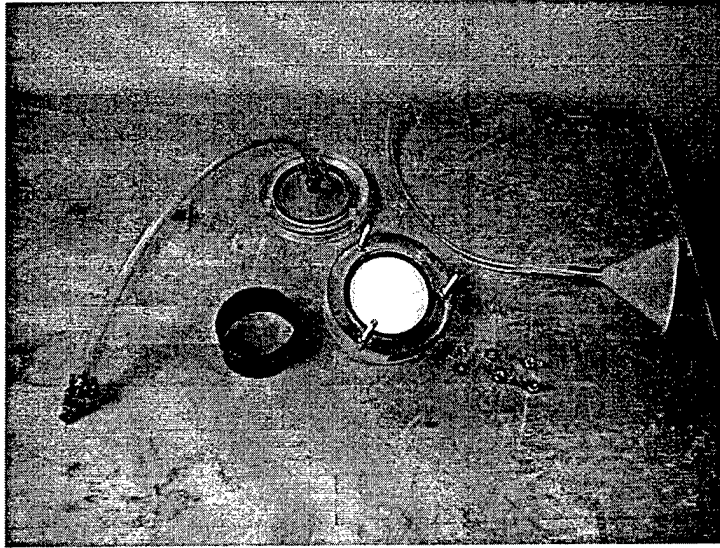


Fig. 6.6 Disassembled Tempe pressure cell

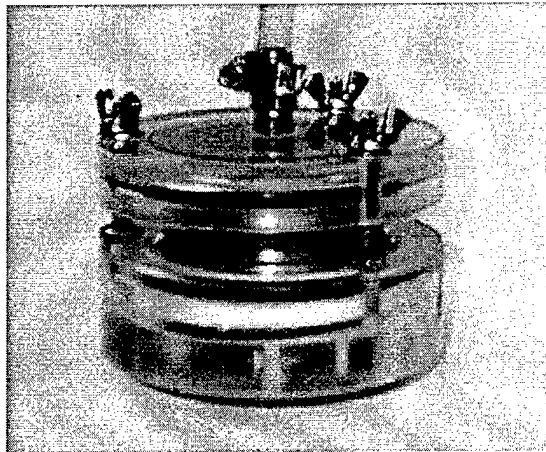


Fig. 6.7 Assembled Tempe pressure cell

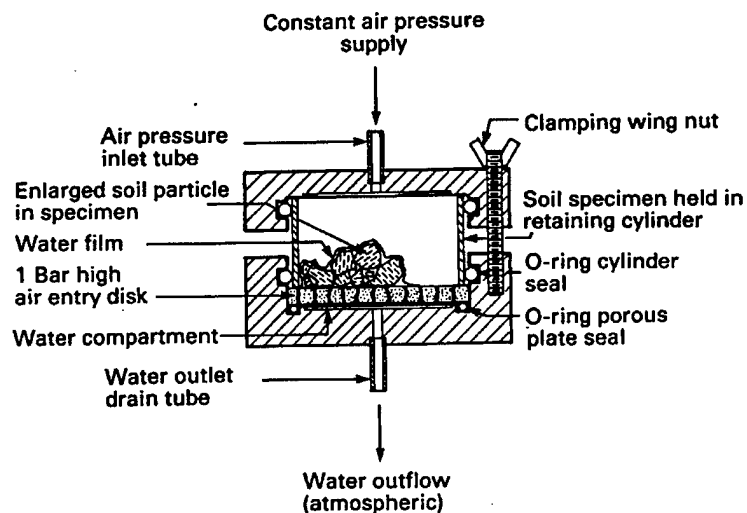


Fig. 6.8 Cross section of a Tempe pressure cell (from Soil-moisture Equipment Corporation, 1985)

Use of the Tempe cell in the development of the soil-water characteristic curve requires using what is known as the axis translation technique. In testing soils with negative pore-water pressures approaching -14.7 psi (~ -100 kPa gauge), water in the measuring system may start to cavitate when the water pressures approach -14.7 psi (~ -100 kPa). As cavitation occurs, the measuring system becomes filled with air, forcing water from the measuring system into the soil. This condition is avoided by translating the reference or pore-air pressure and referencing the pore-water pressure to a positive air pressure (Fredlund and Raharjdo, 1993). When using the Tempe cell, u_a becomes equal to the externally applied air pressure. By connecting the water outflow to a tube filled with water

at the same height as the top of the specimen (as shown in Figure 6.9), u_w is equal to zero. As a result, the matric suction, $(u_a - u_w)$ is equal to the applied air pressure. Water is forced out of the soil, through the high air-entry disk, and into the water reservoir. The soil's volumetric water content at equilibrium (i.e., no more water is being forced out of the soil) is plotted against the matric suction (applied u_a) in order to develop the soil's soil-water characteristic curve.

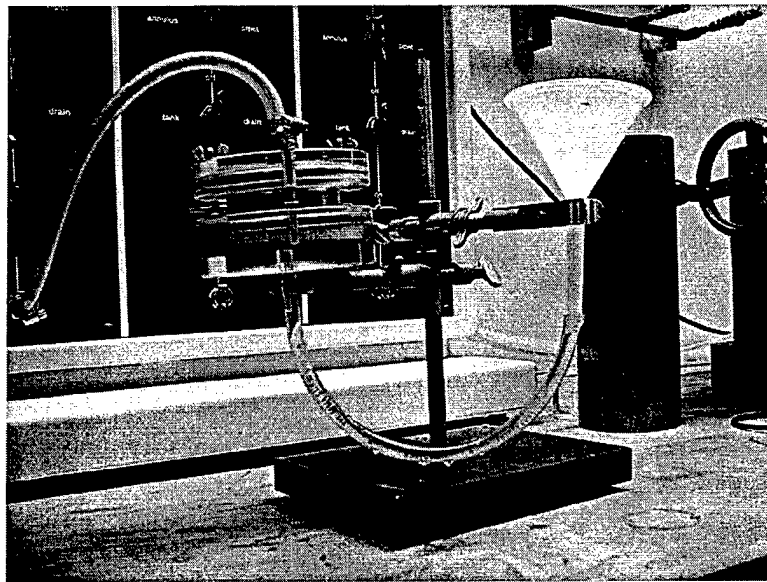


Fig. 6.9 Tempe pressure cell with water outlet connected to water reservoir at same height as top of soil specimen

The aforementioned high air-entry disk is a porous ceramic disk that allows the passage of water, but prevents the flow of free air up to its rated air

entry value (14.7 psi [~ 100 kPa] for the Tempe pressure cell). The ceramic disk permits the control of u_a and u_w (Fredlund, 2000; Fredlund and Rahardjo, 1993).

6.2 Development of the Soil-Water Characteristic Curve

Tempe pressure cell testing was conducted on samples of the GAB used to construct the UAB layer in the quarry haul road in order to develop a soil-water characteristic curve to determine the negative pore-water pressures acting in the UAB layer. For each test, a dry amount of GAB was scalped of aggregate larger than 0.5 in. (1.3 cm) and mixed with 6% by mass of water and compacted into the brass ring of the Tempe pressure cell. Prior to placing the soil in the cell, the porous ceramic disk was placed in a beaker of water and saturated. A compacted specimen is shown in Figure 6.10.

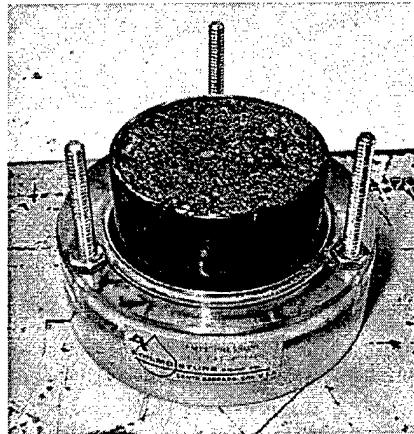


Fig. 6.10 Compacted GAB in a Tempe pressure cell

The samples were compacted using a screwdriver handle and a rectangular metal rod. The unit weights of the sample and applied air pressure for each test are shown in Table 6.1.

Table 6.1 Specimen Unit Weights and Applied Air Pressures

Test #	1	2	3	4	5	6
u_a (psi)	0.5	1	2	5	8	12
unit wt. (pcf)	120.4	126.0	122.7	130.0	121.1	127.1

After the soil is compacted into the brass ring, the bottom of the cell is connected to a water reservoir. The height of water is maintained at the same height as the top of the soil sample until the soil is saturated. Although water began ponding on top of the specimen in a matter of minutes, the soil was kept under these conditions overnight. After the soil was considered saturated, the top of the cell was attached and the air pressure applied (as shown in Figure 6.9). The height of the water in the reservoir was kept even with the top of the soil sample in order to maintain zero pore-water pressure, making the matric suction equal to the applied air pressure.

The cell was given a week to equilibrate, after which the cell was disassembled, the soil carefully transferred to a metal cup, weighed, and placed in an oven for drying. The soil was removed from the oven the next day and weighed in order to determine w . Assuming a unit weight of water of 62.4 pcf

(1 g/cm³), and a constant brass ring volume of 2.405x10⁻³ ft³ (68.1 cm³), θ was calculated. The resulting w 's and θ 's for each test are shown in Table 6.2.

Table 6.2 Volumetric Water Contents and Applied Air Pressures

Test #	1	2	3	4	5	6
u_a (psi)	0.5	1	2	5	8	12
w (%)	10.3	7.3	6.0	4.7	3.3	2.7
θ (%)	18.7	13.9	10.9	9.3	6.0	5.1

The applied u_a 's were plotted with their corresponding θ 's resulting in the soil-water characteristic curve, as shown in Figure 6.11.

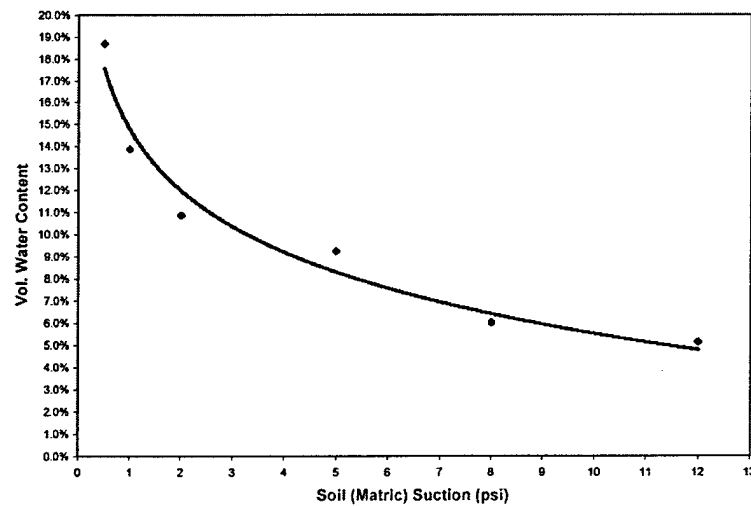


Fig. 6.11 Soil-water characteristic curve for UAB layer

6.3 Negative Pore-Water Pressures in the UAB Layer

Once the soil-water characteristic curve was developed, the gravimetric water contents measured on the day of testing were converted to volumetric water contents (using the NDG average dry unit weights from Table 4.4 for Sites 3 and 5, and 135.3 pcf for Site 2, and assuming a unit weight of water of 62.4 pcf [1 g/cm^3]). The volumetric water contents were used to determine the matric suctions for each test site, as shown in Figure 6.12. The water contents and corresponding matric suctions are listed in Table 6.3.

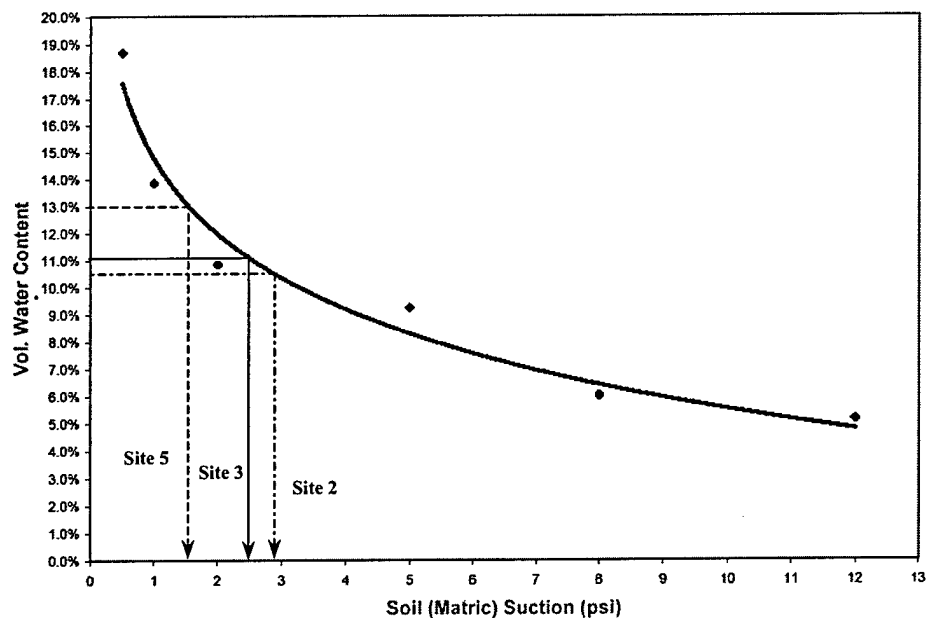


Fig. 6.12 Determining the matric suctions

Table 6.3 Volumetric Water Contents and Corresponding Matric Suctions

Date of Test	Location	w (%)	θ (%)	Matric Suction (psi)
1/24/02	Site 2	4.8	10.5	2.9
1/24/02	Site 3	4.9	11.1	2.5
1/24/02	Site 5	5.7	13.0	1.6

Assuming that u_a is equal to zero in the field, u_w would be equal to the negative value of the matric suction. Additionally, if u_a is assumed to be zero (atmospheric), then it can be inferred that the state of stress would be equal to the effective stress:

$$\sigma' = \sigma - u_w \quad (6.2)$$

This would result in a state of effective stress higher than the total stress, which is especially important during conditions of no external loading as the negative pore-water pressures are greater than the total gravimetric stresses. These negative pore-water pressures also play an important role in calculating the radial effective stress, σ_r' :

$$\sigma_r' = \sigma_v * K - u_w \quad (6.3)$$

where σ_v = vertical total stress and

K = coefficient of lateral earth pressure.

CHAPTER SEVEN

Determination of Vertical and Radial Normal Stresses in the UAB Layer

7.1 Overview of ILLI-PAVE

The ILLI-PAVE computer program was utilized to determine the state of stress in the UAB layer under the various loading conditions. The program considers the pavement as an axisymmetric solid of revolution and divides it into a number of finite elements, each as a section of concentric rings. The stress-dependent resilient modulus and the failure criteria for granular materials and fine-grained soils are incorporated in ILLI-PAVE. In order not to exceed the strength of the materials, as defined by the Mohr-Coulomb failure envelope, the principal stresses in the granular and subgrade layers are modified at the end of each iteration (Raad and Figueroa, 1980).

The finite element model treats the pavement as a series of interconnected elements. Each layer of elements can be assigned a Young's modulus, E , and Poisson's ratio, ν , which permits a representation of the influence of stress variation on the modulus in both the vertical and horizontal directions (Elliot and Lourdesnathan, 1989).

According to the ILLI-PAVE User's Manual (1990), "The pavement is modeled as a three-dimensional pavement section using a two-dimensional half space of a finite solid of revolution. By symmetry, the solution of the three-dimensional solid may be specified in terms of a plane radial section of rectangular configuration. This rectangular half space is then divided into a set of rectangular elements that comprise the finite element mesh." This model is illustrated in Figures 7.1 and 7.2.

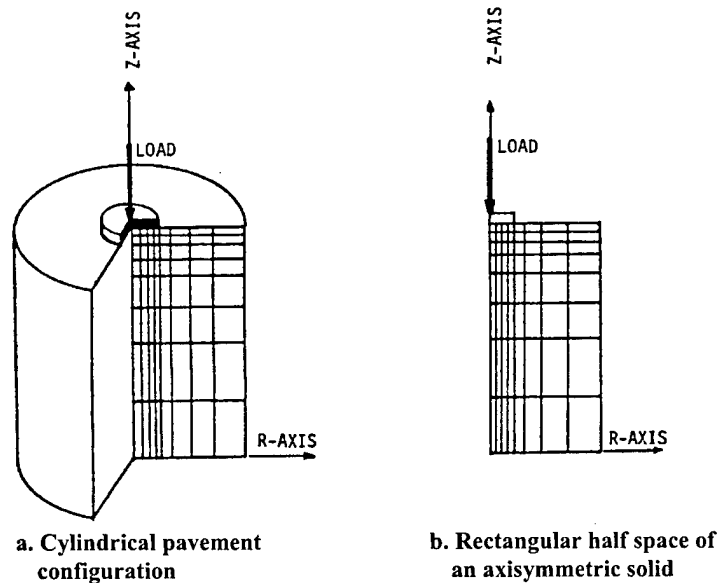


Fig. 7.1 ILLI-PAVE pavement model (ILLI-PAVE User's Manual, 1990)

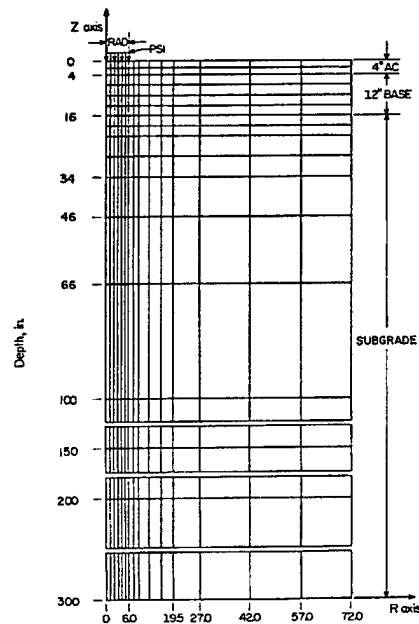


Fig. 7.2 Example system configuration of the finite element mesh (ILLI-PAVE User's Manual, 1990)

The elements and nodes forming the system mesh are sequentially numbered radially outward and top to bottom. Smaller elements are used in the areas of primary concern (directly below the loaded area and in upper primary structural areas) in order to get the most accuracy with limited computing time. The surface contact pressure and the radius of the loaded area are used to specify the loading (ILLI-PAVE User's Manual, 1990).

7.2 Calculating the Vertical and Radial Total Normal Stresses

The layers of the pavements for all three sections were modeled as constant modulus materials. The HMA, subbase, 2 in. (5.1 cm) of GAB, and subgrade were all assigned constant values for E, total unit weight (γ), ν , and coefficient of lateral earth pressure, K, as shown in Table 7.1.

Table 7.1 Input Values for Young's modulus and Poisson's Ratio

	HMA	cemented subbase	surge stone subbase	2 in. of GAB	subgrade
E (psi)	500,000	2,000,000	30,000	30,000	22,000
E (kPa)	3,400,000	13,700,000	200,000	200,000	150,000
Unit wt. (pcf)	145	150	145	145	130
Unit wt. (kg/m ³)	2300	2400	2400	2300	2200
ν	0.4	0.2	0.2	0.2	0.45
K	0.67	0.4	0.4	0.45	0.45

The E for the UAB layer was based on the PH-wave velocity measured under each external loading, assuming a Poisson's ratio of 0.15, and calculated as follows:

$$E_{\max} = \frac{V_{PH} \left(\frac{\gamma}{g} \right) (1 + \nu)(1 - 2\nu)}{(1 - \nu)} \quad (7.1)$$

where V_{PH} is the PH-wave velocity and g is the acceleration of gravity.

The resulting values for E for a typical test site are shown in Table 7.2. The Young's moduli for each of the sites and corresponding loading conditions can be found in Appendix B.

Table 7.2 Calculated values for Young's modulus for the UAB layer at Site 5

External Load (lbs.)	0	1270	5670	8370
E (psi)	26,800	32,200	64,100	71,000
E (kPa)	180,000	220,000	440,000	490,000

The ILLI-PAVE program was run for each of the three external loading conditions. The resulting vertical and radial total normal stresses (σ_v and σ_r , respectively) at the middle of the UAB layer, in the center of the loaded area, for a typical site (including the geostatic normal stresses for zero external load, assuming a K-value of 0.4) are shown in Table 7.3. The loaded area was determined by measuring the footprint of the wheel used to load the test site. The ILLI-PAVE vertical and radial total stresses for each of the sites and corresponding loading conditions can be found in Appendix C.

Table 7.3 Computed Total Normal Stresses in the Middle of the UAB Layer at Site 5

External Loading (lbs)	Loaded Area (in.²)	Vert. Total Normal Stress (psi)	Rad. Total Normal Stress (psi)
0	N/A	0.50	0.20*
1270	68.8	6.14	0.16
5670	111.4	26.1	0.45
8370	129.5	36.3	.78

*note: calculated using a K-value of 0.4

7.3 Calculating the vertical and radial effective normal stresses

Utilizing the vertical total normal stresses computed by ILLI-PAVE and the pore-water pressures determined using the aforementioned soil-water characteristic curve (shown in Figure 6.12), the vertical effective normal stress (σ_v') for each loading condition was calculated using Eq. 6.2. Additionally, the radial effective normal stresses (σ_r') were calculated in the same manner. The resulting vertical and radial effective normal stresses at the middle of the UAB layer for a typical site are presented in Table 7.4.

Table 7.4 Computed Effective Normal Stresses in the Middle of the UAB Layer at Site 5

External Loading (lbs)	Vert. Total Normal Stress (psi)	Rad. Total Normal Stress (psi)	Pore-water Pressure (psi)	Vert. Eff. Normal Stress (psi)	Rad. Eff. Normal Stress (psi)
0	0.50	0.20*	-1.6	2.1	1.80
1270	6.14	0.16	-1.6	7.7	1.76
5670	26.1	0.45	-1.6	27.7	2.05
8370	36.3	.78	-1.6	37.9	2.38

*note: Calculated using a K-value of 0.4

7.4 Total Stress Profiles in the UAB Layer from ILLI-PAVE

An examination of the vertical and radial total normal stresses over the entire profile of the UAB layer was performed on Site 5 in order to study the distribution and evaluate the reasonableness of the vertical and radial total normal stresses computed by ILLI-PAVE. The vertical and radial total stresses at the top and bottom of the UAB layer computed by ILLI-PAVE were plotted along with

the computed vertical and radial total normal stresses at the middle of the layer for each loading condition. The vertical and radial total normal stresses for a 2:1 load distribution and Boussinesq influence factors beneath the center of the loaded area were also plotted with the ILLI-PAVE vertical total normal stresses. The resulting plots are shown in Figures 7.3 through 7.5. The geostatic normal stresses under the case with no external load are shown in the figures.

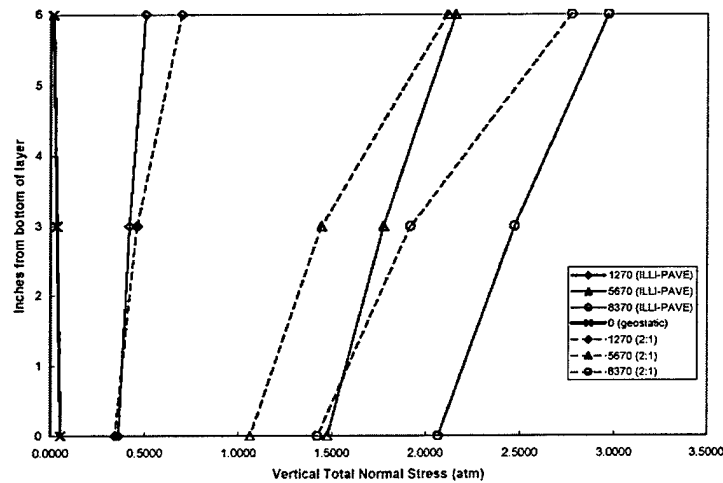


Fig. 7.3 Vertical total normal stresses in the UAB layer at Site 5 based on ILLI-PAVE and 2:1 distributions

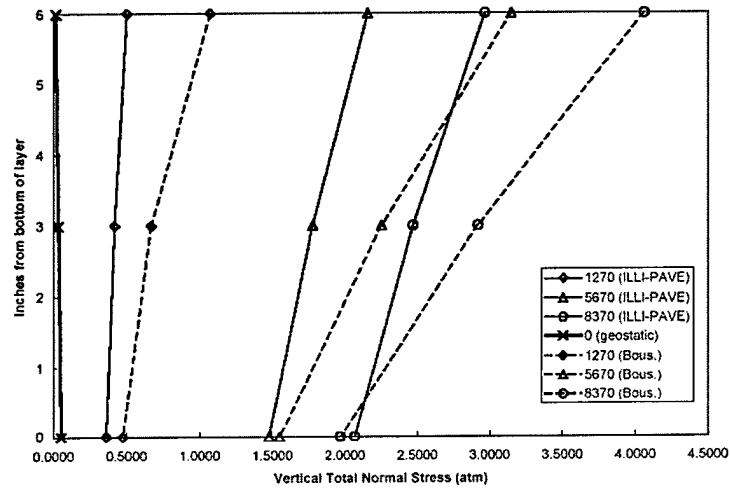


Fig. 7.4 Vertical total normal stresses in the UAB layer at Site 5 based on ILLI-PAVE and Boussinesq distributions

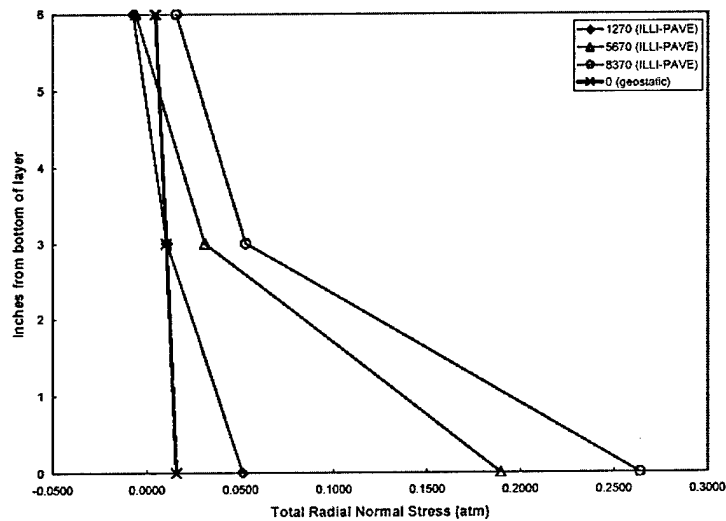


Fig. 7.5 Radial total normal stresses in the UAB layer at Site 5 from ILLI-PAVE

In addition, the vertical and radial effective normal stresses at the top and bottom of the UAB layer were also calculated using the vertical and radial total normal stresses above and the pore-water pressure calculated for Site 5. These values were plotted with the vertical and radial effective normal stresses calculated for the middle of the layer, as shown in Figures 7.6 through 7.8.

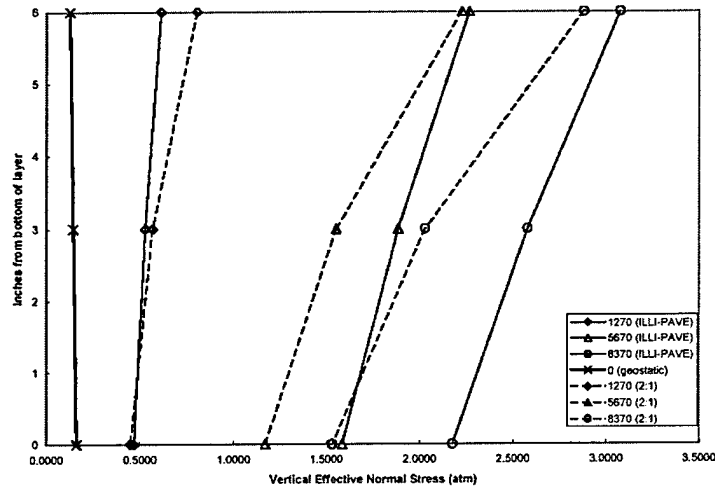


Fig. 7.6 Vertical effective normal stresses in the UAB layer at Site 5 based on ILLI-PAVE and 2:1 distributions

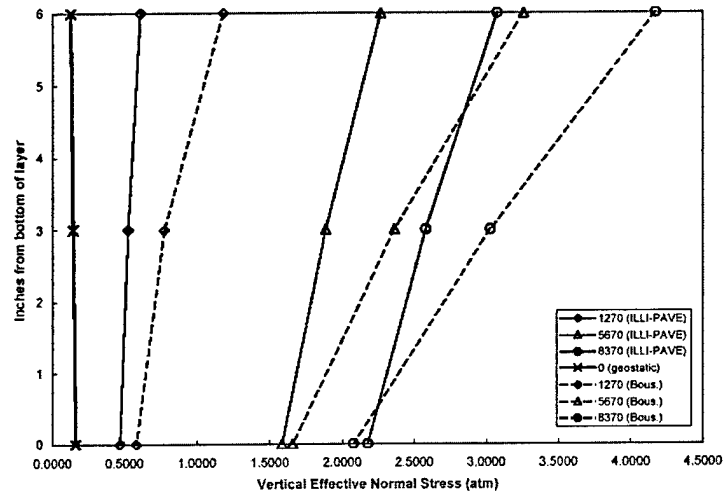


Fig. 7.7 Vertical effective normal stresses in the UAB layer at Site 5 based on ILLI-PAVE and Boussinesq distributions

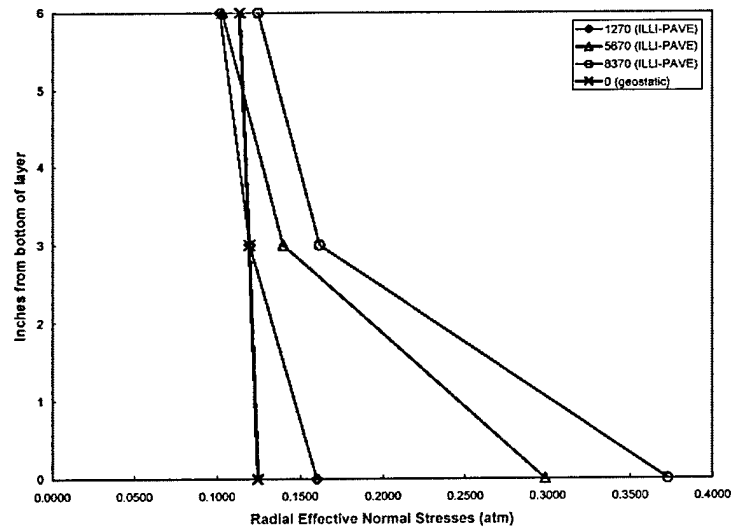


Fig. 7.8 Radial effective normal stresses in the UAB layer at Site 5 from ILLI-PAVE

As can be seen in Figures 7.3, 7.4, 7.6, and 7.7, the vertical total and effective normal stresses decrease with depth (except in the case of zero external load), as would be expected for a small loaded area. However, the ILLI-PAVE radial total and effective stresses increase with depth, as shown in Figures 7.5 and 7.8, which seems opposite to what would be expected as the influence of the loading is expected to decrease with depth. This unexpected result may be explained by the possibility that an isotropic, layered analysis is not appropriate for this situation. ILLI-PAVE is capable of performing a non-linear analysis that may have produced radial total normal stresses more in line with those calculated in the next section.

7.5 Radial Total and Effective Normal Stresses Using a Constant Value of K

New radial total normal stresses were calculated for the Site 5 profile in accordance with the following equation:

$$\sigma_r = \sigma_v * K \quad (7.2)$$

in which a value of 0.3 was used for K.

The radial effective normal stresses were calculated by using the σ_r -value calculated in Eq. 7.2 and then subtracting the pore-water pressure. In this case, the water is assumed to have a K-value of 1.0. The resultant profile plots are shown in Figures 7.9 and 7.10.

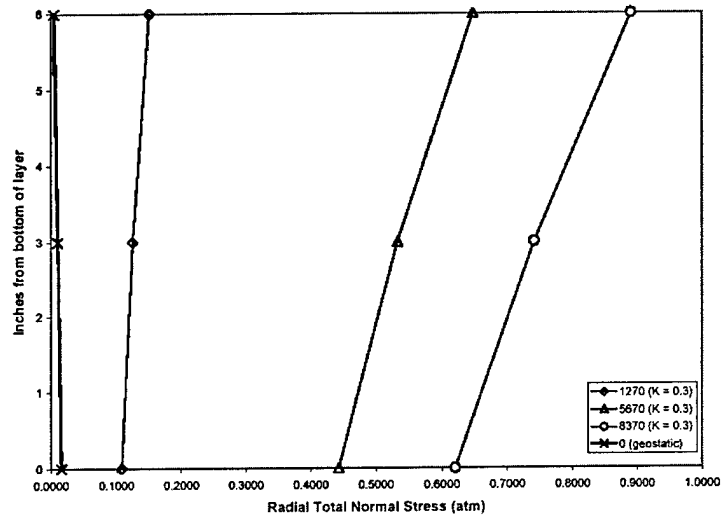


Fig. 7.9 Calculated radial total normal stresses in UAB layer at Site 5

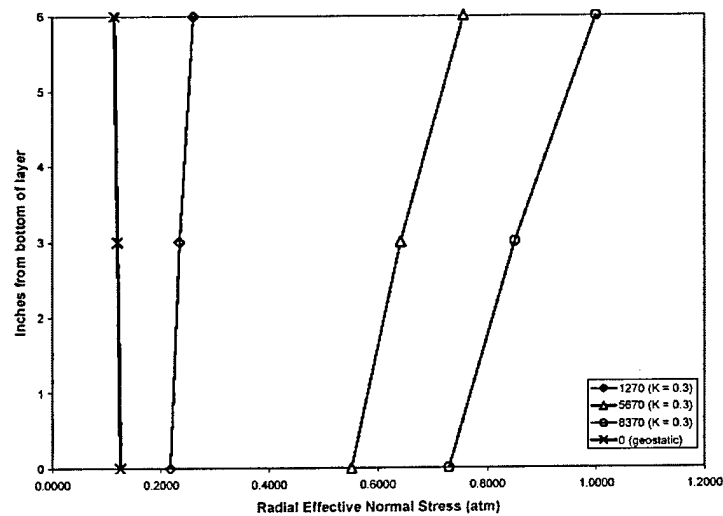


Fig. 7.10 Calculated radial effective stresses in UAB layer at Site 5

As can be seen in Figures 7.9 and 7.10, the radial total and effective stresses are decreasing with depth, as would be expected. As a result, these results are used in the analysis presented in Chapter 8. This approach is supported in Chapter 8 where the radial effective stresses are plotted versus the PH- and SHH-wave velocities. The vertical and radial total and effective stresses for each of the sites and associated loading conditions are presented in Chapter 9.

CHAPTER EIGHT

Stiffnesses Measured by Seismic Crosshole Testing

8.1 Introduction

As discussed in Chapter 5, miniaturized versions of crosshole and downhole seismic tests were conducted in the UAB layer. Unfortunately, the only readily identifiable seismic waves were the PH and SHH waves measured in the crosshole test. Therefore, only the results from the PH and SHH testing are presented below.

8.2 Resultant PH- and SHH-Wave Velocities for Each Site

The plots of PH- and SHH-wave velocities versus radial effective normal stresses (calculated in Section 7.5) determined for Sites 2 through 5 are shown in Figures 8.1 through 8.4, respectively. Also shown in each figure are best-fit lines to the data and associated equations. The equations for the best-fit lines are of the form:

$$V = C \left(\frac{\sigma_r'}{1 \text{ atm}} \right)^n \quad (8.1)$$

where V = the stress wave velocity (y in the equation in the figures)
 C = the stress wave velocity at 1 atm,
 σ_r' = the radial effective normal stress in atmospheres, and
 n = the exponent of the power function.

In this case, the values of σ_r' were calculated from σ_v' determined using ILLI-PAVE and a K-value of 0.3 as discussed in Section 7.5.

Values of Poisson's ratio are also shown in each figure. These values were calculated by dividing the coefficient from the PH best-fit line by the coefficient from the SHH best-fit line. In all cases, the "interpreted" relationships were used when they were present. (The interpreted relationships are discussed below).

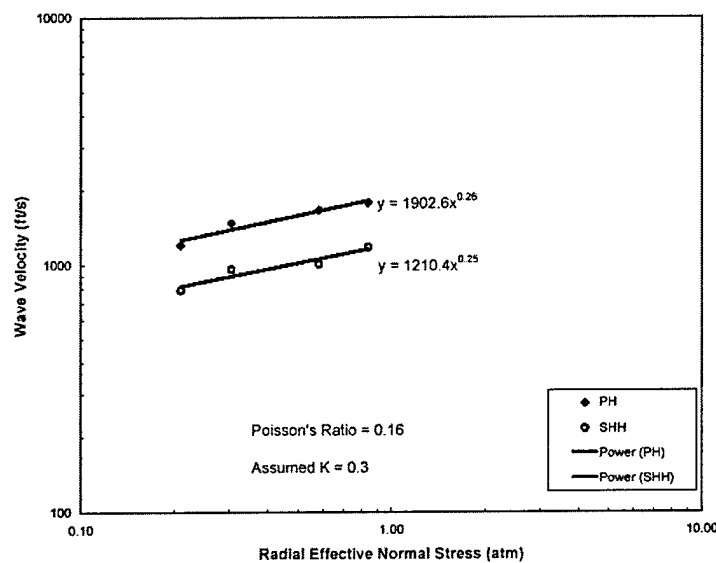


Figure 8.1 Variations of PH- and SHH-wave velocities with stress state for Site 2

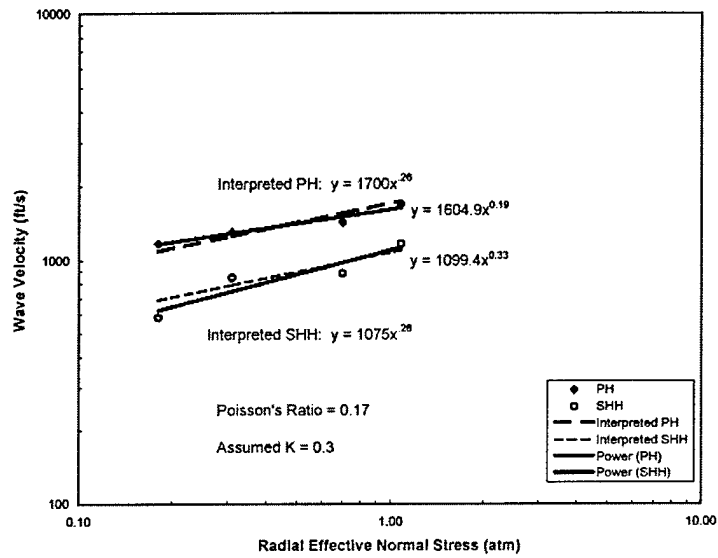


Figure 8.2 Variations of PH- and SHH-wave velocities with stress state for Site 3

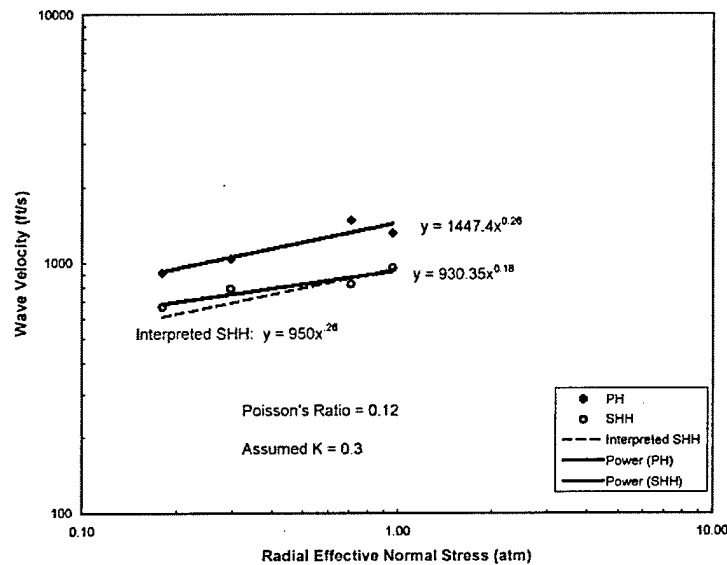


Figure 8.3 Variations of PH- and SHH-wave velocities with stress state for Site 4

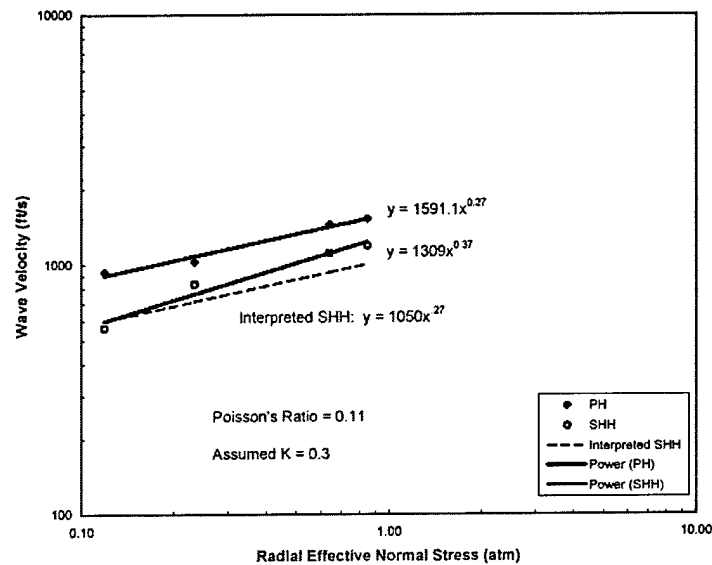


Figure 8.4 Variations of PH- and SHH-wave velocities with stress state for Site 5

As can be seen in Figures 8.1 through 8.4, the slopes of the best-fit lines for the PH-wave velocities fall closely in line with each other, with the exponent varying between 0.26 and 0.27. Also, in only one case (Site 3 in Figure 8.2) was it necessary to “interpret” the PH results by placing by eye a line through the four data points that is slightly different than the best-fit line which fits the data and also agrees well with the slopes of the other PH results. The logic used in this interpretation is that slight unknown variations in the measurements caused the measured data to differ slightly but the general trend was still captured in the measured data.

Upon reviewing Figures 8.1 through 8.4, it is obvious that the SHH-wave velocities exhibit much more scatter than the PH-wave velocities, requiring a bit more "interpretation" to find the appropriate line for the data. This variance in the SHH-wave velocity profiles is due to the significant amount of interpretation that was sometimes required by the individual analyzing the travel time records. This difficulty in interpretation was certainly increased by the short travel times, reflecting and refracting boundary surfaces, and distribution in the states of stress in the vertical direction throughout the UAB layer. The plotted velocities were calculated from a combination of direct and interval travel times, the time chosen being a function of the quality of the record.

Interestingly, all of the Poisson's ratios are near the assumed value of 0.15 used in the ILLI-PAVE analysis. A power regression was used to develop the best-fit line for the measured data, which agreed closely with the results from previous studies of granular soils; that is, the log wave velocity versus log normal stress relationship should be linear. Also, in this analysis, the radial normal effective stress was assumed to have the same value in all horizontal directions.

8.3 Comparison of the PH-Wave Velocity Profiles

A comparison of the PH-wave velocities for each of the four sites is shown in Figure 8.5. The PH waves show that the stiffnesses in the horizontal

direction of all base layers are reasonably close, with the traditional section (Site 2) being the stiffest. The relatively high stiffness of Site 2 is thought to be due to the long period of compaction of the surge stone subbase before construction of the UAB layer (about four months of use of the road), essentially transforming this section into an inverted pavement. The South African and Georgia sections are nearly the same, with the two South African sites (Sites 3 and 4) bracketing the Georgia site (Site 5). This relative comparison is also supported by the SHH waves as shown in the next section.

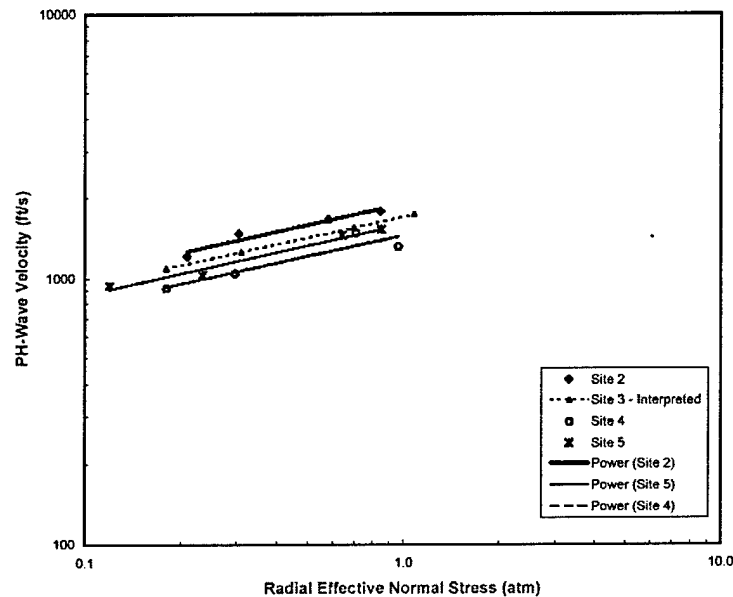


Figure 8.5 Variation of PH-wave velocity with stress state for all four sites

Using Eq. 7.1, the horizontal maximum Young's modulus, $E_{H,max}$ was calculated for each site and loading condition utilizing the Poisson's ratios shown in Figures 8.1 through 8.4. A comparison of $E_{H,max}$ for each of the four sites is presented in Figure 8.6. As with the PH-wave velocities, Site 2 is shown to be stiffer than the other three sites, with the South African sites (Sites 3 and 4) again bracketing the Georgia site (Site 5). It should also be noted that $E_{H,max}$ equals the small-strain value of the resilient modulus, M_r , because there is no permanent deformation in the small-strain range.

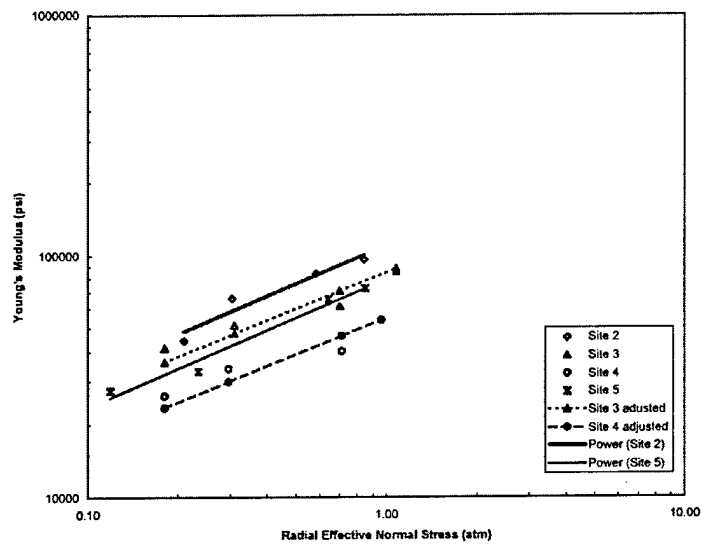


Figure 8.6 Variation of $E_{H,max}$ with stress state for all four sites

The ranges of values for $E_{H,max}$ (highest, lowest, and average) for each loading condition are presented in Table 8.1. All of the calculated values for each site and loading condition are presented in Chapter 9.

Table 8.1 Range in $E_{H,max}$ from All Sites for Each Loading Condition

Loading Condition	1	2	3	4
$E_{H,max}$ – high (psi/kPa)	44,200/ 300,000	66,100/ 460,000	84,100/ 580,000	96,300/ 660,000
$E_{H,max}$ – low (psi/kPa)	26,200/ 180,000	33,900/ 230,000	43,900*/ 280,000	53,900/ 370,000
$E_{H,max}$ – avg. (psi/kPa)	34,800/ 240,000	46,000/ 320,000	62,800/ 430,000	77,200/ 530,000

*note: Actual value was out of range. Reported value is an interpolation.

The importance of pore-water pressure as related to the value of $E_{H,max}$ is illustrated in Figure 8.7, where the plot of $E_{H,max}$ versus radial effective normal stress for Site 5 is shown. The measured data is shown by the open diamonds. The best-fit line to the data is also shown. The values for $E_{H,max}$ for two other conditions are also shown. These conditions are (1) zero pore-water pressure and no external load and (2) $E_{H,max}$ under saturated conditions with a fully-loaded truck inducing a positive pore-water pressure of 10 psi (0.7 atm) in the UAB layer.

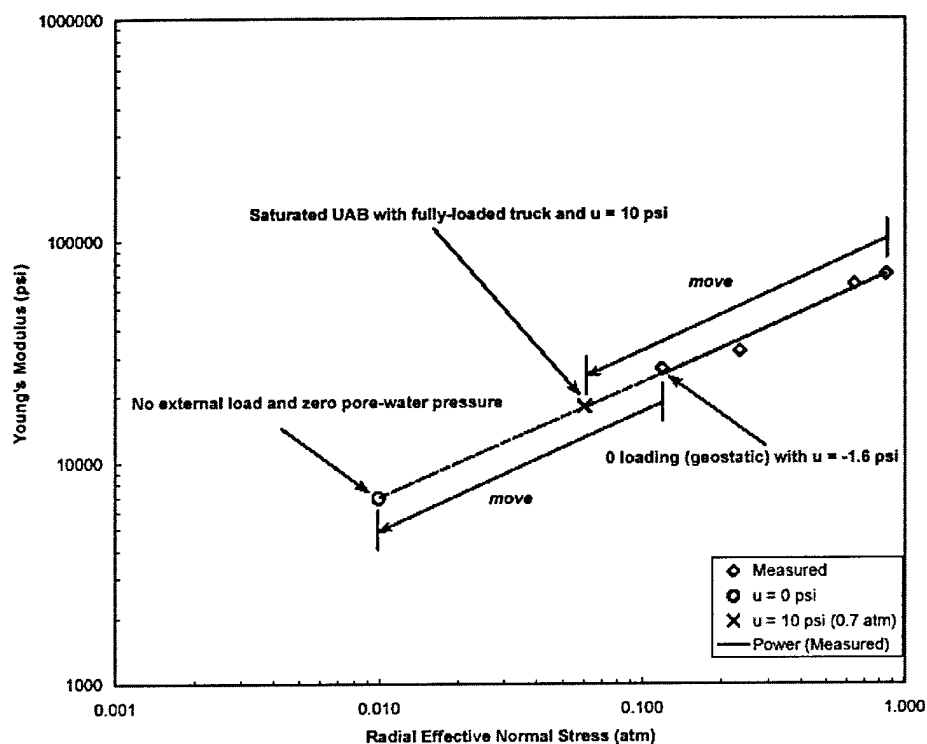


Figure 8.7 Variation of $E_{H,max}$ with stress state for Site 5

As can be seen in Figure 8.7, negative pore-water pressures have a significant impact on the stiffness of the UAB layer, with the value of Young's modulus under zero loading (geostatic) being reduced significantly (by 75%) with the pore-water pressure increasing from a -1.6 psi (-0.1 atm) to zero. Equally disturbing is the loading of the pavement under saturated conditions, where the increase in pore-water pressure from -1.6 to 10 psi under a fully-loaded truck can result in

the stiffness reducing by 75% which could result in pavement failure after repeated loading.

8.4 Comparison of the SHH-Wave Velocity Profiles

A comparison of the SHH-wave velocities for each of the four sites is shown in Figure 8.5. As with the PH-wave measurements, the traditional section (Site 2) is shown to be stiffest, with the South African sites (Sites 3 and 4) bracketing the Georgia site (Site 5).

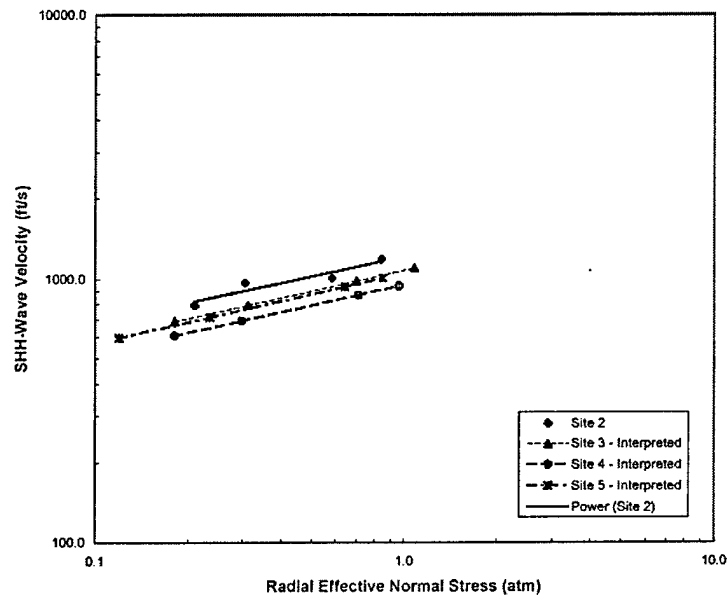


Figure 8.8 Variation of SHH-wave velocity with state of stress for all four sites

8.5 Resonant Column Results

Resonant column testing was also conducted on a sample of GAB at a gravimetric water content of 6% and a total unit weight of 150 pcf (2400 kg/m³) (Menq, 2002). The variation in SHV-wave velocities with effective confining pressures is presented in Figure 8.9. The linear relationship in log-log space based on Eq. 8.1 is shown in Figure 8.9 and shows the same behavior found in previous studies (Menq, 2002).

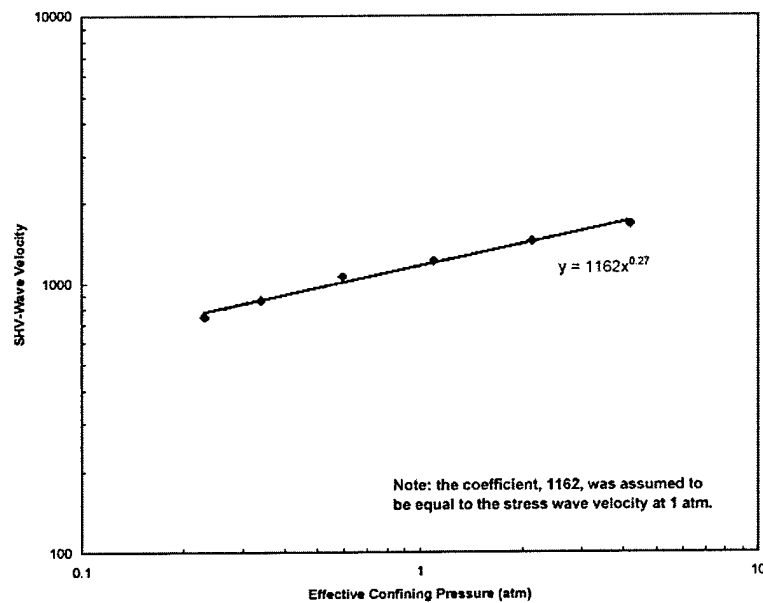


Figure 8.9 Variation of SHV-wave velocity with effective confining pressure of the UAB determined in laboratory by resonant column testing (Menq, 2002)

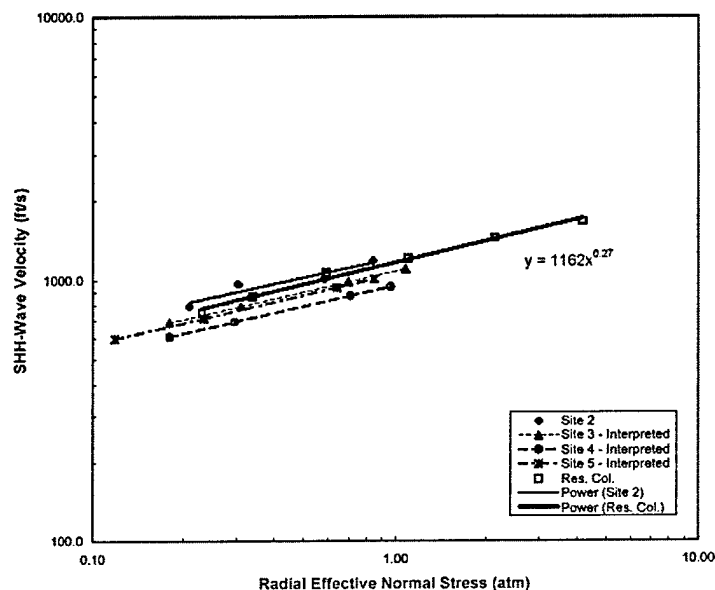


Figure 8.10 Comparison of field SHH-wave velocities measured in the UAB layer with SHV-wave velocities measured in the laboratory by resonant column testing with a reconstituted UAB specimen

The SHH-wave velocities measured in the field are compared with the laboratory results in Figure 8.10. As can be seen from the figure, the SHV-wave velocities measured during resonant column testing compare well with the SHH-wave velocities measured in the field. The fact that the best-fit line to the resonant column data has nearly the same slope ($n = 0.27$) as the slope of the fitted lines associated with the field measurements ($n = 0.26$ to 0.27) indicates that the radial effective stresses for the field measurements are most likely well predicted under the field loading conditions.

8.6 Variation in PH- and SHH-Wave Velocities Versus ILLIPAVE Radial Effective Stresses

As discussed in Chapter 7, the accuracy of the radial total stresses computed by ILLI-PAVE was questioned. The reason for questioning these stresses is understood by viewing the results presented in Figures 8.11 and 8.12, where the PH- and SHH-wave velocities are plotted against the ILLIPAVE radial effective stresses. Power best-fit lines of the data are also presented in the figures.

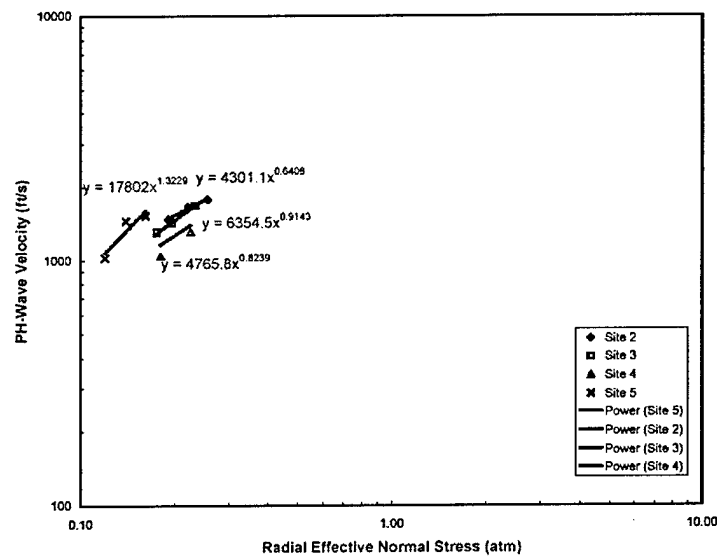


Fig. 8.11 PH-wave velocity vs. ILLI-PAVE radial effective normal stress for all four sites

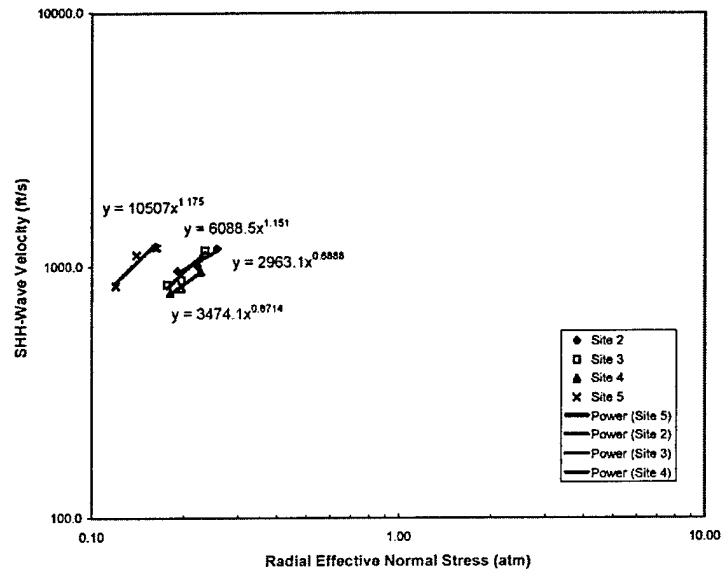


Figure 8.12 SHH-wave velocity vs. ILLI-PAVE radial effective normal stress for all four sites

As can be seen from Figures 8.11 and 8.12, the slopes of the best-fit lines are significantly greater than the slope of the resonant column line. This indicates that the stresses are greatly underestimated under the larger field loading conditions. Accordingly, the radial effective stresses calculated with Eq. 6.2 (using the vertical total stresses computed by ILLI-PAVE and a K-value of 0.3) are a better approximation.

8.7 Estimation of the Anisotropic State of the UAB Layer in Terms of E_{\max}

An estimation of the vertical maximum Young's modulus, $E_{V,\max}$, from these measurements can be done by using the following: (1) the vertical effective

normal stresses, (2) an assumption of structural anisotropy, and (3) the same value of n (exponent of the power best-fit line) as found for $E_{H,max}$ versus the radial effective normal stresses. The resulting equation can be expressed as:

$$E_{V,max} = 0.95C(\sigma_v')^n \quad (8.2)$$

where $0.95C$ = the estimation of structural anisotropy (C is the coefficient of the best fit line from the plot of $E_{H,max}$ versus σ_r') (Belloti, et al, 1996) and n = the exponent of the power best-fit line for $E_{H,max}$ versus the σ_r' .

The plot of the values for $E_{V,max}$ and $E_{H,max}$ versus the effective normal stresses in direction of loading for a typical site (Site 5 in this example) is shown in Figure 8.13.

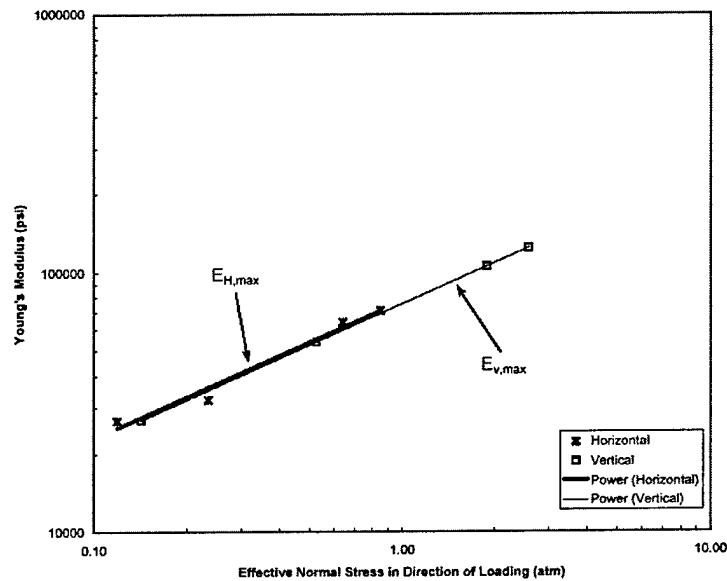


Figure 8.13 $E_{V,max}$ and $E_{H,max}$ vs. the effective normal stresses in direction of loading for Site 5

The plot of the values for $E_{V,max}$ and $E_{H,max}$ versus the loading condition is shown in Figure 8.14.

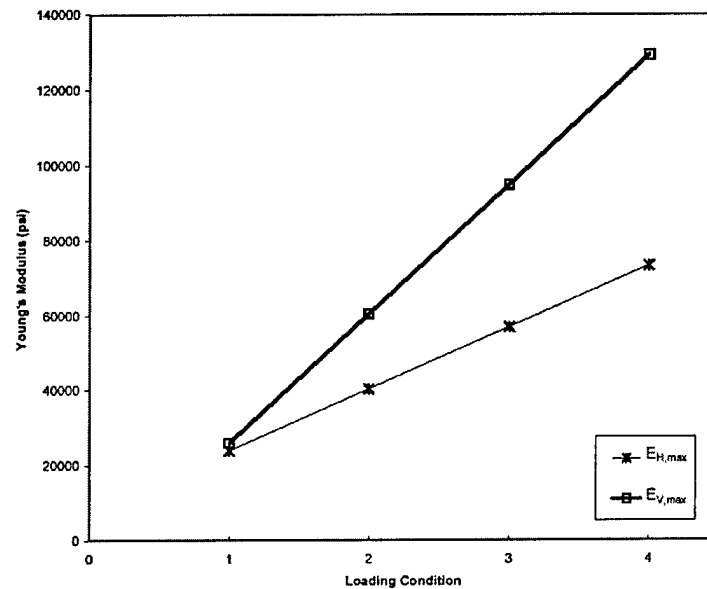


Figure 8.14 $E_{V,max}$ and $E_{H,max}$ vs. the loading condition for Site 5

As can be seen in Figures 8.13 and 8.14, there is an increase in $E_{V,max}$ over $E_{H,max}$ with loading, which is due to σ_v' being greater than σ_r' with increased loading. At the condition with no external load, the values of E are essentially the same because the state of stress is dominated by the value of negative pore-water pressure that has the same value in all directions ($K = 1.0$ for u).

CHAPTER NINE

Summary, Conclusions, and Recommendations

9.1 Summary

Unbound aggregate base (UAB) layers in a quarry haul road in Georgia were characterized with in-situ seismic testing. Two pavement sections were constructed as inverted pavements, one using the South African Roads Board (SARB) method and the other using the Georgia Department of Transportation (GDOT) conventional method. A third control section in the haul road was constructed in the traditional method so that it could be compared with the other two sections. The only difference between the South African section and the Georgia section is that a process known as slushing was used as part of the SARB compaction process. The UAB layer was approximately 6 in. (15.2 cm) thick, had a dry unit weight around 140 pcf, and a water content of about 6% (which was near optimum).

In-situ seismic testing was performed using embedded sensors in the UAB layer in each section. The embedded sensors were installed prior to the placement of the HMA course. Also installed at each test site was a vertical section of PVC pipe that served as a source casing for the crosshole testing. Miniaturized versions of traditional crosshole and downhole tests were conducted in an attempt

to determine the directional stiffnesses at each of the five sites and how these stiffnesses changed under different external loads. The external loads were the single wheel loads of a mini-van, an empty dump truck, and a fully-loaded dump truck.

9.2 Conclusions and Recommendations

9.2.1 Wave Velocity Measurement

Measurements of stiffness of the UAB layer in compression (P) and shear (S) were successfully conducted. These measurements involved horizontally propagating P and S waves. It was found that the Georgia section was as good as the South African section, but that the traditional section was the stiffest. The high stiffness of the traditional section was thought to result from the subbase being subjected to a prolonged period of compaction before construction of the UAB layer, in essence transforming the traditional section into an inverted pavement.

It was found that negative pore-water pressures in the partially saturated granular base had a significant impact on the stiffness of the UAB layer in the unloaded and van-load conditions. It was important to take the pore-water pressure (u) into account if the stiffness was to be correctly predicted.

An increase in stiffness with an increase in load was measured. Using the vertical total normal stresses computed from ILLI-PAVE, a value of 0.3 for K was found to be reasonable for this material in determining the associated radial total normal stress, σ_r . The radial effective normal stress, σ_r' was calculated from σ_r and u .

The value of horizontal Young's modulus at small strains, maximum horizontal Young's modulus ($E_{H,max}$), was determined to range from a low of 26,200 psi (180,000 kPa) for the UAB layer in the unloaded condition to a high of 96,300 psi (660,000 kPa) for the fully loaded condition. A summary of the results in terms of E are given in Table 9.1.

Table 9.1 Summary of Results in Terms of E

Site 2				
External Load (lbs)	σ_v' (atm)	σ_r' (atm)	$E_{H,max}$ (psi)	$E_{H,max}$ (kPa)
0	0.24	0.21	44,200	300,000
1,270	0.55	0.30	66,100	460,000
5,670	1.48	0.58	84,100	580,000
10,280	2.35	0.84	96,300	660,000

Site 3				
External Load (lbs)	σ_v' (atm)	σ_r' (atm)	$E_{H,max}$ (psi)	$E_{H,max}$ (kPa)
0	0.20	0.18	41,100	280,000
1,270	0.64	0.31	51,000	350,000
5,670	1.93	0.70	61,200	420,000
10,010	3.19	1.08	85,500	590,000

Site 4				
External Load (lbs)	σ_v' (atm)	σ_r' (atm)	$E_{H,max}$ (psi)	$E_{H,max}$ (kPa)
0	0.20	0.18	26,200	180,000
1,270	0.59	0.30	33,900	230,000
5,670	1.97	0.71	43,900*	300,000
8,880	2.80	0.96	53,900	370,000

Site 5				
External Load (lbs)	σ_v' (atm)	σ_r' (atm)	$E_{H,max}$ (psi)	$E_{H,max}$ (kPa)
0	0.14	0.12	27,600	190,000
1,270	0.53	0.23	33,100	230,000
5,670	1.88	0.64	65,900	450,000
8,370	2.58	0.85	73,000	500,000

*note: Actual value was out of range. Reported number is an interpolation.

The range in values of $E_{H,max}$ at each loading condition are shown in Figure 9.1. In general, the range in values is within about $\pm 30\%$ of the average at each loading condition.

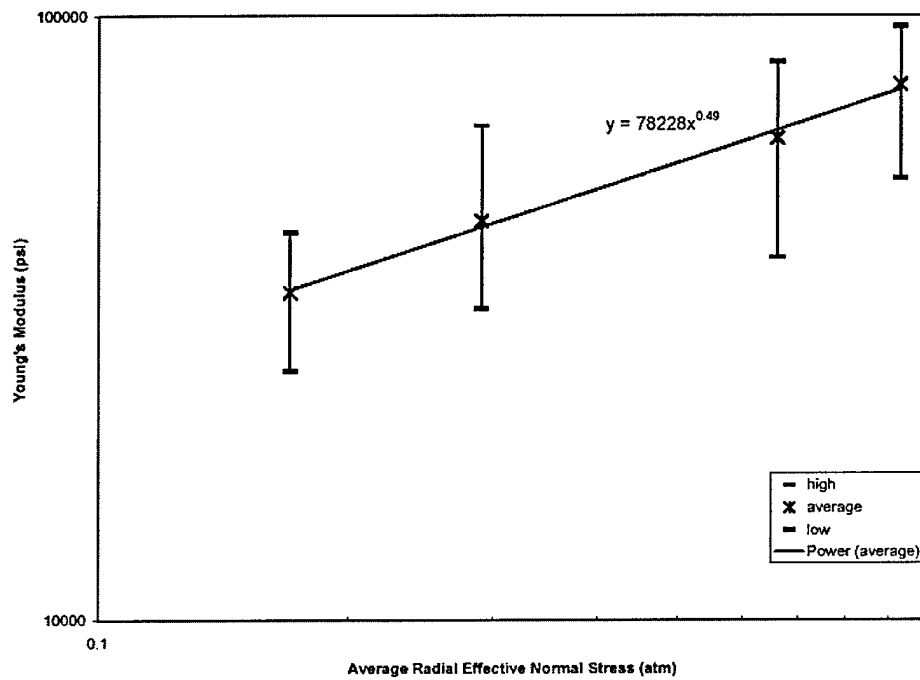


Figure 9.1 $E_{H,max}$ vs. average radial effective normal stress

The Poisson's ratios ranged from a low of 0.11 (Site 5) to a high of 0.17 (Site 3), with an average for all four sites of 0.14.

9.2.2 Field Testing

Overall, the PH- and SHH-wave testing worked reasonably well, giving the best records for measuring the PH- and SHH-wave velocities. The SHV- and

PV-wave testing produced poor quality records. It is felt that this happened due to the large size of the embedded instrumentation relative to the length of the travel paths. Many of the problems would have been minimized had the UAB layer been 12 in. (30 cm) instead of 6 in. (15 cm), providing a longer travel path for the PV-waves and less impact from reflected waves for the SHV waves. It was found that a clear travel path of at least 5 in. (13 cm) was needed for a good travel-time record.

9.2.3 Field Instrumentation

Smaller embedded instruments (approximately half the size of the instruments used) would have worked better given the small thickness of the UAB layer (6 in. thick), especially with respect to the sensors used in the PV wave testing. For this testing, the geophones should have simply been covered with epoxy rather than placed in PVC cases.

The source borehole size worked out well; anything smaller would have been difficult. It is felt that a segmented source casing, permitting the isolation of the impact to the middle of the layer, would have resulted in better SHH-wave records. Additionally, steel bars should have been installed during placement of the HMA and used as sources for PV- and SHV-wave testing in the downhole test.

Appendix A

**Measured PH- and SHH-Wave Velocities and Associated Loading
Conditions**

Site 2				
External Load (lbs)	V _{PH} (ft/s)	V _{PH} (m/s)	V _{SHH} (ft/s)	V _{SHH} (m/s)
0	1,206	368	793	242
1,270	1,475	450	965	294
5,670	1,664	507	1,008	307
10,280	1,780	543	1,181	360

Site 3				
External Load (lbs)	V _{PH} (ft/s)	V _{PH} (m/s)	V _{SHH} (ft/s)	V _{SHH} (m/s)
0	1,168	356	585	178
1,270	1,302	397	851	259
5,670	1,425	434	886	270
10,010	1,686	514	1,167	356

Site 4				
External Load (lbs)	V _{PH} (ft/s)	V _{PH} (m/s)	V _{SHH} (ft/s)	V _{SHH} (m/s)
0	915	279	667	203
1,270	1,041	317	790	241
5,670	1,479	451	823	251
8,880	1,312	400	956	291

Site 5				
External Load (lbs)	V _{PH} (ft/s)	V _{PH} (m/s)	V _{SHH} (ft/s)	V _{SHH} (m/s)
0	936	285	562	171
1,270	1,026	313	839	256
5,670	1,447	441	1,113	339
8,370	1,523	464	1,193	364

Appendix B

**Input Values for Young's Modulus and Associated Loading
Conditions for ILLI-PAVE**

Site 2		
External Load (lbs)	$E_{H,max}$ (psi)	$E_{H,max}$ (kPa)
0	44,600	310,000
1,270	66,600	460,000
5,670	84,800	580,000
10,280	97,100	670,000

Site 3		
External Load (lbs)	$E_{H,max}$ (psi)	$E_{H,max}$ (kPa)
0	41,800	290,000
1,270	51,900	360,000
5,670	62,300	430,000
10,010	87,100	600,000

Site 4		
External Load (lbs)	$E_{H,max}$ (psi)	$E_{H,max}$ (kPa)
0	25,600	180,000
1,270	33,200	230,000
5,670	67,000	460,000
8,880	52,700	360,000

Site 5		
External Load (lbs)	$E_{H,max}$ (psi)	$E_{H,max}$ (kPa)
0	26,800	180,000
1,270	32,200	220,000
5,670	64,100	440,000
8,370	71,000	490,000

Appendix C
ILLI-PAVE Stresses and Loading Conditions

Site 2		
External Load (lbs)	Vert. Total Normal Stress (atm)	Rad. Total Normal Stress (atm)
0	0.04	0.02
1,270	0.36	-0.05
5,670	1.29	-0.27
10,280	2.15	-0.50

Site 3		
External Load (lbs)	Vert. Total Normal Stress (atm)	Rad. Total Normal Stress (atm)
0	0.03	0.014
1,270	0.47	0.006
5,670	1.76	0.026
10,010	3.02	0.063

Site 4		
External Load (lbs)	Vert. Total Normal Stress (atm)	Rad. Total Normal Stress (atm)
0	0.03	0.014
1,270	0.42	0.010
5,670	1.80	0.026
8,880	2.63	0.056

Site 5		
External Load (lbs)	Vert. Total Normal Stress (atm)	Rad. Total Normal Stress (atm)
0	0.03	0.013
1,270	0.42	0.011
5,670	1.78	0.031
8,370	2.47	0.053

References

- Arthur, J.R.F. and Menzies, B.K. (1972), "Inherent Anisotropy in a Sand," Geotechnique, Vol 22, No. 1, pp. 115-128.
- Belloti, R., Jamiolkowski, M., Lo Presti, D.C.F., and O'Neill, D.A. (1996), "Anisotropy of Small Strain Stiffness of Ticino Sand," Geotechnique, Vol. 46, No. 1, pp. 115-131.
- Bolt, B.A. (1976), Nuclear Explosions and Earthquakes, W.H. Freeman and Company.
- Brown, S.F. (1996), "Soil Mechanics in Pavement Engineering," Geotechnique, Vol. 46, No. 3, pp. 383-426.
- Cho, G.C., and Santamarina, J.C. (2001), "Partially Saturated Particulated Materials – Particle Level Studies," Journal of Geotechnical and Geoenvironmental Engineering, Vol. 127, No.1, pp. 84-96.
- Cook, C. (2002), Lafarge North America.
- Department of Transportation, State of Georgia, "Standard Specifications Construction of Roads and Bridges," 1993.
- Elliot, R.P. and Lourdesnathan D. (1989), "Improved Characterization Model for Granular Bases," Transportation Research Record, No. 1227, pp. 128-133.
- Fredlund, D.G. (2000), "The 1999 R.M. Hardy Lecture: The Implementation of Unsaturated Soil Mechanics into Geotechnical Engineering," Canadian Geotechnical Journal, Vol. 37, No. 5, pp. 963-986.
- Fredlund, D. G., Rahardjo, H. (1993), Soil Mechanics for Unsaturated Soils, John Wiley & Sons, Inc.
- Fuhrman, M.D. (1993), "Crosshole Seismic Test at Two Northern California Sites Affected by the 1989 Loma Prieta Earthquake," M.S. Thesis, University of Texas at Austin, May.
- ILLI-PAVE PC Version User's Manual, April 1990, Transportation Facilities Group, Department of Civil Engineering, University of Illinois at Urbana-Champaign.

- Lee, S.H.H., and Stokoe, K.H., II (1986), "Investigation of Low-Amplitude Shear Wave Velocity in Anisotropic Material," Report GR86-6, University of Texas at Austin, 34 pp.
- Lewis, D. (2002), Georgia Department of Transportation.
- Menq, F. Y. (2002), "Dynamic Properties of Gravelly and Sandy Materials," Ph.D. dissertation, University of Texas at Austin.
- Oda, M. (1972), "Initial Fabrics and Their Relations to Mechanical Properties of Granular Material," Soils and Foundations, 12(2), pp. 1-28.
- Raad, L. and Figueroa, J.L. (1980), "Load Response of Transportation Support Systems," Transportation Engineering Journal, ASCE, Vol. 106, No. TE1, pp. 111-128.
- Richart, F.E., Jr., Hall, J.R., Jr., and Woods, R.D. (1970), Vibrations of Soils and Foundations, Prentice-Hall, Inc.
- Roblee, C.J., Stokoe, K.H., II, Fuhrman, M.D., and Nelson, P.P. (1994), "Crosshole SH-wave Measurements in Rock and Soil," Dynamic Geotechnical Testing II, ASTM STP 1213, pp. 58-72.
- Smith, C. (2002), Georgia Department of Transportation.
- South African National Roads Agency (1998), "High Performance Crushed Stone Bases (G1) Used On South African Highways – A General Overview."
- Stokoe, K.H., II, Hwang, S.K., Lee, J.N.K., and Andrus, R.D. (1994), "Effects of Various Parameters on the Stiffness and Damping of Soils at Small to Medium Strains," International Symposium on Prefailure Deformation Characteristics of Geomaterials, Sapporo, Japan, September 12 – 14.
- Stokoe, K.H., II, Lee, J.N.K., and Lee, S.H.H. (1991), "Characterization of Soil In Calibration Chambers with Seismic Waves," First International Symposium on Calibration Chamber Testing, Potsdam, New York, June.
- Stokoe, K.H., II and Santamarina, J.C. (2000), "Seismic-Wave-Based Testing in Geotechnical Engineering," International Conference on Geotechnical and Geological Engineering, GeoEng 2000, Melbourne, Australia, Nov. 19-24.
- Tutumluer, E. (1998), "Anisotropic Behavior of Unbound Aggregate Bases – State of the Art Summary," Invited Paper, In proceedings of the 6th Annual Symposium of the International Center for Aggregate Research (ICAR), St. Louis, Missouri, April 19-21, pp. 11-33.

www.gamedev.net/reference/programming/features/deformsolid2, 2002

www.ph.dhr.state.ga.us/regional/morgan/index.shtml, 2002

www.mcvicker.com/vwall/Hand03b.GIF, 2002

Vita

Ronald Granville Terrell was born in Cincinnati, Ohio on October 27, 1971. He is the son of Rondal Ewell Terrell and Linda Peavyhouse Terrell. He graduated from Milford High School and entered Purdue University in West Lafayette, Indiana in 1990. He graduated from Purdue University with a Bachelor of Science Degree in Civil Engineering and was commissioned an Ensign in the United States Navy's Civil Engineer Corps in May 1994. He was assigned to Naval Mobile Construction Battalion SEVEN in October 1994 where he served as a company officer in Okinawa, Japan and Puerto Rico, and as the Officer in Charge, Deployment for Training, St. Vincent. He was then assigned as the Officer in Charge, Construction Battalion Unit FOUR ZERO SIX in October 1996. His next assignment was with Public Works Center Guam in October 1999, where he served as comptroller and an assistant production officer. While in Guam, he obtained his Professional Engineer (PE) license. He entered the Graduate School at the University of Texas in August 2001.

Permanent Address: 6219 Oak Hill Rd.

Byrdstown, TN 38549

This report was typed by the author.